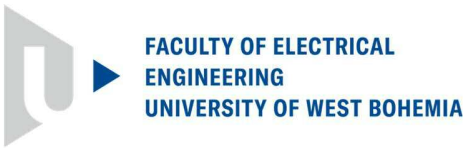

Silesian University of Technology

Faculty of Materials Engineering

Doctoral Thesis

Analysis of Thermal Stresses in Steel Workpiece Heated by Induction

Author: Debela Geneti Desisa

Promoters: Assoc. Prof. Albert Smalcerz, Ph.D., DSc.
Department of Industrial Informatics, Silesian University of Technology, Poland
Assoc. Prof. Václav Kotlan, Ph.D.
Department of Electrical and Computer Engineering, University of West Bohemia, Czech Republic

A Thesis submitted in fulfilment of the requirements for the degree of Doctor of Philosophy (Joint PhD) in the Faculty of Materials Engineering, Department of Industrial Informatics, and the Faculty of Electrical Engineering, Department of Electrical and Computer Engineering.

Academic Year: 2023 – 2024

Acknowledgement

I am so thankful to God for going through the challenges and making me the person I am today. It is God who has been my strength in all difficult times, fears, anxieties, despair, joys, and sorrows. Without the help of God, it would have been difficult to get here and finish my research paper in its current form. My vision was great, my goal far away, and the path was complicated. Glory be to God for all the achievements He has made in my life and through my PhD journey.

Waan hundumaa dabarsee isa nama har'aa nagodhe waaqayyoon guddiseen galateeffadha. Bu'aa ba'ii jireenya hedduu, yeroo ulfaatoo, sodaa, yaaddoo, abdii kutannaa, gammachuu, fi gadda hunda keessatti kan jabina naaf ta'e waaqayyo dha. Mul'atni koo gudda, galmi koo fagoo, daandiin isaa walxaxaa turee. Gargaarsa waaqayyoo malee tasumaa as ga'uunis ta'e waraqaa qoranno koo kana xumuree bifa amma qabu kanaan argachuun hin danda'amu. Fayyaakoo fi amantiikoo osoon hin gatin haala hundaummatti isa nadanda'eef ulfinni hata'u.

This dissertation would not be in its present form without the support of various people from the Silesian University of Technology (SUT) in Poland and the University of West Bohemia (UWB) in the Czech Republic. My heartfelt gratitude goes to my promoters, Prof. A. Smalcerz, for his guidance, encouragement, friendly approach, and willingness to support me in all circumstances during my studies. From him, I learnt kindness, courage, dedication to work, and humility. I am very happy to have pursued my Ph.D. with you and your ambitious team, which I was fortunate to be a part of. My thanks also go to Prof. V. Kotlan for your guidance, supervision, and support in all the necessary facilities during my stay at UWB. I appreciate your friendly approach, courage and advice in modelling and simulation work. Your dedication to swift email responses, as well as your comments, corrections, and improvements to my dissertation, has taught me many valuable lessons for my academic career. I fondly remember the social interactions among the staff in the Department of Electrical and Computer Engineering at UWB, where colleagues would remind each other to go for lunch and enjoy meals together. There was a lot of joy and laughter and I learnt much from them about the importance of fellowship.

My heartfelt acknowledgement goes to Prof. J. Barglik and Prof. I. Dolezel for their unconditional support of my PhD work through your comments and corrections on articles, conference papers, and dissertation documents. I am proud to have had you on this research team. Having you in this team helps me to have confidence in my work and has provided me with many

insights for my future educational endeavours. My appreciation and thanks also go to the unique, happy, and intelligent Dr. A. Smagór for your support in technical aspects. You were always available whenever I faced problems with internet connections, computer system installations, and your welcoming behaviour. Therefore, you deserve special thanks.

My heartfelt acknowledgement goes to all the Industrial Informatics staff members and alumni with whom I worked over the past three and a half years. I also extend my gratitude to the administrative staff of the joint doctoral school, who consistently provided the necessary support and information when I needed their help.

Finally, my special thanks go to my family: my mom, Dame Dhibisa, my wife, Milkaye Mulatu, and my children, Sinan and Miluu, for their unwavering love, courage, and support. My mom always prays to God for me, offering special prayers for my success and expressing her love through phone calls whenever we speak. I wish you a long life with good health. My wife, you deserve special thanks for your support, patience and for taking care of our children. You always use the special word “jabaadhu!” meaning "be strong." Your moral and spiritual support has made a valuable contribution to my PhD work. My son, Sinan, eagerly looks forward to my finished work and always asks when I will come home, motivating me to work hard to complete my PhD on time.

Last but not least, I would like to acknowledge my fellow PhD students from Ethiopia for their support in all situations, difficulties, and anxieties, and for sharing their experiences in academic life. At the beginning of my studies, I shared special memories with Yohannis Jelila and Goftila Sirata.

Debela

July, 20224

Abstract

Thermal stresses arise in a component that undergoes a change in temperature while the material is either externally or internally constrained, preventing it from freely expanding or contracting with the temperature change. The aim of thermal stresses analysis is to ensure the reliability of the design and reduce uncertainty in materials undergoing heat treatment. Thermal stress analysis involves examining the thermomechanical system, which is subjected to heat transfer and heat generation within the material (i.e., induction heating). Therefore, types of multiphysics analysis achieved through numerical methods are the appropriate approach. The study consists of two phases: controlling the heating parameters and subsequent cooling (quenching). Each phase has its own design strategy and controlling mechanism, and failure of one affects the desired mechanical properties.

A precise numerical model that describes the events on the surface of a workpiece during induction heating (IH) as well as the temperature changes within the workpiece is challenging to develop. To address this challenge, the model employs three different algorithms to analyse the temperature distribution from the surface to the core: explicit and implicit event controlling algorithms and a discrete frequency control approach aligned with the coil current. This is achieved through the automation of feedback control mechanisms that adjust the input parameters. Controlling the temperature distribution by adjusting the input parameters is regarded as a means of governing the entire system in induction heating.

The induction hardening model for gear wheels is calibrated to ensure high precision, based on a reliable mathematical model and the correct selection of input parameters. The calibration strategy integrates key parameters to achieve the most effective combination for the specified application, control heat flow, and ensure optimal energy efficiency. However, some of these parameters are often known only with some uncertainty (e.g., physical properties of the material and their temperature dependencies, parameters of cooling of heated teeth, etc.). Therefore, the model must be appropriately calibrated to achieve an acceptable agreement between the calculated results and the experimental data. The detailed calibration strategy is described and illustrated with a typical example.

Thermal residual stress resulting from volume changes due to temperature variations and phase transformations, and its effects on other mechanical properties, has been investigated. A

general model of induction surface hardening was analysed on the basis of coupled electromagnetic, thermal, mechanical, and metallurgical phenomena. The distribution of mechanical strains and stresses is determined in the surface layers of steel materials subjected to induction hardening. This distribution is influenced not only by thermoelastic processes but also by plastic deformations of the exposed layers and the transformation of specific levels of steel. An illustrative example demonstrates the methodology to solve an axisymmetric configuration.

Extracting the transformation-induced plasticity (TRIP) strain from the total strain by experimental analysis of quenching poses significant challenges. However, the Finite Element Method (FEM) is crucial in addressing these challenges and enabling the prediction of multiple co-occurring physical phenomena. The combined effect of thermal and TRIP strains on mechanical properties is demonstrated through an illustrative example using a cylindrical workpiece with a length of 100 mm and a radius of 20 mm. The model also illustrates how phase transformation strains produce stresses and deformations by coupling temperature-dependent phase transformations with an elastoplastic analysis.

The main objective of this work is to minimise uncertainty in model development, optimise processes, and ensure energy efficiency. Uncertainty modelling is helpful in decision-making for new models, especially for processes involving multiphysics (i.e., induction hardening). In this work, a numerical model was developed using COMSOL Multiphysics and data analysis was performed using MATLAB software connected via LiveLink. Temperature control algorithms were developed to explicitly or implicitly define events in the heating process and control them via a feedback loop. Another method used involves defining an objective function subject to constraints and a certain group of parameters. This method is crucial to identify the most influential parameters in the process and to select optimal values.

Elastoplastic models of martensite formation have been presented, providing an overview of different modelling approaches related to martensite formation. In this approach, FEM is implemented to analyse residual thermal stresses, strain formation, and plastic strain evolves when deviatoric stresses and thermal stresses exceed the yield limit.

Streszczenie

Ograniczenia zewnętrzne lub wewnętrzne materiału uniemożliwiają mu swobodne rozszerzanie się lub kurczenie się wraz ze zmianą temperatury stąd, pod wpływem zmian temperatury powstają w tym elemencie naprężenia termiczne. Ich zadaniem jest zapewnienie niezawodności konstrukcji i zmniejszenie niedokładności w materiałach poddawanych obróbce cieplnej. Analiza naprężeń termicznych obejmuje badanie układu termomechanicznego, w którym następuję wytwarzanie i wymiana ciepła (np. przez nagrzewanie indukcyjne). W związku z tym odpowiednim podejściem rozwiązywania tego typu zagadnień jest analiza wielokryterialna z wykorzystaniem metod numerycznych. Analiza składa się z dwóch etapów: kontroli parametrów nagrzewania oraz następującego po nim chłodzenia (hartowania). Każdy etap analizy jest oddzielnym projektem i posiada własne mechanizmy kontrolne, ale każdy z nich wpływa na oczekiwane właściwości mechaniczne materiału.

Opracowanie precyzyjnego modelu numerycznego opisującego zdarzenia zachodzące na powierzchni przedmiotu obrabianego podczas nagrzewania indukcyjnego (IH), a także zmiany temperatury wewnątrz przedmiotu obrabianego, stanowi bardzo trudne wyzwanie. Aby sprostać temu wyzwaniu, w modelu zastosowano trzy różne algorytmy wykorzystywane do analizy rozkładu temperatury od powierzchni do rdzenia wsadu: jawne i niejawne algorytmy sterowania procesami oraz dyskretne sterowanie częstotliwością prądu cewki wzbudnika. Osiąga się to poprzez automatyczną kontrolę mechanizmów sprzężenia zwrotnego, które dostosowują parametry wejściowe. Kontrolowanie rozkładu temperatury poprzez regulację parametrów wejściowych jest uważane za sposób zarządzania całym systemem nagrzewania indukcyjnego.

Model hartowania indukcyjnego kół zębatych kalibrowany jest w celu zapewnienia wysokiej precyzji, w oparciu o rzetelny model matematyczny i prawidłowy dobór parametrów wejściowych. Celem doboru kluczowych parametrów jest osiągnięcie optymalnego rozwiązania, z punktu widzenia przepływu ciepła i efektywności energetycznej. Jednak niektóre z tych parametrów są często znane tylko z pewną niepewnością (np. właściwości fizyczne materiału i ich zależności temperaturowe, parametry chłodzenia nagrzanych zębów itp.). Dlatego model musi zostać odpowiednio skalibrowany, aby osiągnąć akceptowalną zgodność pomiędzy wynikami obliczonymi, a danymi eksperymentalnymi. Szczegółowa metodologia kalibracji została opisana i zilustrowana typowym przykładem.

Zbadano termiczne naprężenia szczątkowe wynikające ze zmian objętości spowodowanych zmianami temperatury i przemianami fazowymi oraz ich wpływ na inne właściwości mechaniczne. Przeanalizowano ogólny model indukcyjnego hartowania powierzchniowego na podstawie sprzężonych zjawisk elektromagnetycznych, termicznych, mechanicznych i metalurgicznych. Określono rozkład odkształceń i naprężeń mechanicznych w warstwach powierzchniowych materiałów stalowych poddanych hartowaniu indukcyjnemu. Na rozkład ten wpływają nie tylko procesy termosprężyste, ale także odkształcenia plastyczne odsłoniętych warstw i przemiany fizyczne stali. Przedstawiony przykład pokazuje metodologię rozwiązywania układu osiowo-symetrycznego.

Trudnym wyzwaniem jest wyodrębnienie odkształcenia plastycznego wywołanego transformacją (TRIP) z całkowitego odkształcenia za pomocą eksperymentu. Jest to możliwe dzięki zastosowaniu metody elementów skończonych (FEM), umożliwiająca rozwiązywanie układów, w których występują sprzężone ze sobą zjawiska fizyczne. Jako przykład takiego układu został opracowany model cylindrycznego przedmiotu obrabianego o długości 100 mm i promieniu 20 mm. Model ten dobrze ilustruje, w jaki sposób odkształcenia związane z przemianą fazową powodują naprężenia i odkształcenia, czyli łączy przemiany fazowe zależne od temperatury z analizą elastoplastyczną.

Głównym celem tej pracy jest zminimalizowanie niepewności przy opracowywaniu modeli, optymalizacja procesów i zapewnienie efektywności energetycznej. Minimalizacja niepewności jest szczególnie istotne dla nowych modeli, zwłaszcza w przypadku procesów obejmujących wiele zjawisk fizycznych, a takim jest hartowanie indukcyjne. W niniejszej pracy model numeryczny został opracowany przy użyciu oprogramowania COMSOL Multiphysics, a analiza danych została przeprowadzona przy użyciu oprogramowania MATLAB połączonego przez LiveLink. Algorytmy kontroli temperatury zostały opracowane w celu jawnego lub niejawnego definiowania zdarzeń w procesie nagrzewania i kontrolowania ich za pomocą pętli sprzężenia zwrotnego. Do wyznaczenia innych parametrów zastosowano metodę polegająca na zdefiniowaniu funkcji celu. Metoda ta jest kluczowa dla zidentyfikowania parametrów mających największy wpływ na proces i wybrania optymalnych wartości.

Zaprezentowano elastoplastyczne modele powstawania martenzytu. W prezentowanym w pracy podejściu, zaimplantowano MES do analizy: szczątkowych naprężeń termicznych, powstawania odkształceń i odkształceń plastycznych.

English summary

The root cause of thermal stress generation is the variation of temperature within the body. The thermal stress generated during induction heating is assumed to not affect the mechanical properties of the material, but the cooling process does. However, the non-linearities of induction heating present challenges for the cooling process, which in turn affects the desired mechanical properties after hardening. Therefore, the study of thermal stress begins with the analysis of the temperature distribution, control of deformation, strain generation, and metallurgical aspects of the material. Thermal stress analysis lies at the crossroads of thermodynamics (heat transfer), solid mechanics (stress and strain), and metallurgical phenomena (phase transformation). Using induction as a source of heat energy to analyse thermal stress makes it more challenging to control the phenomena and achieve the desired results.

Due to its nature, induction heating makes it challenging to control the temperature distribution from the surface to the required depth, especially in surface hardening. To address this challenge, developing digital control mechanisms with control algorithms aligned with feedback closed loop is important. This involves explicitly or implicitly defining the events within the workpiece, connecting them to the current flow switch, and controlling the input power. These methods have several advantages, including achieving the required temperature within the specified range, preventing surface detonation, and not affecting heat transfer.

In both explicit and implicit event control methods, power is supplied intermittently, turning the switch on or off. In explicit event control, the state of an event is defined over a period. This method is computationally costly, time-consuming, but conditionally stable, and designed for simulating short transient dynamic events. In implicit event control, the event is not directly defined over the period; instead, an indicator is used. When the indicator point is reached, the switch is turned off and then on again. Implicit methods are typically used to simulate static or less transient phenomena. These methods aid in the selection of the optimal power, frequency, and coil length in induction heating.

The asynchronous dual-frequency approach employs two distinct frequencies that alternately become active based on the event condition. Lower frequencies allow significant current penetration and a deeper skin effect, making them more efficient for heating larger parts. At high frequencies, current penetration is limited to the surface. On the contrary, higher

frequencies restrict current penetration and influence the generation of eddy current within the workpiece.

Uniform temperature distribution is important in austenitizing because distortion usually arises from the release of residual stresses accumulated during prior processes, such as forging or machining, as well as from non-uniform heating. The distortion caused by the quenching process is largely a function of the austenitizing temperature, the uniformity of the quenching process, and the choice of the quenching medium. The simulation involves two steps: the first step involves heating to the austenite temperature, where coupled electromagnetic and thermal phenomena occur, and the second step involves cooling to the martensite finish (M_f) temperature.

Predicting residual thermal stress and strain begins by tracing the thermal history of the workpiece during quenching. The temperature distribution within the quenched part is affected by the intensity of the quenching process. Faster cooling rates result in a steeper temperature gradient, leading to increased thermal strain within the object. The formation of thermal stresses at various temperatures depends on the degree of strain and, in case of plastic deformation, on the flow stress at that temperature. For an accurate computation of thermal stress and strain, it is crucial to track in parallel the entire sequence of phase transformations alongside the temperature evolution.

Understanding the distribution of stresses and strains within hardened layers is crucial for assessing the risk of cracks and other damage, particularly in components used in machinery, automotive, and aerospace industries. During quenching, different types of stresses develop in the workpiece, at different stages of quenching.

At the initial quenching stage, austenite cools down without phase transformations due to significant thermal gradients. The surface contracts faster than the core, resulting in tensile stresses on the surface and compressive stresses at the core to maintain a balanced stress state. The second stage begins when the martensitic transformation starts on the surface. Dilatational phase-transformation strains and transformation plasticity lead to rapid unloading and reverse loading on the surface. The untransformed core responds to counterbalance these stresses, resulting in significant compressive stresses on the surface and tensile stresses at the core. The third stage begins when phase transformations start at the core, leading to a complete transformation and cooling of the surface.

The extraction of TRIP strain involves the capture of additional plastic deformation resulting from thermal and mechanical stresses during cooling. This extraction of TRIP from total strain

through experimental analysis of quenching poses significant challenges. Thus, Finite Element Method (FEM) plays a crucial role in addressing the challenges associated with and enabling the prediction of multiple concurrent physical phenomena. These include forecasting the temperature history, phase evolution, and internal stresses during quenching processes. Effective prediction and illustrating the fundamental mechanisms of stress development and the distribution of residual stresses are essential for designing advanced materials with enhanced mechanical properties.

COMSOL Multiphysics is a finite element analysis (FEA), solver, and simulation software package used for various physics and engineering applications, especially for coupled phenomena and multiphysics. It offers conventional physics-based user interfaces and can handle coupled systems of partial differential equations (PDEs) in weak form. An API for Java and MATLAB can be used to control the software externally. Models created in COMSOL Multiphysics can be linked to MATLAB via LiveLink for data analysis, as demonstrated in this work. An algorithm was developed to simulate a model, and the resulting data were imported into MATLAB for graphical analysis. Furthermore, a mathematical model was developed to aid in decision-making and predicting material properties. Additionally, software JMatPro was used in this work to generate a CCT diagram and predict the effect of cooling rate on the mechanical properties of the material.

A promising solution to the complexity of induction heating is to develop multifidelity surrogate models that incorporate both high and lowfidelity data, thus striking a balance between prediction accuracy and computational cost. Achieving this balance involves integrating realistic information into the construction of a surrogate model. Induction heating entails sustainability in terms of energy efficiency, environmental friendliness, precise heating to the target area, and rapid heating methods. However, modern technologies, such as the implementation of machine learning and artificial neural networks (ANN), which have recently emerged in the field, require further development.

Podsumowanie

Podstawową przyczyną powstawania naprężeń termicznych jest zmiana temperatury wewnątrz ciała. Zakłada się, że naprężenia termiczne generowane podczas nagrzewania indukcyjnego nie wpływają na właściwości mechaniczne materiału, ale proces chłodzenia. Jednak nieliniowość nagrzewania indukcyjnego stanowi wyzwanie dla procesu chłodzenia, co z kolei wpływa na pożądane właściwości mechaniczne po zakończeniu całego procesu hartowania. Badanie naprężeń termicznych rozpoczęto od analizy rozkładu temperatury, kontroli deformacji, generowania odkształceń i metalurgicznych właściwości materiału. Analiza naprężeń termicznych obejmuje zagadnienia termodynamiki (wymiana ciepła), mechaniki ciała stałego (naprężenia i odkształcenia) oraz zjawiska metalurgiczne (przemiana fazowa). Wykorzystanie indukcji jako źródła energii cieplnej do analizy naprężeń termicznych sprawia, że trudniej jest kontrolować zjawiska i osiągać pożądane wyniki.

Ze względu na charakter procesu nagrzewania indukcyjnego, trudno jest kontrolować rozkład temperatury od powierzchni wsadu do wymaganej głębokości, szczególnie w przypadku hartowania powierzchniowego. Aby sprostać temu wyzwaniu, ważne jest opracowanie numerycznych modeli sterowania uwzględniającymi pętle sprzężenia zwrotnego. Obejmuje to jawne lub niejawne zdefiniowanie procesów odbywających się we wsadzie oraz połączenie ich ze sterowaniem prądu zasilającego i kontrolowaniem mocy wejściowej. Metody te mają kilka zalet, w tym osiągnięcie wymaganej temperatury, zapobieganie deformacji powierzchni i brak wpływu na wymianę ciepła.

Zarówno w jawnych, jak i niejawnych metodach sterowania procesami, zasilanie jest dostarczane w sposób przerywany, włączając lub wyłączając przełącznik. W jawnym sterowaniu procesami stan zdarzenia jest definiowany w pewnym okresie. Metoda ta jest kosztowna obliczeniowo, czasochłonna, ale warunkowo stabilna i przeznaczona do symulacji krótkich przejściowych zdarzeń dynamicznych. W przypadku niejawnej kontroli procesów zdarzenie nie jest bezpośrednio definiowane w okresie; zamiast tego używany jest wskaźnik. Po osiągnięciu punktu wskaźnika przełącznik jest wyłączany, a następnie ponownie włączany. Metody niejawne są zwykle używane do symulacji zjawisk statycznych. Metody te pomagają w doborze optymalnej mocy, częstotliwości i długości cewki w nagrzewaniu indukcyjnym.

Asynchroniczne podejście dwuczęstotliwościowe wykorzystuje dwie różne częstotliwości, które są aktywowane naprzemiennie w zależności od warunków procesu. Niższe częstotliwości pozwalają na większą penetrację prądu i głębszy efekt naskórkowości, dzięki czemu są bardziej wydajne w przypadku nagrzewania większych elementów. Przy wysokich częstotliwościach penetracja prądu jest ograniczona jedynie do powierzchni wsadu.

Równomierny rozkład temperatury jest ważny w procesie austenityzacji, ponieważ odkształcenia zwykle powstają w wyniku uwolnienia naprężeń szczątkowych nagromadzonych podczas wcześniejszych procesów, takich jak kucie lub obróbka skrawaniem, czy też w wyniku nierównomiernego nagrzewania. Odkształcenie spowodowane procesem hartowania jest w dużej mierze funkcją temperatury austenityzacji, jednorodności procesu hartowania i wyboru medium hartowniczego. Symulacje numeryczne obejmują dwa etapy: pierwszy obejmuje nagrzewanie do temperatury austenityzacji, gdzie występują sprzężone zjawiska elektromagnetyczne i termiczne, a drugi etap obejmuje chłodzenie do temperatury zakończenia przemiany martenzytycznej (M_f).

Przewidywanie szczątkowego naprężenia termicznego i odkształcenia rozpoczyna się od prześledzenia historii termicznej wsadu podczas hartowania. Na rozkład temperatury w hartowanej części ma istotny wpływ intensywność procesu hartowania. Większe szybkości chłodzenia powodują większy gradient temperatury, co prowadzi do zwiększonego odkształcenia termicznego w elemencie. Powstawanie naprężeń termicznych w różnych temperaturach zależy od stopnia odkształcenia oraz, w przypadku odkształcenia plastycznego, od naprężenia płynięcia w danej temperaturze. W celu dokładnego obliczenia naprężeń termicznych i odkształceń, kluczowe jest równoległe śledzenie całej sekwencji przemian fazowych wraz z ewolucją temperatury.

Zrozumienie rozkładu odkształceń i naprężeń w hartowanych warstwach ma kluczowe znaczenie dla oceny ryzyka pęknięć i innych uszkodzeń, szczególnie w komponentach stosowanych w przemyśle maszynowym, motoryzacyjnym i lotniczym. Podczas hartowania w obrabianym przedmiocie powstają różne rodzaje naprężeń, na różnych etapach hartowania.

W początkowej fazie hartowania austenit ochładza się bez przemian fazowych ze względu na znaczne gradienty temperatury. Powierzchnia kurczy się szybciej niż rdzeń, powodując naprężenia rozciągające na powierzchni i naprężenia ściskające w rdzeniu. Drugi etap rozpoczyna się, gdy na powierzchni elementu rozpoczyna się przemiana martenzytyczna. Dylatacyjne odkształcenia przemiany fazowej i plastyczność przemiany prowadzą do szybkiego rozładowania i odwrotnego obciążenia powierzchni. Nieprzekształcony rdzeń reaguje, aby zrównoważyć te

naprężenia, powodując znaczne naprężenia ściskające na powierzchni i naprężenia rozciągające w rdzeniu. Trzeci etap rozpoczyna się, gdy w rdzeniu rozpoczynają się przemiany fazowe, prowadząc do całkowitej przemiany i schłodzenia powierzchni.

Ekstrakcja odkształcenia TRIP polega na wychwytywaniu dodatkowych odkształceń plastycznych powstałych w wyniku naprężeń termicznych i mechanicznych podczas chłodzenia. Wyodrębnienie TRIP z całkowitego odkształcenia eksperymentalnie jest wyzwanie. Dlatego też metoda elementów skończonych (MES) odgrywa kluczową rolę w podejmowaniu wyzwań związanych z przewidywaniem wielu sprzężonych zjawisk fizycznych. Skuteczne przewidywanie podstawowych mechanizmów rozwoju naprężeń i rozkładu naprężeń szczątkowych jest niezbędne do projektowania zaawansowanych materiałów o ulepszonych właściwościach mechanicznych.

COMSOL Multiphysics to pakiet oprogramowania wykorzystujący MES, wykorzystywany do różnych zastosowań w fizyce i inżynierii, zwłaszcza w przypadku zjawisk sprzężonych. Oferuje konwencjonalne interfejsy użytkownika oparte na fizyce i może obsługiwać sprzężone układy równań różniczkowych cząstkowych (PDE) w słabej postaci. Do zewnętrznej kontroli oprogramowania można wykorzystać interfejs API dla języka Java i MATLAB. Modele stworzone w COMSOL Multiphysics mogą być połączone z MATLAB poprzez LiveLink w celu analizy danych, co zostało zademonstrowane w niniejszej pracy. Opracowano algorytm symulujący model, a uzyskane dane zaimportowano do programu MATLAB, w celu ich analizy graficznej. Ponadto opracowano model matematyczny wspomagający podejmowanie decyzji i przewidywanie właściwości materiałów. Dodatkowo w tej pracy wykorzystano oprogramowanie JMatPro do wygenerowania diagramu CCT i przewidzenia wpływu szybkości chłodzenia na właściwości mechaniczne materiału

Obiecującym rozwiązaniem złożoności procesu nagrzewania indukcyjnego jest opracowanie modeli zastępczych o różnych dokładnościach, które zawierają zarówno dane o wysokiej, jak i niskiej dokładności, zapewniając w ten sposób równowagę między dokładnością wyników a kosztami i czasochłonnością obliczeń. Osiągnięcie tej równowagi wymaga włączenia realistycznych informacji do modelu zastępczego. Nagrzewanie indukcyjne wiąże się ze zrównoważonym rozwojem pod względem efektywności energetycznej, przyjazności dla środowiska, precyzyjnego i szybkiego nagrzewania obszaru docelowego. Jednak nowoczesne technologie, takie jak wdrażanie uczenia maszynowego i sztucznych sieci neuronowych (ANN), które niedawno pojawiły się w tej dziedzinie, wymagają dalszego rozwoju.

České shrnutí

Hlavní příčinou vzniku tepelného stresu je kolísání teploty v ohřívaném tělese. Předpokládá se, že tepelné napětí vznikající při indukčním ohřevu neovlivňuje mechanické vlastnosti materiálu, ale proces chlazení ano. Nelinearita indukčního ohřevu však představuje problém pro proces chlazení, který následně ovlivňuje požadované mechanické vlastnosti po zakalení. Studium tepelného namáhání proto začíná analýzou rozložení teploty, řízením deformace, vznikem deformace a metalurgickými aspekty materiálu. Analýza tepelného namáhání leží na pomezí termodynamiky (přenos tepla), mechaniky pevných látek (napětí a deformace) a metalurgických jevů (fázová přeměna). Použití indukce jako zdroje tepelné energie pro analýzu tepelného namáhání činí kontrolu jevu a dosažení požadovaných výsledků náročnějšími.

Indukční ohřev je vzhledem ke své povaze náročnější na kontrolu rozložení teploty od povrchu do požadované hloubky, zejména při povrchovém kalení. Pro řešení této výzvy je důležitý vývoj digitálních řídicích mechanismů s řídicími algoritmy sladěnými se zpětnovazebním uzavřeným okruhem. To zahrnuje explicitní nebo implicitní definování procesu ve vsázce, jejich propojení se spínačem proudového toku a řízení vstupního výkonu. Tyto metody mají několik výhod, včetně dosažení požadované teploty ve stanoveném rozsahu, zabránění deformaci povrchu a neovlivnění přenosu tepla.

Při explicitní i implicitní metodě řízení událostí je napájení dodáváno přerušovaně, zapínáním nebo vypínáním spínače. Při explicitním řízení událostí je stav události definován po určitou dobu. Tato metoda je výpočetně nákladná, časově náročná, ale podmíněně stabilní a je určena pro simulaci krátkých přechodných dynamických událostí. Při implicitním řízení událostí není událost přímo definována v průběhu periody; místo toho se používá indikátor. Po dosažení bodu indikátoru se spínač vypne a poté opět zapne. Implicitní metody se obvykle používají k simulaci statických nebo méně přechodných jevů. Tyto metody pomáhají při volbě optimálního výkonu, frekvence a délky cívky v indukčním ohřevu.

Asynchronní dvoufrekvenční přístup využívá dvě různé frekvence, které jsou střídavě aktivní v závislosti na stavu události. Nižší frekvence umožňují výrazný průnik proudu a hlubší skin efekt, takže jsou účinnější pro ohřev větších dílů. Při vysokých frekvencích je průnik proudu omezen na povrch. Naopak vyšší frekvence omezují průnik proudu a ovlivňují vznik vířivých proudů uvnitř vsázky.

Rovnoměrné rozložení teploty je při austenitizaci důležité, protože deformace obvykle vznikají uvolněním zbytkových napětí nahromaděných během předchozích procesů, jako je kování nebo obrábění, a také nerovnoměrným ohřevem. Deformace způsobené procesem kalení závisí do značné míry na teplotě austenitizace, rovnoměrnosti procesu kalení a volbě kalicího média. Simulace zahrnuje dva kroky: první krok zahrnuje ohřev na teplotu austenitu, při kterém dochází ke spojeným elektromagnetickým a tepelným jevům, a druhý krok zahrnuje ochlazení na teplotu dokončení martenzitu (M_f).

Předpověď zbytkového tepelného napětí a deformace začíná sledováním tepelné historie obrobku během kalení. Rozložení teploty v kaleném dílu je ovlivněno intenzitou procesu kalení. Rychlejší ochlazování má za následek strmější teplotní gradient, což vede ke zvýšení tepelné deformace uvnitř vsázky. Vznik tepelných napětí při různých teplotách závisí na stupni deformace a v případě plastické deformace na napětí toku při dané teplotě. Pro přesný výpočet tepelného napětí a deformace je zásadní paralelně sledovat celou posloupnost fázových přeměn spolu s vývojem teploty.

Pochopení rozložení deformace a napětí v zakalených vrstvách má zásadní význam pro posouzení rizika vzniku trhlin a jiných poškození, zejména u součástí používaných ve strojírenství, automobilovém a leteckém průmyslu. Během kalení vznikají v vsázce v různých fázích kalení různé typy napětí.

V počáteční fázi kalení se austenit ochlazuje bez fázových přeměn v důsledku značných tepelných gradientů. Povrch se smršťuje rychleji než jádro, což vede k tahovým napětím na povrchu a tlakovým napětím v jádře, aby se udržel vyvážený stav napětí. Druhá fáze začíná, když na povrchu začne martenzitická přeměna. Dilatační deformace při fázové přeměně a transformační plasticita vedou k rychlému odlehčení a zpětnému zatížení povrchu. Nepřetvořené jádro reaguje na vyrovnání těchto napětí, což vede ke vzniku značných tlakových napětí na povrchu a tahových napětí v jádře. Třetí fáze začíná, když v jádře začnou fázové přeměny, které vedou k úplné transformaci a ochlazení povrchu.

Extrakce deformace TRIP zahrnuje zachycení dodatečné plastické deformace v důsledku tepelného a mechanického namáhání během chlazení. Tato extrakce TRIP z celkové deformace prostřednictvím experimentální analýzy ochlazování představuje značné výzvy. Metoda konečných prvků (MKP) tak hraje zásadní roli při řešení problémů spojených s předpovídáním více souběžných fyzikálních jevů a umožňuje je předpovídat. Mezi ně patří předpověď průběhu

teploty, fázového vývoje a vnitřních napětí během procesů kalení. Účinná předpověď a znázornění základních mechanismů vývoje napětí a rozložení zbytkových napětí jsou nezbytné pro navrhování pokročilých materiálů se zlepšenými mechanickými vlastnostmi.

COMSOL Multiphysics je softwarový balík pro analýzu konečných prvků (MKP), řešení a simulaci, který se používá pro různé fyzikální a technické aplikace, zejména pro sdružené úlohy a multifyziku. Nabízí konvenční fyzikální uživatelská rozhraní a dokáže zpracovávat sdružené systémy parciálních diferenciálních rovnic (PDE) ve slabé formě. K externímu ovládání softwaru lze použít rozhraní API pro Javu a MATLAB. Modely vytvořené v COMSOL Multiphysics lze propojit s MATLABem prostřednictvím LiveLink pro analýzu dat, jak je ukázáno v této práci. Byl vytvořen algoritmus pro simulaci modelu a výsledná data byla importována do MATLABu pro grafickou analýzu. Dále byl vyvinut matematický model, který pomáhá při rozhodování a předpovídání vlastností materiálů. Kromě toho byl v této práci použit software JMatPro k vytvoření diagramu CCT a předpovědi vlivu rychlosti chlazení na mechanické vlastnosti materiálu.

Slibným řešením složitosti indukčního ohřevu je vývoj náhradních modelů s více věrnostmi, které zahrnují jak údaje s vysokou, tak s nízkou věrností, čímž se dosáhne rovnováhy mezi přesností předpovědi a výpočetními náklady. Dosažení této rovnováhy zahrnuje začlenění realistických informací do konstrukce náhradního modelu. Indukční ohřev s sebou nese udržitelnost z hlediska energetické účinnosti, šetrnosti k životnímu prostředí, přesného ohřevu cílové oblasti a rychlých metod ohřevu. Moderní technologie, jako je implementace strojového učení a umělých neuronových sítí (ANN), které se v této oblasti nedávno objevily, však vyžadují další rozvoj.

Thesis outline

The present thesis concentrates on the analysis of thermal residual stress in steel metal induced by induction heating. The document is structured as follows: Chapters 1 and 2 introduce induction hardening, covering aspects of heating and cooling. Chapters 3 to 6 delve into technical numerical modelling of induction heating, calibration, and optimisation of power control, mathematical modelling of thermal residual stresses, and modelling of thermal strain modelling, including TRIP strain. Finally, Chapter 7 discusses the conclusions and perspectives.

In Chapter 1, a general introduction to induction surface hardening is provided, along with a review of current research developments. The chapter also outlines the research gap, establishes objectives, and presents an overview of the dissertation.

In Chapter 2, a comprehensive review and discussion of the current state-of-the-art in relevant literature is presented. It explains the fundamental mechanisms of heat generation and introduces key concepts related to induction heating. The discussion includes an explanation of penetration depth, critical frequency, and efficiency, which are essential in the context of surface hardening. The chapter also addresses up-to-date research on topics such as quenching, thermal stress and strain, phase transformation, optimisation of data acquisition process, and effect of cooling parameters of surface hardening.

In Chapter 3, a regulation of heat generation within the workpiece is investigated with the aim of achieving the target temperature at the desired location and time through the control of power input. The study involves a comparison of various power control mechanisms, unveiling the potential to influence events both on the surface and inside the workpiece. This chapter introduces a mathematical and numerical model that elucidates the processes that occur on the surface of the workpiece during IH. Simulation of events on the surface, illustrating the temperature inside the workpiece as functions of time and process parameters.

In Chapter 4, a mathematical model for the thermal stresses arising from induction surface hardening in axisymmetric geometries is formulated. The distribution of strains and stresses, originating from thermoelastic, thermoplastic, and transformation processes, is determined in the surface layers. Computational analyses are presented for the exemplary hardening of the induction surface of a cylinder made of steel AISI 4140. The phase decomposition rate, the time evolution of the radial stress, and the dependence of the yield stress in both austenite and martensite on the

temperature are comprehensively described. In addition, an equation is developed that governs the heating and cooling processes during phase transformation.

In Chapter 5, a calibration of the induction hardening model for gear wheels is undertaken. This process requires high precision and must be based on a reliable mathematical model and the correct selection of input parameters. The mathematical model is elucidated as follows: The forward problem articulates the process through partial differential equations, whereas the backward problem involves the proposal of a surrogate model. The methodology is illustrated through an example provided on a gear wheel model manufactured from AISI 4340. The chapter also describes the continuous cooling transformation (CCT) diagram associated with the model.

In Chapter 6, the influence of TRIP strain on the mechanical properties of steel during martensite transformation is depicted through FE analysis. FE analysis is a vital method used for predicting multiple physical phenomena that occur simultaneously. The thermo-elastic-plastic properties of AISI 4140 steel are discussed, including TRIP strain, along with a mathematical model of the process and phase transformation. The chapter also elucidates the impact of the cooling rate on the hardness, strength, and general mechanical properties of steel, supported by illustrative examples.

In Chapter 7, the research conclusions (summary of key finding and contribution to the field) and the perspective of potential future work are provided.

Table of Contents

List of Figures

List of Tables

Nomenclature

Roman letters

A Magnetic vector potential

B Magnetic flux density

C Emissivity

c_p Specific heat capacity at constant pressure

D Electric flux density

E Electric field intensity

E Young's modulus of elasticity

e_v Volumetric dilatation

f Frequency

G Shear modulus

H Magnetic field strength

H_i Enthalpy of the transformation for each phase

I Current

J Current density

$\boldsymbol{J}_s$ Source current density

$\boldsymbol{J}e$ Eddy current

k Thermal conductivity

K Transformation plasticity coefficient

l Length

Q Heat energy generated in the material

r Inner radius

R Outer radius

S_m Mean applied stress

t Required heating/cooling time

T Temperature

T_C Curie temperature

Greek letters

α Linear coefficient of thermal expansion

β_t Volumetric thermal expansion coefficient

γ Electrical conductivity

δ Penetration depth

δ_{ij} Deformation

ε Strain

μ Magnetic permeability

μ_0 Magnetic permeability of the vacuum

μ_r Relative magnetic permeability

μ_s Shear modulus

ν Poison's ratio

ξ_i Volume percentage of phase i

ρ Electrical resistivity

ρ_m Mass density

σ Thermal stress

σ'_{ij} Deviator stress tensor

σ_e Effective stress

σ_y Yield stress

τ Shear stresses

ω Angular frequency

Acronym

AC Alternating current

Ac_1 Lower critical point

Ac_3 Upper critical point

CCR Critical cooling rate

CCT Continuous cooling transformation

DC Direct current

DF Dual frequency

DOFs Degrees of freedom

FEA Finite element analysis

FEM Finite element method

FVM Finite volume method

HF High frequency

HI Induction heating

ISH Induction surface hardening

MF Medium frequency

Ms Martensite start

M_f Martensite finish temperature

PSA Photoelastic stress analysis

SFIH Single frequency induction hardening

SDF Simultaneous dual frequency

SDFIH Dual frequency induction hardening

TRIP Transformation induced plasticity

TSA Thermoelastic stress analysis

TTIH Tooth-by-tooth induction heating

TTT Time-temperature transformation

Chapter 1

Introduction

1.1 General introduction

Induction heating (IH) technology has been in continuous evolution following industrial and technological progress since the late nineteenth century (Mühlbauer, 2008). The foundational principle of IH was discovered by Michael Faraday when he observed induced currents caused by a magnet. Subsequently, James C. Maxwell formulated the unified theory of electromagnetism, and James P. Joule elucidated the heat generated by a current in a conductor, thereby establishing the fundamental principles of induction heating.

IH is a technology that employs an alternating current (AC) magnetic field to generate power in an electrically conductive material (Lupi et al., 2015; Sadeghipour et al., 1996; Tudbury, 1974). Passing AC through a conductor generates an AC magnetic field, leading to the development of AC within the workpiece. This, in turn, results in heating due to resistive and hysteresis losses. Induction heating uses both heat generation inside the workpiece (through an induced current) and conduction heat transfer due to the activated kinetic energy of the molecules (eddy current loss), which is a reason why induction heating is too fast. Induction heating is highly efficient (Patil & Bhadade, 2015), fast heating, cleanness, and more precise temperature control than traditional methods (Davies & Simpson, 1979).

The key advantages of heating technologies with internal sources (electromagnetic/induction heating) include:

- High-specific heating power
- Reduced process time
- Precise control of the process

Furthermore, as electrotechnology for heating typically enhance overall process efficiency, it serves as a solution for a rational and efficient use of energy (Lupi et al., 2015).

Numerical modelling can be applied in induction heating to simulate and understand heat transfer processes, optimise system design, and evaluate the performance of different heating configurations and parameters (Demidovich, 2012). Design, control and modelling of induction heating systems have evolved over time, marked by the introduction of solid state converters and

the adoption of numerical methods for load behaviour analysis (Martín Segura & Montesinos Miracle, 2012).

Modelling the thermal behaviour of materials during induction heating processes is crucial to optimise the entire process (Liu & Rao, 2009), which is important in high energy experiments, where both thermal and mechanical stresses are high (Wetz et al., 2011). It facilitates the proposal of efficient energy strategies, significantly reducing time and effort in the design process.

The complexity of material properties during induction heating, especially drastic changes with temperature, necessitates the use of powerful numerical tools such as finite element analysis (Sadeghipour et al., 1996). It can help in predicting the hardness profile in case of hardening processes, but their accuracy is limited by the complexity of the coupling between electromagnetic and thermal fields and the non-linear behaviour of material properties (Barka et al., 2006).

1.2 Research gaps

Induction heating (IH) is a versatile heating technology for conductive materials due to its high power density, high energy efficiency, and the capability for local reheating (Lucia et al., 2014). Some literature has proposed various approaches employing multiple working coils and multiple inverters to regulate temperature and heat distribution in a workpiece (Lucía et al., 2010; Ngoc et al., 2011). A system comprising multiple working coils and multiple inverters has also been documented in (Green, 1996) for controlling the current amplitude through each corresponding working coil independently of the others. However, it is challenging to control the current amplitude due to mutual inductance or electromotive force (EMF) caused by magnetic couplings between the working coils. In addition, a high-frequency voltage-source inverter lacks the inherent capability to independently control its output power. Consequently, the output power of such an inverter must be regulated by adjusting the DC input voltage (Fujita & Akagi, 1996).

An approach involves employing single inverter, multiple working coils, and mechanical or semiconductor switches to achieve controlled heat distribution (Forest et al., 2000; Rodriguez & Leeb, 2006, 2010). Switches are utilised to precisely control the average amplitude of the coil current by adjusting the connection configuration of the working coils, whether in series, parallel, or more complicated arrangements. However, achieving the desired heat distribution is challenging, as these approaches lack the capability for continuous control of the coil current amplitude.

The Zone-Controlled Induction Heating (ZCIH) system has the ability to regulate the distribution of exothermic heat on the workpiece, mitigating the strain induced by thermal expansion (Fujita et al., 2007, 2011; Ha Pham Ngoc et al., 2009; Miyagi et al., 2006). However, there is a nonlinear relationship between the current amplitude and coil current, leading to heating not only of the corresponding zone, but also of other zones. The interaction between the two working coils generates additional heat between them, altering the profile of the heat distribution. (Ha et al., 2010; Sasayama et al., 2015) concluded that finite element methods (FEM) are necessary to determine appropriate current references to achieve a desirable heat distribution.

To address the performance limitations of induction heating, several manufacturers have suggested overcoming this challenge through simultaneous dual-frequency heating. The simultaneous dual frequency (SDF) heating method uses two different currents, medium frequency (MF) and high frequency (HF), to uniformly harden the surface layer of the workpiece (i.e., shafts, sprockets, and gear) with consistent contour thickness(Esteve et al., 2005a). This method involves a single coil and two inverters, typically coupled through transformers (Okudaira & Matsuse, 2000; Porpandiselvi & Vishwanathan, 2015). MF and HF currents are used simultaneously, with independent control. This allows the regulation of output power to control the hardening depth at both the root and the tip of the gear (Barglik et al., 2021a; Esteve et al., 2015). Furthermore, a recent trend among researchers involves the adoption of a single power converter to achieve simultaneous dual-frequency operation, as proposed by several authors (Bi et al., 2016; Porpandiselvi & Vishwanathan, 2015).

Induction hardening typically comprises two stages: first, intense heating of the workpiece to the desired depth without affecting the edge, followed by rapid cooling below the temperature at which transformation begins (Popov, 2019). This process poses challenges due to the non-linearity of the process parameters in controlling the thickness of the hardness (Kayacan & Çolak, 2004). To identify precise parameter values, optimisation is an essential approach for achieving quality output. Various researchers emphasise optimising process parameters such as feed rate (mm/s), current, frequency, heating time, and the gap between the workpiece and the coil to achieve maximum depth with minimum edge effects (Kobayashi et al., 2013; Rudnev et al., 2003.; Zhang et al., 2019).

Totik et al., 2003 examined heating time (feed rate) and temperature as process parameters, finding that induction heat treatment led to enhanced wear characteristics depending on the

selected process parameters. Researchers (Ge et al., 2006) analysed the correlation between hardening parameters, specifically focussing on voltage and current control of the power supply, heating time control, and part speed control in the context of scan induction hardening. The authors proposed that future efforts should be directed toward optimising the control of the induction hardening process. Asadzadeh et al., 2021 employed a neural network for the estimation of the unspecified parameter in a physical model representing a certain physical process. Naar & Bay, 2013 conducted an optimisation on frequency and current density to achieve a specific temperature rise within a fixed time frame. However, induction hardening involves multiple design parameters, including electromagnetic, thermal, metallurgical, and mechanical fields. Each of these fields comprises design parameters contributing to the quality of the output. Single-objective optimisations have limited scope in this context.

Optimisation is crucial in the design of induction hardening systems (Chereches, 2011). In an alternative approach, (Kohli & Singh, 2011; Qin et al., 2017) used a response surface method (RSM) to explore and optimise the impact of five process parameters (feed velocity, input power, gap, curvature, and flow rate) on temperature, microstructure, microhardness, and phase transformation geometry during continuous spot induction hardening. In (Kayacan & Çolak, 2004), a fuzzy approach was employed to investigate the influence of coil airgap, material diameter, cooling time, power, and frequency on hardening depth and heating time. However, with multiple design parameters, single-objective optimisation can only address them sequentially, lacking the ability to account for the influence of one parameter over the other. Therefore, the set of feasible solutions, considering design restrictions, is considered optimal when it expresses all the objectives, with no other solutions in the search space surpassing them.

Controlling the hardness thickness in induction hardening is highly complex due to the numerous parameters that influence it. Obtaining exact values of parameters for hardness thickness is challenging due to the non-linearities of induction heating (Kayacan & Çolak, 2004). However, the desirability approach enables the transformation of the multi-objective optimisation problem into a single-optimisation problem by incorporating expert knowledge to set weights in the desirability function. Minimising residual thermal deformations, enforced by an additional straightening operation, results in an increase in process duration and costs (Dziatkiewicz et al., 2023). This approach tackles the multi-criteria optimisation challenge in industrial settings for the

induction hardening process, utilising a hybrid method that integrates empirical modelling and computational intelligence tools.

Model calibration involves identifying a unique set of model parameters that effectively describe the behaviour of a system. This is achieved by comparing and adjusting the model predictions through a confrontation with actual measurements conducted on the system. Ensuring a uniform temperature distribution in complex-shaped semi-finished products, especially in specific corner zones, poses a challenging and unresolved task (Pleshivtseva et al., 2022). The solution lies in optimising the design parameters and operation modes of the induction system for the surface hardening process. Current trends in optimisation emphasize the widespread use of numerical models specific to problems (Spezzapria et al., 2016; Tong et al., 2017).

The objective of induction hardening is to achieve a hardened martensitic layer on the surface of a component while preserving the unchanged core microstructure. The depth of the heated layer is influenced by process parameters such as frequency, current intensity, and time, as well as material properties. Following the heating process, quenching is typically performed using a sprayer or immersion in a quenching medium. Rapid cooling of the austenitized area promotes its transformation into a hard martensitic microstructure. In a comprehensive study by (Areitioaurtena et al., 2022; X. Wang et al., 2019), both numerical and experimental investigations were carried out, demonstrating excellent agreement between the simulated and experimentally measured results in the context of scanning induction hardening. However, there was a lack of information on the specific FE model used.

The development of FE analysis has progressed in both electromagnetic and thermal stress modelling, incorporating phase transformations in induction hardening. This advancement helps to comprehend and resolving industrial problems (Şimşir & Gür, 2008). However, there is still a complexity of data acquisition given the challenging nature of determining the parameters of the material and the process. This challenge becomes particularly pronounced in high-power density applications, such as contour hardening of gears.

The interdependence of permeability, resistivity, specific heat, and temperature, combined with the atypical behaviour of steel near the Curie point, introduces challenges in analysing the evolution of the heating power density profile during induction heating. It can be shown that the depth of the skin represents the layer where 86% of the induced power is concentrated, and at this depth the current is 37% of its surface value. The assumption of the exponential decay of current

density is accurate only for materials with constant electrical resistivity and magnetic permeability, but it can be misleading in surface hardening scenarios (Prisco, 2018). However, recent advances in computer technology have enabled the computerised modelling of the induction process, leading to enhanced material characterisation and improved control of the overall process.

In much literature, a mathematical model has been established to predict the volume fraction of martensite and hardness for the materials under investigation (Fang et al., 2018; Hömberg, 2004a; Karban & Donátová, 2010). However, in many existing mathematical models, limitations are observed in accurately predicting martensite's hardness and volume fraction at any specific location within the induction-hardened zone of a given steel component. They inherently lack the capability to adequately describe the strain hardening behaviour of steels across the entire range (Fujita et al., 2011). The complexity of this phenomenon surpasses conventional hardening when including the analysis of the TRIP effect.

The TRIP effect encompasses three phenomena: the development of a strain component due to volume change induced by transformation, the generation of a plastic strain component resulting from the stress field accompanying the transformation, and an additional hardening during plastic deformation caused by the transformation, where martensite exhibits a higher flow stress than austenite (Fischer et al., 2000a; Post et al., 2008). The reality is that all three effects occur simultaneously during the transformation and make it more complex.

TRIP strain refers to plastic deformation observed during microstructural transformations under nonzero stresses (Rohde & Jeppsson, 2000). The Greenwood–Johnson mechanism explains this phenomenon as the weaker phase undergoing plastic deformation to accommodate volumetric changes during phase transformations. Besides phase transformations and stress state, factors like austenite grain size have been linked to TRIP strain (Boudiaf et al., 2011). However, there is limited literature on this subject to date. Researchers (Montalvo-Urquizo et al., 2013), assert that TRIP should not be neglected, as it enhances the numerical prediction of residual stresses.

Numerous studies in the literature have extensively addressed austenite factors that influence the stability and the kinetics of its transformation during thermal or deformation-induced transformation (Blondé et al., 2014; Matsuoka et al., 2013). However, most existing models focus on predicting austenite stability and transformation kinetics under either thermal conditions (Van Bohemen & Sietsma, 2009) or mechanical conditions (Matsumura et al., n.d.; Sherif et al., 2004). In the context of thermomechanical processes, it is emphasised that models integrating both

thermal and mechanical effects can offer a more precise estimation of phase contents and transformation temperatures. A smaller grain size enhances the thermal stability of austenite and lower M_s temperatures (Blondé et al., 2014; Matsuoka et al., 2013). The larger grains exhibit a lower carbon content and have reduced mechanical stability, since carbon is a stabilising factor for austenite.

Austenite stability can be divided into thermal stability and mechanical stability, depending on external driving forces (cooling or stress). Both thermal and mechanical stability are susceptible to the influence of intrinsic and extrinsic factors. Extrinsic factors, such as stress from neighbouring grains due to varying thermal expansion ratios, can impact the thermal stability of austenite during the cooling process (Vandijk et al., 2005). Intrinsic factors refer to the austenite grain domain defined by its grain boundaries, which encompasses interstitial/substitutional atoms (chemical composition), dislocations, and grain boundaries (grain size/morphology). Extrinsic factors are forces applied by adjacent grains, involving stress/strain partitioning (He, 2020; Prisco, 2018).

In general, more research is needed to address a detailed understanding of the thermal residual stress contributing to surface induction hardening in various aspects. These aspects comprising temperature-controlled induction heating, combined parameter optimisation, and the analysis of thermal strain, including the TRIP strain in steel materials, are summarized as follows.

- Numerical modelling is a powerful and essential approach to address the complex behaviours associated with induction heating. A high-frequency voltage-source inverter lacks the inherent capability to independently control its output power. Consequently, the output power of such an inverter must be regulated by adjusting the DC input voltage. The automatic power control, regulated by a feedback control loop, indirectly governs heat transfer within the workpiece, adhering to Fourier's law of conduction. However, these power control strategies may lead to increased switching losses and electromagnetic noise, as it is impractical for switching devices to always turn on and off at zero current. But, it is possible to reduce switch losses and optimise energy efficiency.
- The emphasis on multiple objective parameter optimisation underscores the need for widespread utilisation of numerical solutions, problem-specific mathematical models, and evidence-based verification are crucial aspects that need work. Single-objective optimisation lacks the ability to account for the influence of one parameter over another,

especially in induction hardening, where multiple design parameters span electromagnetic, thermal, metallurgical, and mechanical fields. Each of these fields encompasses design parameters that contribute to the quality of the output. Therefore, the model calibration strategy involves identifying a unique set of model parameters that effectively describe the system's behaviour and optimise the design parameters and operation modes of the induction surface hardening system.

- The complexity of surface hardening surpasses conventional methods when considering the analysis of the TRIP effect. As conductors approach their Curie point, electrical resistivity and magnetic permeability can be misleading in surface hardening scenarios. The challenge lies in the complexity of data acquisition, given the difficulty of determining the material and process parameters. This challenge becomes particularly pronounced in high-power density applications, such as contour hardening of gears. Therefore, the preferred approach involves advanced computer modelling, which enables the computerised simulation of the induction process, leading to improved material characterization and improved control of the overall process.
- TRIP strain refers to plastic deformation observed during microstructural transformations under nonzero stresses. It should not be neglected, as it enhances the numerical prediction of residual stresses and encompasses three phenomena that occur simultaneously during the transformation: (1) the development of a strain component due to volume change induced by the transformation, (2) the generation of a plastic strain component resulting from the stress field accompanying the transformation, and (3) additional hardening during plastic deformation caused by the transformation, where martensite exhibits a flow stress higher than austenite.
- A clear understanding of the primary elements that influence the stability of retained austenite is a critical aspect of the martensite transformation. In the context of thermomechanical processes, it is emphasised that models integrating both thermal and mechanical effects can provide a more precise estimation of phase contents and transformation temperatures. However, many existing mathematical models exhibit limitations in accurately predicting the hardness and volume fraction of martensite at any specific location within the induction-hardened zone of a given steel component. They

inherently lack the ability to accurately describe the strain hardening behaviour of steels throughout the entire range.

1.3 Work motivation

Thermal stresses arise when a material undergoes a temperature change in the presence of constraints. There are two types of constraints associated with thermal stresses: external constraints and internal constraints. External constraints refer to restrictions on the entire system that prevent it from expanding or contracting when subjected to temperature variations. Internal constraints, on the other hand, arise within the material itself because different locations within the material experience varying degrees of expansion or contraction, while the material must remain continuous. In the internal constraint, thermal stresses will occur due to the lack of independent movement between the inner and outer layers of the material. The objective of this research work is specifically to investigate the thermal stress created due to internal constraints.

Exploring the origins and nature of thermal stresses is important because these stresses can lead to fracture or undesirable plastic deformation (Callister & Rethwisch, 2015). There are three main causes of thermal stresses: (1) stress resulting from restrained thermal expansion and contraction, (2) stress resulting from a temperature gradient, and (3) thermal shock for ductile materials. In situations where a homogeneous and isotropic workpiece is heated or cooled uniformly, with no imposed temperature gradients, the workpiece undergoes free expansion or contraction and remains stress-free. However, if the axial motion of the workpiece is restricted by rigid end supports, thermal stresses are introduced.

When a solid body undergoes heating or cooling, its internal temperature distribution is influenced by factors such as its size and shape, the thermal conductivity of the material, and the rate of change of temperature. Thermal stresses can arise due to temperature gradients across the body, often caused by rapid heating or cooling. In such cases, the exterior experiences temperature changes more rapidly than the interior, leading to differential dimensional changes that restrain the free expansion or contraction of adjacent volume elements within the material. For instance, during heating, the outer regions of a sample become hotter and expand more than the interior areas. Consequently, compressive surface stresses are induced and counterbalanced by tensile interior stresses. The stress conditions between the interior and exterior are reversed during rapid cooling, putting the surface in a state of tension.

Thermal fatigue cracking significantly affects the surface finish of the tool and the cast products (Persson, 2004). This can be mitigated by using purely martensitic microstructures and high-strength materials (Z.-C. Lin et al., 1994). The resistance to thermal crack propagation of surface-engineered tool steels is primarily determined by the mechanical properties of the substrate material. Surface-engineered materials are successfully used to improve erosion and corrosion resistance, but their resistance against thermal fatigue needs further exploration (Persson et al., 2005).

Thermal residual stress is a fundamental aspect of induction hardening, contributing to the transformation of the microstructure, creating a hardened surface layer, and improving the wear resistance in metal components. Understanding the status of thermal stress in a workpiece is crucial for controlling the parameters of the induction hardening process, ensuring an optimal balance between hardness and other mechanical properties. This careful control helps minimise the potential for undesirable effects, such as cracking or distortion, resulting in improved performance and durability of hardened components.

Residual stresses can arise from various mechanisms, such as plastic deformations, temperature gradients, or structural changes (phase transformation). If the deformation occurs during the cooling period and remains within the elastic range, no residual stress persists after reaching the equilibrium temperature. Additionally, beyond this simple thermal stress, another stress resulting from structural changes may be present if the metal is heated above the critical transformation point and subsequently quenched. For example, when steel is heated above the upper critical point Ac_3 and then rapidly cooled, the shape and size of the volume elements undergo differential changes due to structural transformations.

To delve into the evolution of residual stress during induction hardening, let us examine the quenching process applied to a steel cylinder. Steel is an alloy composed of iron (Fe) and carbon (C). At room temperature, the solubility of carbon in steel is negligible. Carbon segregation as cementite (Fe_3C). However, by heating the steel above its austenitisation temperature, a crystal structure is achieved in which carbon can dissolve. Rapid cooling prevents carbon segregation (Geijselaers, 2003). The resulting structure, martensite, is exceptionally hard and exhibits excellent corrosion resistance. A critical factor in these processes is the time required for carbon to dissolve and homogenise within the austenite.

1.4 Objectives

The general objective of the research work is to investigate the development of thermal stress in steel workpieces during induction hardening and its influence on the mechanical properties of the material. The goal is to enhance the understanding of the fundamental principles governing thermal stress development and to optimise industrial processes. This general objective has been subdivided into four sub-objectives to achieve the goal of the dissertation.

1. Numerical modelling of induction heating to control the surface temperature while maintaining heat transfer in the radial direction to achieve the target temperature at a specified depth. This is achieved through the automation of feedback control mechanisms that adjust the input parameters. Controlling the temperature distribution by adjustment to the input parameters is regarded as a means of governing the entire system in induction heating. This is because all properties exhibit variations on the temperature gradient.
2. Optimal calibration of model-based controllers for induction surface hardening. In this work, model calibration has done to optimise induction surface hardening, wherein heat transfer computations are based on time-temperature data. This calibration strategy integrates key parameters to achieve the most effective combination for the specified application, achieved by controlling the heat flow and ensuring optimal energy efficiency.
3. Mathematical modelling of thermal stresses in induction surface hardening. In this work thermal residual stress resulting from volume changes due to temperature variations and phase transformations, and its effects on other mechanical properties has investigated. Changes in steel density levels can also be used to characterise both thermal and transformation strains in a unified way. The distribution of stress and strain on the surface layer of the steel material subjected to induction hardening is caused not only by thermoelastic processes but is often influenced by plastic deformations in the exposed layers and the transformation of the level of steel.
4. Investigation of the thermal and TRIP strain effect on the mechanical properties of steel AISI 4140. In this chapter, the combined effect of thermal and TRIP strain on the mechanical properties of the material has been investigated. The study aimed to demonstrate the influence of the cooling rate, perform a simulation of the sensitivity analysis, and explore the phase transformation rate from austenite to martensite.

Chapter 2

Literature review

2.1 Basics of induction heating

Induction heating is a technique to increase the temperature of an electrically conductive material by exposing it to an alternating electromagnetic field (Araneo et al., 2008; Balanis, 2012). When a conductor is exposed to a varying magnetic field, the magnetic flux passing through it changes over time. Consequently, electromagnetic induction occurs, leading to the induction of an electromotive force (EMF) in the conductor, which gives rise to eddy currents (Esteve et al., 2005b). These eddy currents circulate within the conductor in closed loops, creating localised magnetic fields that oppose the change in the original magnetic field.

In most practical applications of induction heating in metals, where the frequency of current is less than 10 MHz, the displacement current, $\partial D/\partial t$ is much smaller than the induced current density **J** (Hetnarski, 2014). Neglecting the displacement current, the Maxwell equations can be expressed in the form (Rudnev et al., 2003.)

$$i\omega\lambda \boldsymbol{A} - \frac{1}{\mu}\nabla^2 \boldsymbol{A} = \boldsymbol{J}_s, \tag{2.1}$$

where ω is the excitation frequency, $\boldsymbol{J}_s$ is the source current density, and μ is the magnetic permeability.

The heat transfer equation governs transient temperature distributions in workpieces and can be written as

$$\rho_m c_p \frac{\partial T}{\partial t} - \nabla \cdot (k\nabla T) = \dot{Q}, \tag{2.2}$$

where ρ_m is the mass density, c_p is the specific heat capacity at constant pressure, k is the thermal conductivity, and $\dot{Q}$ is the energy generated in the material per unit volume and time.

$$\dot{Q} = \frac{1}{2\gamma}|\boldsymbol{J}_e|^2, \tag{2.3}$$

where $\boldsymbol{J}_e$ is the eddy current in the workpiece, $\boldsymbol{J}_e = -i\omega\lambda\boldsymbol{A}$, γ is the electrical conductivity, **A** is the magnetic vector potential.

The current density distribution is influenced not only by temperature-dependent resistivity but also by the local values of magnetic permeability, which depend on temperature and the local magnetic field intensity.

Skin Effect: The current density in the conductor or magnetic flux decreases from the surface towards the internal part of the body. The penetration depth in a homogeneous and linear conducting medium is given as (Lupi et al., 2015),

$$\delta = \sqrt{\frac{2}{\omega\mu\gamma}} = \sqrt{\frac{2\rho}{\omega\mu_0\mu_r}}, \tag{2.4}$$

where δ is the penetration depth, (m), $\omega = 2\pi f$ is the pulsation of the electromagnetic field, (rad/s) and magnetic permeability of the vacuum, $\mu_0 = 4\pi \cdot 10^{-7}, H/m$, ρ is the electrical resistivity $(\Omega \times m)$, and μ_r represents is the relative magnetic permeability. Penetration depth can be expressed in the more convenient form,

$$\delta = 503\sqrt{\frac{\rho}{\mu_r f}}. \tag{2.5}$$

Proximity Effect: If AC flows through two conductors, the distribution of current density is influenced by the distance between them and the actual direction of the currents.

Ring Effect: In bent or ring-shaped conductors carrying DC or AC, the highest current density is concentrated on the inner surface of the ring.

End and edge effects: It vary with different geometrical orientations of the workpiece and inductor. These distributions are influenced by the skin effect and heat transfer conditions as well as by the electromagnetic field distortion occurring in the end regions of inductors and at the edges of workpieces.

2.2 Coupling phenomena of the induction hardening process

The conventional hardening process begins with heating the material to the austenite phase followed by rapid cooling. As the temperature increases beyond a critical point during heating, ferrite begins to transform into austenite. The structure becomes entirely austenitic once it surpasses Ac_3. Upon cooling, the austenite phase undergoes transformation into various phases, depending on the cooling rate. In the irreversible deformation of an iron-based alloy during and after a martensitic phase transformation, two key factors are responsible (Majaty et al., 2018; Nagayama et al., 2001a).

1. The accommodation process, driven by the volume change in the transformation and the shear τ that leads to additional elastic and plastic strain, results in a compatible deformation and strain.
2. The orientation process is triggered by the formation of preferred variants that may align themselves in partially self-accommodating groups.

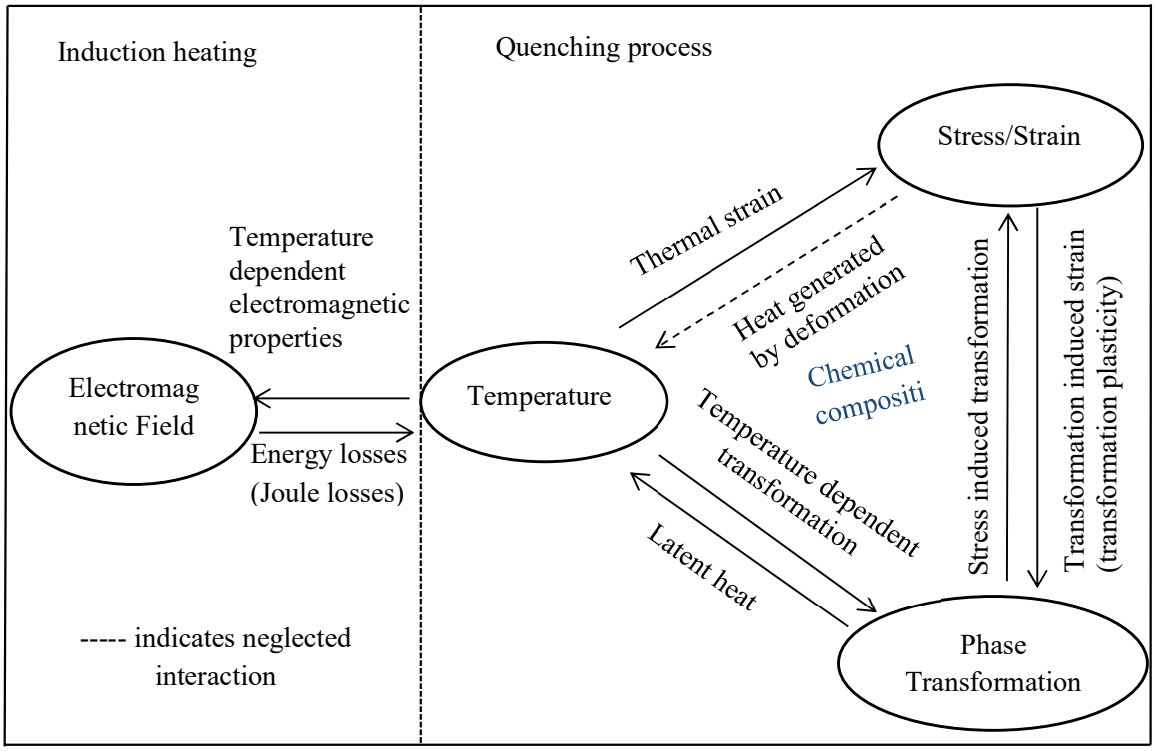

Figure 2.1: Induction hardening process, encompassing induction heating (left) and subsequent cooling (right), along with the associated phenomenological coupling relationships (Hömberg, 2004a; Taleb & Sidoroff, 2003).

2.3 Thermal stress in materials

Thermal stress refers to stress induced by variations in temperature. When a material is rapidly heated or cooled, a temperature disparity arises between its surface and interior. This disparity leads to rapid thermal transition that induces thermal expansion or contraction, resulting in localised movement within the material and generating thermal stresses. If a material is heated or cooled uniformly, there are no temperature gradients, ensuring the workpiece remains free of stress. Without constraints there would be no stresses (Barron & Barron, 2012.).

The primary factor driving stress and strain accumulation during heating is the non-uniform thermal expansion (resistance to this expansion) caused by induced temperature gradients. However, metallurgical phase transformations and structural changes also contribute to the stress distribution within the workpiece (Radionov & Karandaev, 2020; Rudnev et al., 2003). Throughout the heating process, phase transitions and variations in specific volumes occur across different phases and structural morphologies. Consequently, changes in the stress distribution and magnitude arise due to discrepancies in the mechanical properties of these distinct phases.

Following heating, the subsequent cooling (i.e., quenching) led to the development of compressive stresses on the surface. At the initial stage of the cooling process, the temperature distribution underwent a complex evolution. The core temperature continued to increase as heat was conducted from the warmer outer regions as the temperatures at the surface decreased. Eventually, it reached a peaked temperature, and the surface temperature reached its lowest value. This quenching process resulted in the formation of a thin surface layer of martensite, which possesses a specific volume compared to the initial microstructure.

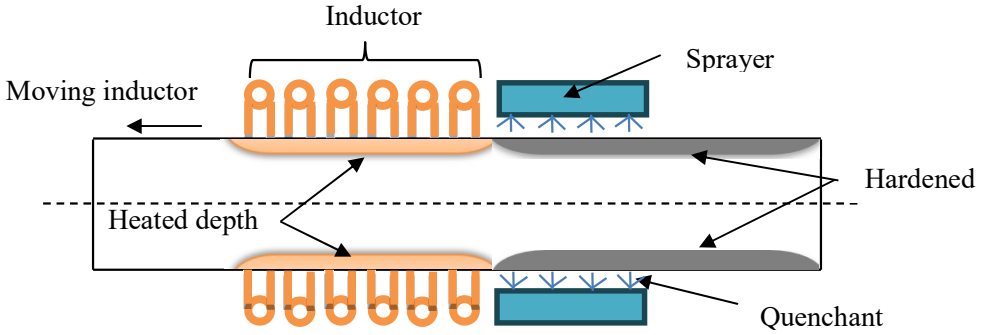

Figure 2.2: Induction hardening setup (Areitioaurtena et al., 2020)

Table 2.1: Geometric data

Length of the workpiece	100 mm
Diameter of the workpiece	40 mm
Workpiece material type	AISI 4140 steel
Number of copper winding	6
Diameter of the copper wire	10 mm
Distance between the centre of two copper wires	16 mm

Gap between the workpiece and copper winding	3 mm
Quenchant (water) velocity	1 m/s
Speed of the inductor and sprayer	0.5 to 2 mm/s

The condition of thermal stresses during and after the quenching process can result in one or more of the subsequent issues, depending upon the quenchant type and material composition:

- Formation of quench cracks
- Distortion of the component
- Change in service properties
- Distortion during machining

Quench cracks can occur when the stress during quenching exceeds the fracture stress of the material, although the exact stress levels needed for this to happen are usually uncertain. The appearance of these cracks is typically unpredictable and heavily influenced by the geometry of the component, which has a significant impact on the stress distribution (Mao et al., 2000).

A significant implication is the impact of residual stresses on the service properties of the component, especially in corrosive environments. Surface tensile stress can increase the vulnerability to stress-corrosion cracking, whereas compressive residual stress will modify the fatigue strength of the component (Samuel & Prabhu, 2022a).

Plastic distortion of components may occur if the stress generated during quenching exceeds the elastic limit. These distortions present considerable challenges, especially when precise dimensional tolerances are required. The distortions that arise from elevated stress levels during quenching can manifest itself as changes in volume, shape, or warping (Chen et al., 2019a; Mao et al., 2000).

2.4 Factors influencing the development of thermal stresses

In numerous studies (Hetnarski & Eslami, 2019; Reza Eslami et al., 2013; Toparli et al., 2002), it has been acknowledged that the formation of thermal stress and strain during and after the quenching process of steels is influenced by the following factors:

- Geometry of the component
- Temperature gradients
- Thermal contraction due to cooling

- Expansion resulting from the transformation of austenite into other phases
- Viscous phenomena
- Transformation-induced plasticity

Geometry of the component: The geometry of an object significantly affects the creation of thermal stress and strain. Thermal residual stresses self-adjust when the component is not restrained externally. Typically, the stress pattern is symmetric about the centre of the body, reflecting the cooling pattern of symmetrical nature. Additionally, the impact of the component's edges and ends is crucial; residual stress and strain within a material diminish toward zero at its free surface (Silva et al., 2005).

Temperature gradients: The root cause of thermal stress generation during quenching lies in the variation of temperature within the body. The largest temperature gradient occurs early in the quenching process but diminishes gradually as the body's temperature approaches that of its surroundings. These thermal gradients, resulting from different cooling rates, drive volume changes, and consequently, the development of thermal stresses (Gür & Pan, 2009; Hetnarski, 2014). Thermal gradients and contraction in the quenched body are significantly affected by both the severity of the quenched medium and the thermal properties of the material. A more severe quenching process leads to higher temperature gradients and increased material deformation (Carlone et al., 2010).

Thermal contraction due to cooling: Sequential development of transformation products (i.e., ferrite, pearlite, bainite, or martensite) is linked to the expansion of the material. The extent of this phenomenon varies depending on the type of phase change, such as from austenite to ferrite or pearlite or from austenite to bainite or martensite. The formation of these transformation products is influenced by the temperature and the rate of cooling.

Figure 2.3 illustrates how the cooling rate influences the yield stress during the quenching process. Higher cooling rates lead to an increased yield stress due to rapid cooling, which hinders atom diffusion, resulting in a more rigid and hard material structure. Conversely, slower cooling rates may result in lower yield stress, allowing for a less rigid atomic arrangement due to increased diffusion time.

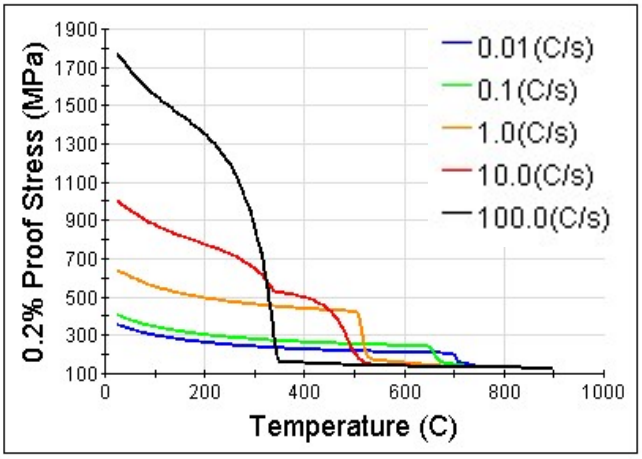

Figure 2.3: Effect of cooling rate on yield stress

Viscous flow: Viscous flow, such as elastic-viscous, viscous, and viscoelastic behaviours are challenging to differentiate from other types of deformation. The elastic-viscoplastic theory is typically applied to materials exhibiting viscous characteristics across both elastic and plastic ranges. However, due to experimental limitations, accurately quantifying the yield condition for an elastic viscoplastic material proves challenging.

Numerous authors have discussed the theory of viscoelasticity and its impact on thermal stress formation (Christensen, 1982; Hetnarski & Eslami, 2019). In the qualitative analysis of stress development during the heat treatment of metallic materials, the elevated temperatures and resulting stress levels necessitate the consideration of the viscous properties.

Transformation-induced plasticity: The origin of transformation plasticity was elucidated by proposing that during transformation, atoms positioned at the phase boundary preferentially diffuse in the direction of stress, leading to elongation in alignment with the applied stress direction (Behrens et al., 2022; Fischer et al., 2000b). During the transformation process in a metal or alloy under a non-zero stress state, the resulting strain surpasses the predicted dilatometry data obtained from stress-free specimens. This additional strain is plastic, despite the stress level being well below the overall elastic limit. The role of transformation plasticity during quenching is influenced by several factors, including properties of a material, the size and shape of the workpiece, and the cooling characteristics of the quenching medium. For example, the contribution of the TRIP increases with larger specimen sizes and higher quenching capacities of the quenchant.

2.5 Evaluation of residual thermal stresses

The process of martensite hardening frequently involves significant thermal stresses and strains. These effects can have either negative consequences, such as cracking, or positive outcomes, such as enhancing the properties of hardened steel.

The evaluation of thermal stress and strain generation during quenching relies on an understanding of the following key factors:

- Temperature distribution within the quenched material
- Phase transformation history of the material
- Temperature-dependent thermal and mechanical properties of the material

The first step in evaluating residual stress and strain involves determining the thermal history of the material during quenching. The temperature distribution within the material during quenching is influenced by the intensity of the quenching medium. Higher cooling rates result in more pronounced temperature gradients, leading to greater thermal deformations. Conversely, slower cooling produces lower thermal strains (Bardelcik et al., 2010; Dey et al., 2019). The creation of thermal stresses at each temperature depends on the developed strain and, in the presence of plastic flow, on the flow stress of the material at that temperature (Koric & Thomas, 2008).

To achieve accurate calculations of thermal stress and strain, it is crucial to track the entire history of phase transformations alongside temperature variations. These transformations involve changes in volume, which affect the coefficient of thermal expansion. In isotropic materials, both temperature change and transformations induce uniform volume changes in a material free to expand (Seif et al., 2016). Therefore, the coefficients of thermal expansion and the volume changes resulting from the transformation are represented as functions of temperature.

During the quenching process, a wide temperature range is involved, and phase transformations occur continuously as the temperature changes. These factors make it imperative to account for the temperature-dependent physical properties (thermal conductivity, specific heat, and surface heat transfer coefficient) of the material. A good understanding of the temperature-dependent mechanical properties of the material is essential to perform reliable thermal stress and strain calculations (Guo et al., 2013; Seif et al., 2016).

2.5.1 Calculation of temperature distribution

Determination of the temperature distribution in the quenched section relies on the modelling of transient heat conduction within an axisymmetric cylindrical object, represented mathematically as (Hömberg, 2004b)

$$\rho_m c_p \frac{\partial T}{\partial t} = \frac{1}{r}\frac{\partial}{\partial r}\left(k \ \frac{\partial T}{\partial r}\right) + \frac{\partial}{\partial z}\left(k\frac{\partial T}{\partial z}\right) + \ \dot{Q}. \tag{2.6}$$

This equation is subjected to the following initial and boundary conditions, $T(r,t) = T_0$ at $t = 0, 0 \leq r \ \leq \ R$ (uniform temperature), $-k\,\partial T/\partial n = h(T \ - \ T_c)$ at $t = 0, r = R$ (convection), and $\partial T/\partial n = 0$ at $t > 0, r = 0$ (symmetry).

Equation (2.6) can be solved numerically by the finite element method using the Galerkin approximation. Applying the linear law of the mixture, the heat generated per unit of time and volume during phase evolution is given by

$$\dot{Q} = \frac{\rho_m}{\Delta t}\sum_{t=1}^{5}\frac{\partial \Delta H_i}{\partial \xi_i} d\xi_i, \tag{2.7}$$

where ξ_i is the volume percentage of phase i, ΔH_i is the enthalpy of the transformation for each phase (austenite – ferrite, austenite – pearlite, austenite – bainite, and austenite - martensite) reactions.

Many heat transfer textbooks and research papers provide numerical solutions for determining temperature distributions within a material, considering variations in thermal properties with changing temperatures. (Babu & Prasanna Kumar, 2010) developed a mathematical model for surface heat flux during quenching, considering the initial soaking temperature. (Nagasaka et al., 1993) developed a mathematical model to predict thermo-elastic-plastic behaviour during water spray quenching. They applied finite element-based techniques to study the kinetics of diffusion-dependent phase transformation and martensitic transformation, coupled with transient heat flow, to predict the microstructural evolution of steel. (Gomes et al., 2019; Hömberg, 2004b) developed a mathematical model to predict the temperature profile of quenched steel, aiming to facilitate improved control over temperature distribution, and in (Bouissa et al., 2019) a new convective heat transfer coefficient during quenching was implemented.

2.5.2 Calculation of thermal stress and strain

In the theory of thermoelasticity, it is generally expected that when a body is subjected to a thermal gradient, thermal stresses develop within it. However, determining the presence of these thermal stresses requires an understanding of the relationships between the temperature gradient, boundary conditions, and thermal strain (Hetnarski & Eslami, 2019). In the case where a metal bar undergoes uniform heating or cooling and thus lacks temperature gradients, the workpiece remains free of stress. The governing equation in terms of the stresses can be written as

$$T_{,ij} + \frac{3\Lambda+2\mu_s}{\Lambda+2\mu_s} T_{,kk}\delta_{ij} = 0. \tag{2.8}$$

In expanded form, this equation read as

$$\left(\frac{1+\nu}{1-\nu}\right)\nabla^2 T + \frac{\partial^2 T}{\partial x^2} = 0, \tag{2.9}$$

$$\left(\frac{1+\nu}{1-\nu}\right)\nabla^2 T + \frac{\partial^2 T}{\partial y^2} = 0, \tag{2.10}$$

$$\left(\frac{1+\nu}{1-\nu}\right)\nabla^2 T + \frac{\partial^2 T}{\partial z^2} = 0, \tag{2.11}$$

where ν is the poison's ratio, Λ is the Lamé constants and μ_s is the shear modulus.

Combining the first three equations yields $\nabla^2 T = 0$. This signifies that the only possible temperature distribution that yields zero thermal stresses within a simply connected body region occurs when

$$\nabla^2 T = 0, \tag{2.12}$$

$$\frac{\partial^2 T}{\partial x \partial y} = \frac{\partial^2 T}{\partial y \partial z} = \frac{\partial^2 T}{\partial z \partial x} = 0. \tag{2.13}$$

However, if there is a temperature gradient, the magnitude of thermal stresses can be expressed as

$$\sigma = E\varepsilon - \alpha E \Delta T, \tag{2.14}$$

Where σ is the thermal stress, α is the linear coefficient of thermal expansion, E is the Young's modulus of elasticity, ε is the strain, and ΔT is the change in temperature.

In the presence of temperature gradient, the strain of a material is generally a function of stress and temperature, $\varepsilon = \varepsilon(\sigma, T)$

$$d\varepsilon = \left(\frac{\partial \varepsilon}{\partial \sigma}\right)_T d\sigma + \left(\frac{\partial \varepsilon}{\partial T}\right)_\sigma dT. \tag{2.15}$$

The differential of direct strain may be written in terms of Young's modulus and thermal expansion coefficient.

$$d\varepsilon = \frac{d\sigma}{E} + \alpha dT \tag{2.16}$$

If the thermal expansion coefficient α assumed constant,

$$\varepsilon = \frac{\sigma}{E} + \alpha \Delta T. \tag{2.17}$$

Determining three-dimensional thermal stresses is generally complex. However, the number of fundamental equations needed to solve them are quite sufficient. These equations include:

- 6 strain–displacement equations
- 3 stress equilibrium (Newton's second law) equations
- 6 stress–strain equations
- Thus, there are a total of 15 governing equations correlating the 15 unknown quantities:
- 6 strain components: ε_x, ε_y, ε_z, γ_{xy}, γ_{yz}, and γ_{xz}
- 3 displacement components: $u, v,$ and w
- 6 stress components: σ_x, σ_y, σ_z, τ_{xy}, τ_{yz}, and τ_{xz}

Next section is discussed some of the equations used to quantify these components in a more comprehensive way.

To determine the thermal stress distribution within a material, the initial step is to calculate the temperature distribution. The governing equation for the rate of conduction heat transfer is the Fourier rate equation.

$$\dot{Q} = -k_t A \frac{\partial T}{\partial x}, \tag{2.18}$$

where k_t represents the thermal conductivity of the material, A denotes the area through which heat is conducted, and $\partial T / \partial x$ is the temperature gradient in the direction along which heat is conducted.

The conduction rate

$$\dot{Q}_{x,in} = -k_t (dy\, dz) \frac{\partial T}{\partial x}. \tag{2.19}$$

The rate of conduction heat transfer from the element in the x-direction can be written as follows:

$$\dot{Q}_{x,out} = \dot{Q}_{x,in} + \frac{\partial \dot{Q}_x}{\partial x} dx = \dot{Q}_{x,in} - \frac{\partial}{\partial x}\left(k_t \frac{\partial T}{\partial x}\right) d \quad dy\, dz \tag{2.20}$$

The net heat conduction rate

$$\dot{Q}_{x,net} = \dot{Q}_{x,in} - \dot{Q}_{x,out} = +\frac{\partial}{\partial x}\left(k_t \frac{\partial T}{\partial x}\right) dx\, dy\, dz \tag{2.21}$$

The temperature and strain equations can be coupled. The rate of change of energy stored in the element involves both thermal and strain energy (Reza Eslami et al., 2013, W. Zhang et al., 2014) written as

$$\frac{\partial U}{\partial t} = \rho c_\varepsilon \frac{\partial T}{\partial t} dx\, dy\, dz + \left(\sigma_x \frac{\partial \varepsilon_x}{\partial t} + \sigma_y \frac{\partial \varepsilon_y}{\partial t} + \sigma_z \frac{\partial \varepsilon_z}{\partial t}\right) dx\, dy\, dz + \beta_t T B \left(\frac{\partial \varepsilon_x}{\partial t} + \frac{\partial \varepsilon_y}{\partial t} + \frac{\partial \varepsilon_z}{\partial t}\right) dx\, dy\, dz, \tag{2.22}$$

where the term c_ε is the specific heat at constant strain, and the coefficient in the last term, $\beta_t B = \alpha E/(1-2\nu)$.

2.6 Characteristics of steel materials in induction hardening

2.6.1 Phase transformation in steel materials

Phase transformation refers to the atomic rearrangement of a material triggered by temperature changes. During the heating process, initially, the steel expands in direct proportion to the increase in temperature. However, when it reaches the critical point Ac_1, expansion stops. Subsequently, upon reaching the critical temperature of Ac_3, indicating complete austenitization during continuous heating, the steel resumes expansion.

There are two main types of transformation diagram used to determine the optimal steel and processing route to achieve desired properties: time-temperature transformation (TTT) and continuous cooling transformation (CCT) diagram. CCT diagram is generally preferred for engineering applications because they allow components to be cooled directly from the processing temperature (i.e. air cooling, furnace cooling, quenching, etc.), which is more cost-effective than transferring to a separate furnace for isothermal treatment. It measures the extent of transformation as the temperature decreases continuously. For instance, a sample is heated to the austenitizing temperature and then cooled at a constant rate, and the resulting transformation is observed, typically using methods such as dilatometry.

The TTT diagrams measure the transformation rate at a constant temperature. For example, a sample is austenitised and cooled to a lower temperature and held at that temperature while the transformation rate (i.e., using dilatometry).

The CCT curves offer information on the temperatures associated with each phase transformation, the amount of transformation product achieved for a specific cooling rate over time, and the cooling rate required to produce martensite. The critical cooling rate is determined by the time needed to prevent pearlite formation in the quenched steel. Typically, a quenchant must deliver a cooling rate equal to or faster than that indicated by the "nose" of the pearlite transformation curve to optimise martensite formation (Totten et al., 2002). CCT diagrams can only be interpreted along curves representing different cooling rates. This rapid cooling replaces diffusion-dependent transformation with a shear-type (diffusion-less) transformation, resulting in the formation of martensite from austenite (Figure 5.3).

2.6.2 Cooling medium

During quenching when the steel is rapidly cooled from the austenitization temperature, the carbon remains locked within the austenite microstructure, preventing its diffusion as it transforms into martensite, characterised by a body-centred tetragonal (BCT) (Gomes et al., 2019; Grong & Shercliff, 2002). The primary aim of quenching is to achieve a cooling rate sufficient for martensite formation, which contributes to the elevated strength and hardness of quenched steel. However, when steel undergoes slow cooling from the austenitization temperature, the face centred cubic (FCC) austenite transitions into body centred cubic (BCC) ferrite, causing the rejection of carbon atoms. This results in the formation of pearlite through a nucleation and growth process, where alternating layers of ferrite and cementite emerge (Poyraz & Ögel, 2020; M.-X. Zhang & Kelly, 2009).

Martensite formation begins at the martensite start temperature (M_s) and completes as the steel is cooled below the martensite finish temperature (M_f). To achieve the necessary cooling rates, many steels are quenched in water or oil. Water quenching offers the fastest cooling rates but can lead to high residual stresses, warpage, and distortion.

Temperature gradients, influenced by the choice of quenchant, cooling rate, and quenching methods, play a crucial role in determining the outcomes of hardening processes. The cooling stage significantly impacts the depth to which the temperature is induced. The cooling rate of a specific

section of a steel bar from the austenitizing temperature depends on two factors: (1) the temperature to which the quenching medium cools the surface of the workpiece, and (2) the heat flow rate within the workpiece. Due to the heat conduction properties of steel, the central region of the workpiece cools much more slowly than the surface. The temperature profile illustrating the phenomena on the surface and at the core is given in Figure 2.4. Consequently, the surface and the core develop different types of stresses at different times during quenching, as shown in Figure 2.5. This indicates the benefits obtained from quenching in terms of improving mechanical properties.

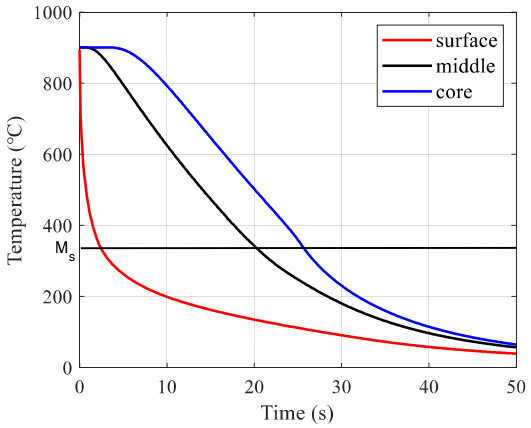

Figure 2.4: Temperature profile at the surface and the core

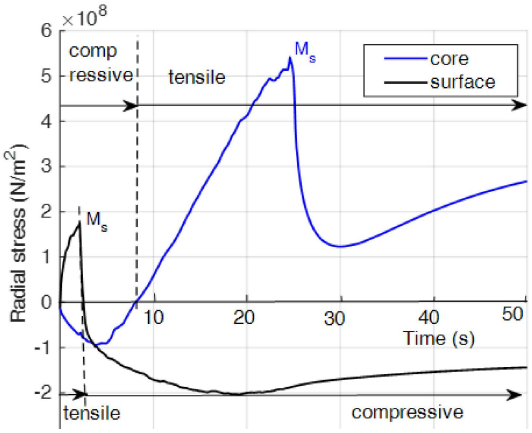

Figure 2.5: Stress development on the surface and core in response to temperature gradient

The rise in compressive stress on the surface was accentuated upon reaching the M_s temperature. A maximum compressive stress of 202 MPa was observed as the surface temperature

decreased to 140 °C. As the transformation front progressed from the surface towards the centre, a release of the surface compressive stress occurred. Conversion of austenite to martensite at the centre prevented further plastic deformation. At this point, the cooling rate at the centre surpassed that of the surface, resulting in a notable increase in tensile stress at the centre.

2.7 Temperature measurement during induction heating

2.7.1 Thermocouple

A thermocouple is an electrical device consisting of two dissimilar conductors forming an electrical junction. It produces a temperature-dependent voltage as a result of the Seebeck effect, which can be interpreted to measure temperature. The Seebeck effect specifically describes the generation of an electromotive force within an electrically conductive material due to a temperature difference between two points. In situations where there is no internal current flow (open circuit), the change in voltage (ΔV) is directly proportional to the temperature gradient.

$$\nabla \mathrm{V} = -S(T)\nabla T \tag{2.23}$$

Here $S(T)$ is the Seebeck coefficient (temperature-dependent material properties).

2.7.2 Infrared thermography

Infrared thermography employs an infrared imaging and measurement camera to detect invisible infrared energy emitted by an object (Gaussorgues, 1994). This energy, known as thermal or infrared energy, falls outside the visible spectrum and cannot be perceived by the human eye because of its longer wavelength. Instead, it is recognised as heat. The intensity of infrared radiation increases with the temperature of the object, and the camera allows us to visualise this energy. As the temperature increases, it emits more energy, resulting in a shorter wavelength.
Characteristics of infrared thermography include:

- Capture the distribution of temperature across a surface and present it visually.
- Enables temperature measurement from a distance, without physical contact with the object
- Temperature measurements can be obtained in real time.

Experimental methods that measure load-induced information associated with stress changes, such as strain gauges, thermoelastic stress analysis (TSA), and photoelastic stress analysis

(PSA), need additional experimentation or numerical analysis to isolate individual stress components. TSA, often employed in the analysis of loaded structures, utilises an infrared camera to capture thermal data correlated with mechanical stress changes under adiabatic conditions (Alshaya, 2023; Dulieu Barton & Stanley, 1999; Patterson & Rowlands, 2008). Although PSA and strain gauges offer load-induced data like TSA, the former need time-consuming installation and nonlinear numerical analysis to derive individual stresses and necessitate linear analysis (Alshaya, 2023; S. J. Lin et al., 2015).

2.7.3 Numerical methods

Recently, simulations of quenching and other heat treatment processes have increasingly relied on numerical methods such as the finite difference method (FDM), the finite volume method (FVM), and especially the FEM (Burkhart et al., 2013, Srivastava et al., 2022). Designers of induction heating systems must use specialised software tools capable of effectively simulating the process (Kianezhad et al., 2015). An ideal design for a modern induction heating system should view the features of induction heating not only as standalone physical processes, but as an integrated system comprising the inductor, load-matching station, and power supply (i.e. solid-state inverter).

FEM is a general numerical method for solving partial differential equations in two or three space variables (i.e., boundary value problems). To solve a problem, a large system is divided into smaller, simpler pieces called finite elements. The numerical domain for the solution has a finite number of points, which is obtained through a particular space discretisation in the space dimensions.

2.7.3.1 Finite element discretisation

Initially, the structure is discretised into numerous subregions, with the displacement field expressed in nodal values for each subregion. Subsequently, the total potential energy, which encompasses both strain energy and nodal force potential, is minimised concerning the nodal values, establishing the equilibrium relationship (Zervos et al., 2009).

$$\{F_e\} = [\mathrm{K}]\{u\}, \tag{2.24}$$

where $\{u\}$ is the vector of nodal displacements (also $\{u\}$ refers to the nodal degrees of freedom), $\{F_e\}$ is the vector of element nodal forces, and [K] is called the element stiffness matrix.

When a continuous medium is discretised into a collection of piecewise simple regions, the issue of assemblage arises, encompassing two key aspects:

1. Ensuring compatibility among the elements by sharing nodes between neighbouring elements.
2. Achieving equilibrium among the assembled elements, typically by balancing forces or summing strain energies.

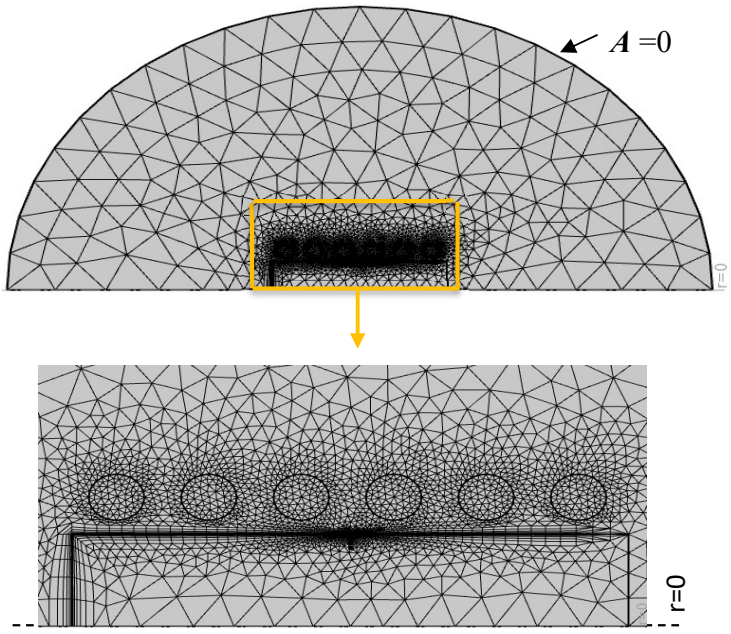

Figure 2.6: Finite element mesh

The accuracy of numerical model results depends on several factors, including mesh quality (coarse or fine), types of mesh (i.e., hexahedral, tetrahedral, or triangular), and the geometry of the workpiece (Figure 2.6). When assessing the quality of a finite element mesh, two primary concerns emerge. Firstly, the shape of the elements used for geometry discretization is crucial. Secondly, the mesh, determined by the number of elements it comprises, is a significant consideration (Burkhart et al., 2013).

The reliability of a model to predict real-world phenomena depends on a rigorous examination of its outcomes compared to experimental data (Oberkampf & Trucano, 2002; Rebba et al., 2006), typically through numerical validation. The criteria for evaluating mesh quality primarily focus on the geometric attributes of elements, with the aim of ensuring symmetrical

shapes (aspect ratios), ideal internal angles, and positive volumes (element Jacobians) (Knupp, 2001).

2.7.3.2 Convergence of the solutions

To be effective, the solution of the finite element method must converge towards exact solutions while respecting geometric boundary conditions and interelement compatibility. To ensure convergence, three additional criteria must be satisfied.

1. The element must accurately model a consistent state of strain and stress as the element size approaches infinitesimally small limits.
2. A supplementary requirement is that the element should be capable of accommodating rigid-body displacements without inducing strains. This mirrors the constant strain condition, where $\varepsilon_{ij} = 0$ and serves as an extreme scenario to ensure uniformity of strain.
3. Lastly, the assumed displacement functions should be comprehensive enough to meet the orders required by the initial criterion.

When these criteria are met, a minimum level of strain energy is guaranteed, ensuring monotonic convergence.

2.8 Strain-based displacement

In general, when a point is displaced by a small distance from the reference point, the resulting change may vary slightly. Suppose the element in Cartesian coordinates. Let us denote the displacement components of a specific point (x, y, z) as u (x-displacement), v (y-displacement), and w (z-displacement).

Extensional strain refers to the change in length per original length unit. The extensional strain along the x, y, and z-direction can be expressed as follows (Barron & Barron, 2012,p.199).

$$\varepsilon_x = \frac{\left(u+\frac{\partial u}{\partial x}dx\right)-u}{dx} = \frac{\partial u}{\partial x} \tag{2.25}$$

$$\varepsilon_y = \frac{\left(v+\frac{\partial v}{\partial y}dy\right)-v}{dy} = \frac{\partial v}{\partial y} \tag{2.26}$$

$$\varepsilon_z = \frac{\left(w+\frac{\partial w}{\partial z}dz\right)-w}{dz} = \frac{\partial w}{\partial z} \tag{2.27}$$

Shear strains or distortion strains are defined as the change in the angle between two intersecting planes of the element. Due to the small magnitude of these strains, the tangent of the angle is practically equivalent to the angle itself. The shearing strain between the edge of the element in the *x*-direction and the side of the element in the *y*-direction can be determined in the following manner.

$$\gamma_{xy} = \frac{\left(u+\frac{\partial u}{\partial y}dy\right)-u}{dy} + \frac{\left(v+\frac{\partial v}{\partial x}dx\right)-v}{dx} = \frac{\partial u}{\partial y} + \frac{\partial v}{\partial x} \tag{2.28}$$

$$\gamma_{xz} = \frac{\left(u+\frac{\partial u}{\partial z}dz\right)-u}{dz} + \frac{\left(w+\frac{\partial w}{\partial x}dx\right)-w}{dx} = \frac{\partial u}{\partial z} + \frac{\partial w}{\partial x} \tag{2.29}$$

$$\gamma_{yz} = \frac{\left(v+\frac{\partial v}{\partial z}dz\right)-v}{dz} + \frac{\left(w+\frac{\partial w}{\partial y}dy\right)-w}{dy} = \frac{\partial v}{\partial z} + \frac{\partial w}{\partial y} \tag{2.30}$$

It is obvious from the definition of the shear strains, that $\gamma_{xy} = \gamma_{yx}$, $\gamma_{xz} = \gamma_{zx}$, and $\gamma_{yz} = \gamma_{zy}$. Thus, there are only three different shear strains. Such types of strains are sometimes called engineering strains.

2.9 Stress-equilibrium relations (force balances)

The stresses and forces exerted on a differential element are typically specified within cartesian coordinates, and they fall into two primary categories: (a) Surface forces, originating from direct or normal stresses in the x, y, and z directions (σ_x, σ_y, and σ_z) as well as shear stresses (ε_{xy}, ε_{yz}, and ε_{xz}), and (b) Body forces, representing forces per unit volume ($X, Y,$ and Z), which may arise from gravitational forces (such as the weight of the material), magnetic forces, inertial forces.

Applying the Newton's 2nd law of motion, $\sum F = ma$, in the x-direction, can be written as

$$\frac{\partial \sigma_x}{\partial x}dx\,(dy\,dz) + \frac{\partial \sigma_y}{\partial y}dy\,(dx\,dz) + \frac{\partial \sigma_z}{\partial z}dz\,(dx\,dy) + X\,(dx\,dy\,dz) = \rho(dx\,dy\,dz)\frac{\partial^2 u}{\partial t^2} \tag{2.31}$$

Applying the same law for x, y and z direction respectively the stress relation can be written (Barron & Barron, 2012, p.205) as

$$\frac{\partial \sigma_x}{\partial x} + \frac{\partial \tau_{xy}}{\partial y} + \frac{\partial \tau_{xz}}{\partial z} + X = \rho_m \frac{\partial^2 u}{\partial t^2}, \tag{2.32}$$

$$\frac{\partial \tau_{yx}}{\partial x} + \frac{\partial \sigma_y}{\partial y} + \frac{\partial \tau_{yz}}{\partial z} + Y = \rho_m \frac{\partial^2 v}{\partial t^2}, \tag{2.33}$$

$$\frac{\partial \tau_{zx}}{\partial x} + \frac{\partial \tau_{zy}}{\partial y} + \frac{\partial \sigma_z}{\partial z} + Z = \rho_m \frac{\partial^2 w}{\partial t^2}. \tag{2.34}$$

Here ρ_m represents mass density. For steady-state or static conditions, the right side of equations 2.32 to 2.34 are zero.

2.10 Stress–strain relations (generalised Hooke's law)

The mechanical strain in the *x*-direction caused by a stress σ_x is given by σ_x/E. Similarly, for the y and z direction, the strains caused by σ_y and σ_z respectively are given by $-\nu\,\sigma_y/E$ and $-\nu\,\sigma_z/E$, where ν represents the poison's ratio effect. Again, if the temperature T changes from the stress-free temperature T_0 by $\Delta T = (T - T_0)$, a thermal strain, $\alpha\Delta T$, will result. Combining all four components, it can be written as the stress-strain relationship in the elastic range for the x, y, and z directions (Hetnarski & Eslami, 2019, p.24).

$$\varepsilon_x = \frac{1}{E}\left[\sigma_x - \nu(\sigma_y + \sigma_z) + \alpha\Delta T\right] \tag{2.35}$$

$$\varepsilon_y = \frac{1}{E}\left[\sigma_y - \nu(\sigma_x + \sigma_z) + \alpha\Delta T\right] \tag{2.36}$$

$$\varepsilon_z = \frac{1}{E}\left[\sigma_z - \nu(\sigma_x + \sigma_y) + \alpha\Delta T\right] \tag{2.37}$$

In a homogeneous isotropic material, shear stresses (τ_{xy} , for instance), there is no generation of strains in the third coordinate direction (e.g., the z-direction). Consequently, the effect of the Poisson ratio is not evident for shear stresses in such materials. Similarly, temperature changes typically lead to expansions or contractions rather than distortion strains. Shear strains directly correlate with shear stresses (Barron & Barron, 2012,p.207).

$$\gamma_{xy} = \frac{\tau_{xy}}{G} = \frac{2(1+\nu)\tau_{xy}}{E}, \tag{2.38}$$

$$\gamma_{xz} = \frac{\tau_{xz}}{G} = \frac{2(1+\nu)\tau_{xz}}{E}, \tag{2.39}$$

$$\gamma_{yz} = \frac{\tau_{yz}}{G} = \frac{2(1+\nu)\tau_{yz}}{E}, \tag{2.40}$$

where the shear modulus, $G = E/2(1+\nu)$ and τ is the shear stress, respectively. The six stress-strain relations may be written in compact form using the index notation and the mathematical strain terms.

$$\varepsilon_{ij} = \frac{1}{E}\left[(1+\nu)\sigma_{ij} - \nu(\sigma_{11} + \sigma_{22} + \sigma_{33})\delta_{ij}\right] + \alpha\Delta T\delta_{ij}, \qquad \text{(i, j = 1, 2, 3)} \tag{2.41}$$

where the quantity δ_{ij} is the Kroneker delta and is defined by

$$\delta_{ij} = \begin{cases} 1 \ for \ i = j \\ 0 \ for \ i \neq j. \end{cases} \quad (2.42)$$

The quantity $S_m = (\sigma_{11} + \sigma_{22} + \sigma_{33})/3 = (\sigma_x + \sigma_y + \sigma_z)/3$ is called the mean applied stress.

Let us define the quantity volumetric dilatation, $e_v = (\varepsilon_{11} + \varepsilon_{22} + \varepsilon_{33}) = (\varepsilon_x + \varepsilon_y + \varepsilon_z)$

Adding Equations 2.38 to 2.40, can be written as

$$\varepsilon_x + \varepsilon_y + \varepsilon_z = \frac{1-2\nu}{E}(\sigma_x + \sigma_y + \sigma_z) + 3\alpha\Delta T. \quad (2.43)$$

Mean stress and volumetric dilatation are related as follows.

$$e_v = \frac{S_m}{B} + \beta_t \Delta T, \quad (2.44)$$

where the volumetric thermal expansion coefficient, $\beta_t = 3\alpha$, and the volume modulus of elasticity, $B = E/3(1 - 2\nu)$.

2.11 Mechanical response to thermal stress

TRIP has a dual impact on the mechanical response of the material during quenching, influencing both the stress evolution and residual stress levels. Stress evolution during quenching at any given point can be divided into loading, unloading, and reverse loading phases. Initially, dilatation caused by phase transformations induces unloading, followed by reverse loading. During reverse loading, stresses typically reach levels capable of inducing plastic deformation. When the material is in the elastic zone, TRIP serves as an extra strain, promoting stress relaxation. In the plastic zone, if the TRIP strain adequately accommodates deformation, no additional plastic strain is needed, resulting in stress relaxation. However, when the TRIP strain is insufficient in the plastic zone, stress relaxation does not occur because additional plastic strain is required for further deformation (Behrens et al., 2022; Soleimani et al., 2020).

The typical residual stress distribution in a quench-hardened workpiece with axisymmetric geometry exhibits tensile stresses on the surface and compressive stresses in the core. These patterns are closely related to the irreversible strain history, which is influenced by various factors including material properties and the temperature profile during cooling (cooling medium, material composition and geometric features). The irreversible nature of TRIP generally intensifies the residual stress state.

The role of TRIP hinges on the balance between irreversible strains from classical plasticity and transformation plasticity. The impact of a TRIP is notably significant when the primary source of irreversible strains is transformation plasticity, without reliance on classical plasticity. This phenomenon is particularly evident in surface treatments such as induction, laser hardening, and carburising, where transformation plasticity alone is capable of effectively managing deformation (Fischer et al., 2000b; Inan & Tauchert, 2014).

The evolution of TRIP has commonly relied on a phenomenological approach. When exposed to uniaxial stress, the transformation plasticity strain is typically expressed in a general form as

$$\varepsilon^{tr} = K \cdot \sigma \cdot \phi(\xi), \tag{2.45}$$

where σ is the applied stress, K is the transformation plasticity coefficient, $\phi(\xi)$ is the progress of transformation plasticity. The value of K and $\phi(\xi)$ is determined either experimentally or by calculation.

When dealing with a triaxial stress state, it is commonly assumed that similar relationships apply to both classical plasticity and TRIP. For instance, the transformation plasticity strain rate is typically presumed to be proportional to the stress deviator due to the von Mises associated flow rule (Gür & Pan, 2009). However, unlike classical plasticity, TRIP does not adhere to a specific yield criterion and can occur even under low stresses.

2.12 Mitigation strategies and control technique

2.12.1 Residual stresses distortion control

The quality of hardened parts is significantly influenced by factors such as the cooling rate, fixture design, and cooling duration, leading to distortion, residual stresses, and potential cracking. In the induction hardening of the steel workpiece, both the thermal gradient and the phase transformation act simultaneously to influence the evolution of internal stresses and distortion.

Induction heating processes may involve two steps: a single step with dual frequencies or a two-step with distinct frequencies for each step. Simultaneous dual frequency (SDF) induction heating, where both medium and high frequencies are applied simultaneously to the part, results in a more uniform temperature distribution, particularly beneficial for curved surfaces such as gear

tooth profiles (Li & Ferguson, 2012). In the case of dual frequencies (DF), automatically shifts from the first frequency to the second as specified in the algorithm.

Another common method for hardening gear components is the sequential application of two induction frequencies. Typically, a lower frequency is initially used to heat the gear root, followed by a higher frequency for the gear tip. Introducing a time delay between the two frequencies allows for more flexible control over temperature distribution within the component.

In gearwheel hardening, the temperature profile has three zones: the tooth tip, which is heated above the Ac_1 temperature (austenitizing temperature); the transition zone, which is below the Ac_1 temperature; and the unaffected zone, which comprises the larger part of the gearwheel.

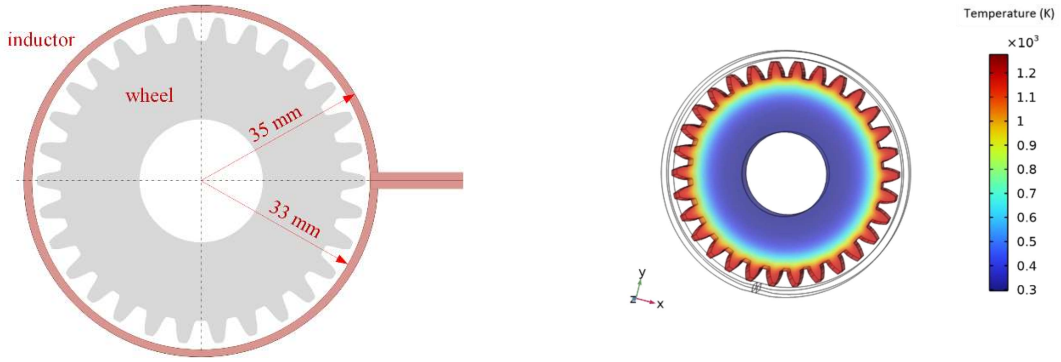

Figure 2.7: Gear tooth hardening

Figure 2.7 shows the gearwheel heated prior to quenching to obtain the required mechanical properties. The tooth tip is subjected to cyclic loads from gear meshing, which is why it needs high hardness and high strength.

2.12.2 Optimisation of heating parameters

Improved efficiency in induction heating offers benefits such as precise temperature control, safety, environmental friendliness, and rapid heating. When optimising the entire cycle of induction heating, the thermal process must be carefully addressed. This encompasses the heating process, the cooling, and soaking stages during billet transportation. To achieve the desired temperature in the workpiece prior to hot working operations, temperature distribution after the transfer stage as a function controlled by the output is considered. Consequently, the controlled heating cycle is characterised by a set of heat transfer equations that encompass both the heating and cooling (transfer) stages.

The billet temperature $T_h\ (l,t)$ during the heating process can be described by:

$$\frac{\partial T_h\ (l,t)}{\partial t} = \frac{\partial^2 T_h(l,t)}{\partial l^2} + \frac{\Gamma}{l}\frac{\partial T_h(l,t)}{\partial l} + w(\xi,l)u(t), \tag{2.46}$$

$$0 < l < 1;\ 0 < t < t_0.$$

With boundary conditions of the third kind,

$$\frac{\partial T_h\ (l,t)}{\partial l} = Bi_h\ (T_a - T_h)(1,t), \tag{2.47}$$

$$\frac{\partial T_h\ (0,t)}{\partial l} = 0, \tag{2.48}$$

$$T_h(l,0) = T_0 = T_a = \text{constant} \tag{2.49}$$

where t_0 is the total time of heating, Bi_h is the Biot number correspond to heat losses from the surface of the workpiece during the whole heating process, $u(t)$ a control input function, $w(\xi,l)$ is the energy loss from the source.

In the subsequent transfer stage, the temperature distribution $T_\theta\ (l,t)$ follows the same equation (Equation 2.46) but does not include any heat sources.

$$\frac{\partial T_\theta\ (l,t)}{\partial t} = \frac{\partial^2 T_\theta(l,t)}{\partial l^2} + \frac{\Gamma}{l}\frac{\partial T_\theta(l,t)}{\partial l} + 0 < l < 1, \tag{2.50}$$

$$t_0 < t < t_0 + \Delta t.$$

With boundary conditions,

$$\frac{\partial T_\theta\ (l,t)}{\partial l} = Bi_\theta\ (T_a - T_\theta)(1,t), \tag{2.51}$$

$$\frac{\partial T_\theta\ (0,t)}{\partial l} = 0, \tag{2.52}$$

$$T_\theta(l,t_0) \equiv T_h(l,t_0). \tag{2.53}$$

During the transfer stage, it is cooled intensively, $Bi_\theta > Bi_h$.

Mathematical proof demonstrates that, concerning the models under consideration, the time-optimal control strategy involves alternating between stages of heating at maximum power $u \equiv U_{max}$ (heat ON) and subsequent soaking/cooling cycles with power $u = 0$ (heat OFF). Figure 2.8 illustrates the advantages of the soaking stage in induction heating to achieve uniform temperature over the required depth. The computation duration was 210 s with a coil current 260 A and current frequency 7.5 kHz. Due to the temperature difference between the surface and the core, heat transfer continues without being affected by the power-off stage. Typically, successful hardening

involves attaining the necessary microstructure, hardness, strength, or toughness while minimizing residual stresses, distortions, and the risk of cracking.

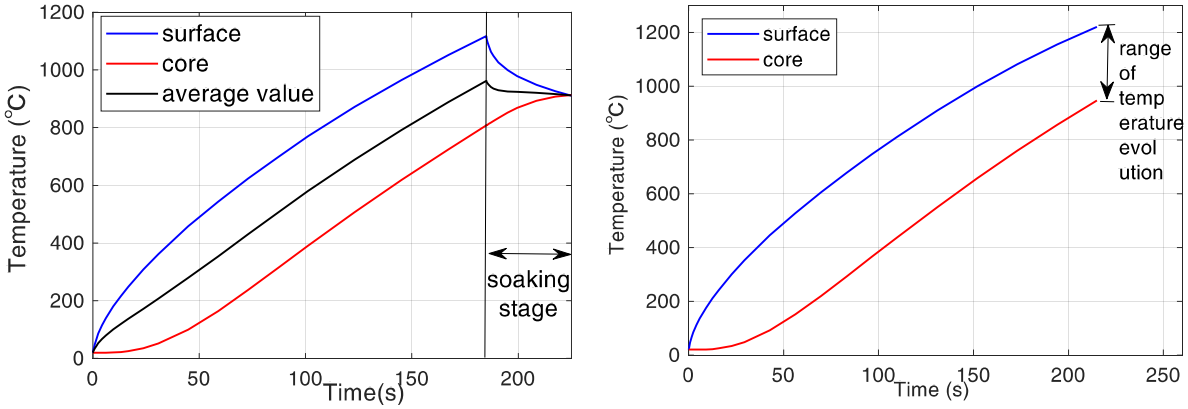

Figure 2.8: Single frequencies with soaking stage (left), and without soaking stage (right)

Induction hardening is commonly used to increase the hardness and durability of various types of metal components. Induction hardening is commonly used in the manufacturing of gears, shafts, and other components that are subject to high levels of stress and wear. Most applications of induction surface hardening require high-power densities and short heating cycles to restrict heating to the surface area. The main metallurgical advantages of surface hardening with induction include increased wear resistance and improved fatigue strength.

Induction contour hardening of gear wheels is a highly effective heat treatment technology, particularly recommended for advanced applications in the machinery, automotive, and aerospace industries. Compared to traditional, energy-intensive heat treatments such as carburising, nitriding, and other methods (nitrocarburising and carbonitriding), it offers significant advantages, including high overall efficiency, short processing times, and lower energy consumption. However, modelling this process is relatively complex. The numerical model must incorporate both multiphysics and non-linear formulations. It also considers that critical temperatures, and thus the hardening temperature, depend on the speed of the induction heating. Although hardening depends on several factors such as steel grade, part size, part shape, and desired case depth, implementing the proper method helps achieve the desired properties. The contour induction heating model shown in Figure 2.9 uses a heat flux of 250 kW for 5 s in a frequency transient study.

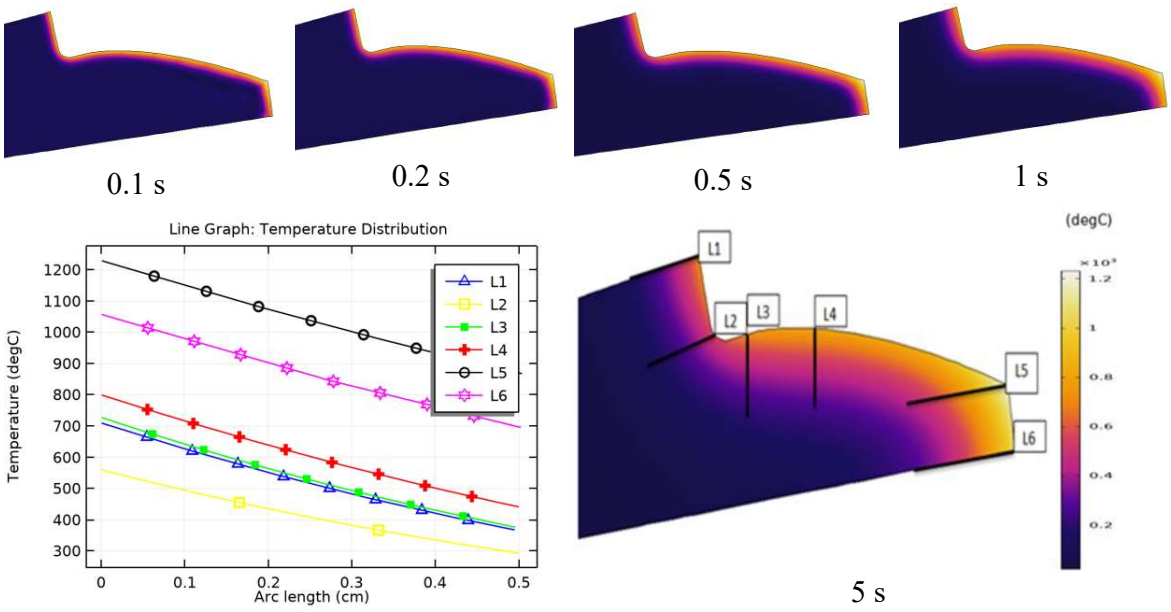

Figure 2.9: Surface heating

Figure 2.9 shows the temperature profile prior to surface hardening. The induction hardening process does not change the surface chemical composition. However, heating to the austenite temperature followed by rapid cooling prevents carbon segregation and results in martensite transformation.

Several factors influence the induction hardening process (Totten et al., 2002, p220):

- The power, frequency, and configuration of the induction coil affect the heating rate, depth, and uniformity of the metal components.
- The composition, microstructure, and shape of the metal parts affect their electrical conductivity, magnetic permeability, transformation temperature, and distortion behaviour.
- The quenching medium, the temperature and the cooling rate, the hardness gradient and residual stress distribution within the metal parts.
- Preheating temperature, speed of movement, and ambient temperature of the metal components play a role in determining the thermal gradient, phase transformation, and mechanical properties of the metal parts.

Chapter 3

Numerical model for induction heating

3.1. Introduction

Numerical modelling serves as a fundamental tool for advancing our understanding of the phenomena that occur within the workpiece during induction heating and subsequent cooling (quenching), with the aim of obtaining predictable target mechanical properties (Favennec et al., 2003; Rhein et al., 2015; Zhe & Sanqiang, 2013). Modern induction heating technology is geared towards effectively managing heat generation within the workpiece to attain the desired temperature in specific regions and within defined timeframes. Precision control of temperature distribution is paramount in induction heating (Fisk et al., 2018; Khalifa et al., 2019), offering advantages in terms of economy, environmental impact, and production efficiency. Manipulation of input parameters (coil current, frequency, heating duration, and inductor shape) facilitates the creation of a desired temperature profile while mitigating the risk of liquid formation on the surface and edges (Bodart et al., 2001; Masserey et al., 2004; Ono et al., 2002). However, while significant efforts have been directed towards mathematical modelling, practical implementation on the workpiece surface remains a challenge.

In the induction heating process, the control function typically involves selecting the operating frequency and the input power. In addition, factors such as coil design, workpiece geometry, and air gap determination must be considered to achieve the desired final temperature. Numerical modelling is used to gain insight into the process and accommodate the temperature-dependent nature of the material properties. According to Fourier's law of heat conduction, temperature gradients always move towards regions of lower temperature. On the other hand, a notable characteristic of AC has an effect on the skin, which primarily affects the surface. Integrating these two phenomena offers a solution for induction heating, potentially governing temperature distribution and heat transfer from the surface to the interior of the material.

In metals possessing high thermal conductivity, maintaining uniformity between surface and core temperatures is generally more feasible (e.g., copper, aluminium, silver). On the contrary, metals with low thermal conductivity (such as stainless steel, titanium, and carbon steel) require additional attention to ensure the desired temperature consistency. Numerical modelling of these

intricate processes is crucial, as it enables visualisation of the entire process within the workpiece. The involvement of AC power source adds complexity to the process.

To reduce such complexity, two main strategies were proposed. The first involves influencing current penetration depth by controlling electromagnetic frequencies, either through synchronous or asynchronous dual-frequency methods. Properly solving a set of Maxwell equations allows for the management of skin depth. The second strategy involves controlling the heat distribution through a combined solution of Maxwell's equations and Fourier's law of conduction. Both scenarios are discussed in detail in Section 3.3.

The induced current density decreases exponentially from the surface to the core during induction heating, a phenomenon known as the depth of the skin. The extent of the skin effect depends on the frequency of current, the size of the workpiece, and the properties of the material.

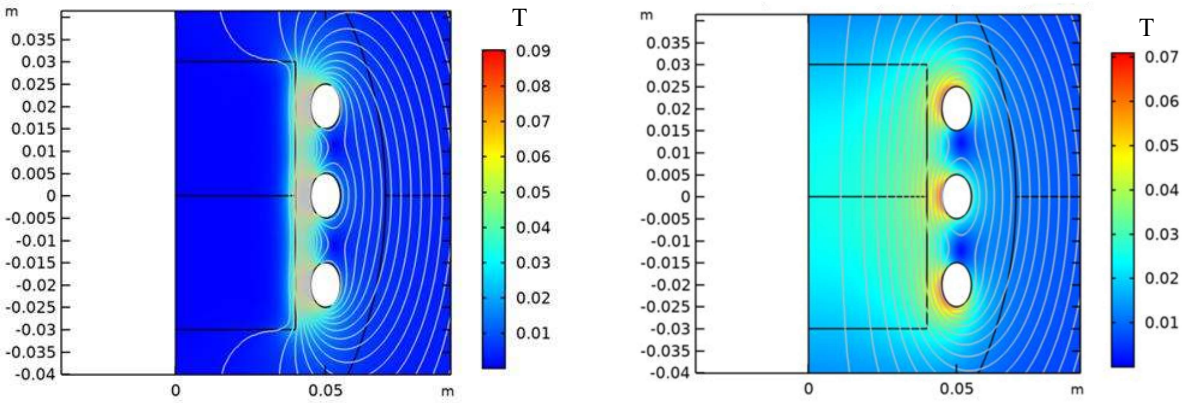

Figure 3.1: Distribution of magnetic flux density

During medium-frequency induction heating, the penetration depth is greater and the current travels a longer distance toward the core shown in Figure 3.1(right). On the contrary, during high-frequency IH, the current density is confined to the surface and may only persist for a short duration as in Figure 3.1(left). Combining the two phenomena, the dual frequency approach is less expensive to implement, with medium frequency followed by high frequency (Sönmez et al., 2022) to achieve the desired penetration depth.

3.2 Physical model

The primary properties of the material responsible for regulating the temperature distribution and heat energy flow within solids include electrical conductivity, thermal conductivity, and magnetic permeability. For pure metals and metallic materials, the Weidermann-Franz law governs the

relationship between thermal conductivity and electrical conductivity, which also varies with temperature. The law states that, for metals, the ratio of thermal conductivity to the product of electrical conductivity and temperature should remain constant (Callister & Rethwisch, 2015).

$$L = \frac{k}{\gamma T}, \tag{3.1}$$

where γ is the electrical conductivity, k is the thermal conductivity, T is the absolute temperature and L is a constant.

However, some alloys deviate from this widely accepted principle (Rudnev et al., 2003). As the temperature rises, metals expand and undergo changes in their mechanical properties, experiencing a reduction in stiffness and strength while altering their atomic structure. The increase in heat energy disrupts the alignment of atoms, preventing the production of a magnetic field because of high vibration. Consequently, the magnetic permeability of metals is high at low temperatures but diminishes as they approach their Curie temperatures, eventually reaching the permeability level of air.

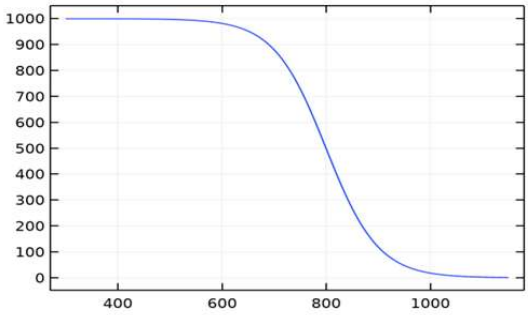

Figure 3.2: Relative permeability as a function of temperature

Permeability is high just below the Curie point. However, once the temperature exceeds the Curie point, the permeability abruptly vanishes, and the material is no longer magnetic. As shown in Figure 3.2 magnetic permeability experiences a sharp decrease within the range of 700–900 K, eventually reaching unity at around 1100 K. According to (Amitava et al., 2004), the magnetic permeability is elevated before the Curie point, but a broad transition occurs within the range of 753 to 903 K.

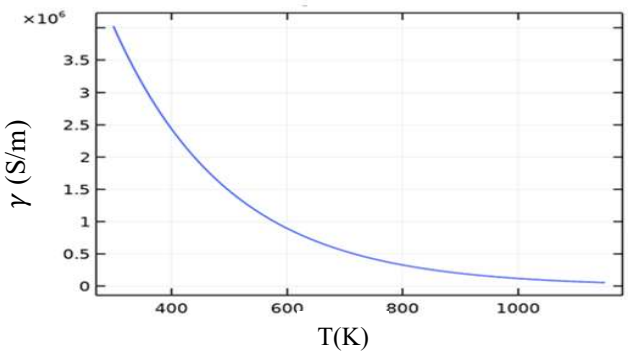

Figure 3.3: Electrical conductivity as a function of temperature

A linear approximation relies not on the electric field (or the magnitude of electric current), but rather on temperature. Reference (Fakir et al., 2018) conducted a similar study on AISI 4340 steel, using the finite difference method to investigate the properties of the material. Their experimental work affirmed that thermal conductivity decreases with increasing temperature. Typically, at room temperature or above, the electrical conductivity of a standard conductor is inversely proportional to temperature (Figure 3.3). The electrical conductivity value is consistently positive.

The use of numerical modelling in process temperature regulation contributes significantly to the design and implementation of industrial heating applications. This enhances process visualisation and facilitates the development of effective control mechanisms. In heating applications, one approach involves regulating the heat flow within the solid by managing the input (heat source). The other approach is to control the heat generation within the workpiece using a fuzzy logic control mechanism. Therefore, the use of numerical modelling enables the prediction of how various interconnected and nonlinear factors can influence the transitional and final thermal conditions of the heated component (Sönmez et al., 2022). Furthermore, it helps to forecast necessary improvements to enhance process efficiency and formulate the most suitable process strategies.

3.3 Basic of the induction heating process

Process control involves monitoring and adjusting a process to achieve the desired outcome, commonly used in industries to maintain and improve quality. Using numerical and mathematical models, it provides detailed event algorithms and diagrams within a workflow, offering enhanced visualisation and insight into how the process functions.

The process IH is generally complex and involves the simultaneous integration of three physical phenomena: electromagnetic field, the thermal field (heat transfer), and solid mechanics factors (stress/strain). Temperature changes instantly impact the physical and electromagnetic properties of the material. Consequently, the development of numerical and mathematical models, supported by repeatable experimental results, helps simplify the complexity of these interactions. In the next section shall discuss these three physical phenomena separately and explore their interactions with each other.

3.3.1 Electromagnetic field

The challenge in electromagnetic analysis lies in solving a set of Maxwell's equations under specific boundary conditions. The time-harmonic equations governing the physical interface commence with Ampere's law, incorporating displacement currents (referred to as Maxwell-Ampere's law), which do not impose additional computational costs in the frequency domain.

$$\text{Maxwell-Ampere's law: } \nabla \times \boldsymbol{H} = \boldsymbol{J} + \frac{\partial \boldsymbol{D}}{\partial t}, \tag{3.2}$$

$$\text{Maxwell-Faraday's law: } \nabla \times \boldsymbol{E} = -\frac{\partial \boldsymbol{B}}{\partial t}, \tag{3.3}$$

$$\text{and equation of continuity: } \nabla \cdot \boldsymbol{J} = -\frac{\partial \rho}{\partial t}, \tag{3.4}$$

where $\boldsymbol{H}$ is the magnetic field strength, $\boldsymbol{B}$ is the magnetic flux density, $\boldsymbol{E}$ is the electric field intensity, D Electric flux density, and $\boldsymbol{J}$ is the electric current density associated with free charges. Provided that the field quantities are harmonic that can write as

$$\boldsymbol{J} = \gamma \boldsymbol{E} + \mathrm{j}\omega D + \gamma v \times \boldsymbol{B} + \boldsymbol{J}_e. \tag{3.5}$$

Substituting Equation (3.5) into Equation (3.2),

$$\nabla \times \boldsymbol{H} = \boldsymbol{J} + \frac{\partial D}{\partial t} = \gamma \boldsymbol{E} + \mathrm{j}\omega D + \gamma v \times \boldsymbol{B} + \boldsymbol{J}_e + \frac{\partial D}{\partial t}, \tag{3.6}$$

where γ is the electrical conductivity, v is the velocity of the inductor, and $\boldsymbol{J}_e$ is the externally generated current density.

$$\boldsymbol{J}_e = \frac{N l_{coil}}{S} e_{coil}, \tag{3.7}$$

Introducing additional relations necessary for solving Maxwell's equations given as

$$\boldsymbol{B} = \nabla \times \boldsymbol{A}, \tag{3.8}$$

$$\boldsymbol{E} = -\mathrm{j}\omega \boldsymbol{A}, \tag{3.9}$$

where $\boldsymbol{A}$ is the magnetic vector potential, and ω is the angular frequency.

3.3.2 Thermal field

Electromagnetic induction heating utilizes default settings that employ a combined step to solve both electromagnetic and temperature fields. However, one challenge in induction heating is attaining the desired surface-to-core temperature distribution. The centre of the workpiece heats more slowly than the surface, primarily because of the skin effect, as mentioned earlier.

$$\rho_m c_p \frac{\partial T}{\partial t} + \rho_m c_p u \cdot \nabla T = \nabla \cdot (k \nabla T) + Q_e, \tag{3.10}$$

where Q_e represents the electromagnetic loss (W/m^3), u is the conductor velocity $(mm/\ )$, Q_{rh} is the resistive losses, Q_{ml} is the magnetic losses, R_e is the electric resistance, and ω is the angular velocity, given as

$$Q_e = Q_{rh} + Q_{ml}, \tag{3.11}$$

$$Q_{rh} = \frac{1}{2} R_e (\boldsymbol{J} \cdot \mathbf{E}), \tag{3.12}$$

$$Q_{ml} = \frac{1}{2} R_e (i\omega \boldsymbol{B} \cdot \mathbf{H}). \tag{3.13}$$

Figure 3.4 illustrates the challenge of managing the temperature at two sites under normal conditions without controlling the input power. The temperature at the surface is increasing rapidly, while the temperature at the core is rising gradually.

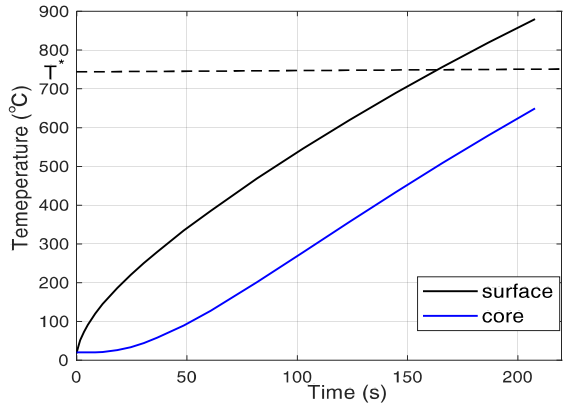

Figure 3.4: Temperature vs. time curve

This discrepancy leads to surface deterioration of the workpiece, resulting in premature current cancelation before the core reaches the desired temperature.

3.3.3 Solid mechanics

During heating or cooling, the workpiece undergoes thermal expansion or contraction, resulting in thermal stress. This is because the surface and interior of the materials experience different temperatures because of rapid heating or cooling. Induction heating exposes materials to such conditions due to rapid temperature changes. This thermal gradient induces localised movement within the material, leading to the initiation and propagation of cracks. Therefore, the analysis of thermal stress is essential as it predicts the deformation and stress caused by temperature variations, thereby determining the thermal stability and susceptibility to extreme stress.

$$\sigma = E\alpha(T_f - T_0) = E\alpha\Delta T, \tag{3.14}$$

Where σ is the thermal stress, E is Young's modulus, α is the thermal expansion coefficient, T_f and T_0 are the final and initial temperatures, respectively.

Thermal stress causes the body to produce thermal strain. The thermal strain $\{\varepsilon^T\}$ and its increment $\{\Delta\varepsilon^T\}$ are typically expressed by the following equation, employing either the average thermal expansion coefficient α_0 or the instantaneous thermal coefficient (Ma et al., 2022).

$$\{\varepsilon^T\} = \{\alpha_0, \alpha_0, \alpha_0, 0,0,0\}^T(T - T_{ref}) \tag{3.15}$$

The increment of thermal strain can be given as

$$\{\Delta\varepsilon^T\} = \{\alpha, \alpha, \alpha, 0,0,0\}^T\Delta T \tag{3.16}$$

Where, T, ΔT, and T_{ref} are the current temperature, temperature increment, and reference temperature for defining the average thermal expansion coefficient, respectively.

$$\alpha(T) = \alpha_0(T) + \frac{d\alpha_0(T)}{dT}\left(T - T_{ref}\right) \tag{3.17}$$

In addition to the thermal expansion-induced strain, a change in volume resulting from phase transformation, fluctuations in Young's modulus, and shifts in yield stress as a result of temperature changes will all contribute to additional thermal strain.

3.4 Case study and applications

3.4.1 Materials

Common materials for shaft preparation are high-quality carbon steel, while plain carbon steel is also commonly used for lightly loaded shafts. The objective of induction hardening is to use inexpensive low carbon or medium-carbon steels (i.e., 4140 or 4340), as they acquire high strength and good toughness upon hardening (through induction hardening flame hardening, or nitriding processes). However, induction hardening is preferred in the automotive and aerospace industries due to its environmental friendliness, rapid processing, corrosion resistance, and energy efficiency.

Numerous mechanical components, including shafts, gears, and sprockets, undergo surface treatments after machining to improve their wear resistance and durability. The effectiveness of these treatments relies on the modification of the properties of the surface material and inducing residual stress. The process creates a resilient core with residual tensile stresses and a hardened surface layer with compressive stress.

Low-alloyed medium-carbon steels, treated with induction surface hardening, are extensively used in essential automotive and machine roles necessitating superior wear resistance. The wear resistance characteristics of parts subjected to induction hardening depend on the depth of hardening and the magnitude and distribution of residual compressive stress present in the surface layer. In this study, AISI 4340 was selected for its outstanding combination of strength and toughness, which outperforms many carbon-hardened steels (Tong et al., 2018).

Table 3.1: Chemical compositions of AISI 4340 (wt.%) (Penha et al., 2015)

Elements	C	Mn	Si	Ni	Cr	Mo
Composition limits	0.38-0.43	0.60-0.80	0.15-0.35	1.65-2.00	0.70-0.90	0.20-0.30

The geometry under examination consists of a bar made from AISI 4340 alloy steel, with dimensions of 100 mm in length and 20 mm in radius (Figure 3.6). Analysis was carried out using COMSOL Multiphysics version 6.0, which incorporated a sufficiently large artificial boundary and a fine mesh.

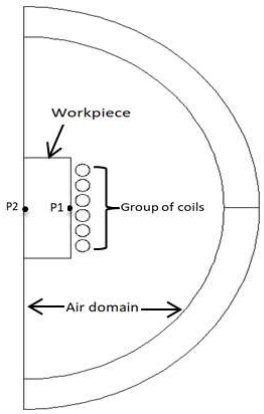

Figure 3.5: Geometry setup for induction heating

Table 3.2: Geometric data

Length of the workpiece	100 mm
radius of the workpiece	20 mm
Workpiece material type	AISI 4340 steel
Number of loops	6
Diameter of the copper wire	10 mm
Distance between the centre of two copper wires	16 mm
Gap between the workpiece and copper winding	3 mm

The conductor used in the model is a homogenized multiturn coil with a coil current of 200A and a frequency of 12.5 kHz over 60 s.

3.4.2 Solution methods and discretization

The electrical and thermal fields of induction heating must be effectively coupled to achieve the desired hardness profile (Barglik et al., 2021b). This process involves three key step of analysis. First, a COMSOL Multiphysics 2D/3D model was created, considering both the material properties and the machine parameters. Second, a comprehensive examination of the temperature distribution, surface characteristics, and depth of the case was conducted by varying the machine parameters to achieve the target temperature. During this phase, the current density of the coil, which is responsible for supplying power and facilitating heat transfer to the workpiece, was also determined. Finally, a sensitivity study was conducted using various statistical tools to assess the hardness profile under different settings of machine parameters.

The finite element method (FEM) was used to simulate the model. In COMSOL Multiphysics, from the mathematics branch, ODE and DAE interfaces, as well as events for process control involved in the setting. This branch of physics offers a distinct foundation for study and aids in algorithm development. The start of the process, the event duration, and the re-initialisation condition were all discreetly configured. Three distinct algorithms were developed to assess the temperature distribution from the surface to the core: explicit and implicit event control algorithms, along with discrete frequency control synchronised with the coil current. These methods are significantly advantageous for achieving the target temperature of conductor materials, including irregular shapes.

Adjusting the power of the coil provides another effective method of controlling the heat source. This adjustment can be easily accomplished by appropriately varying the coil voltage. It is known that the coil power is directly proportional to the square of the voltage. Consequently, the power density of electromagnetic heat sources can be regarded as a convenient time-dependent control function commonly used in the induction heating process.

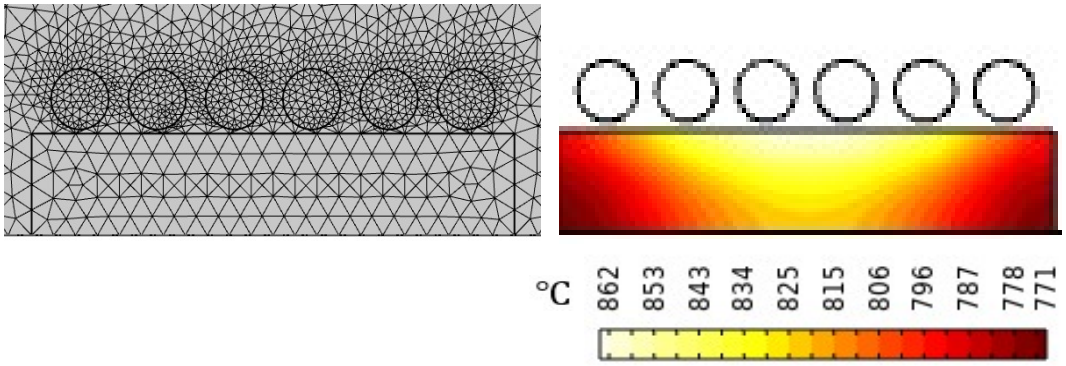

Figure 3.6: Finite element mesh (left) and isothermal contour (right)

In both explicit and implicit event control approaches, the power supplied intermittently turns the switch on or off. In explicit event control, the state of an event is defined over a period. This method is computationally costly and time-consuming, conditionally stable, and meant for simulating short transient dynamic events. In implicit event control, the event is not directly defined over the period, but an indicator is. When the indicator point is reached, the switch is turned off and then on again.

Implicit methods are typically employed to simulate static or less transient phenomena. Time integration within fully transient methods addresses dynamic events. The advantage of implicit

methods lies in their unconditional stability for larger time steps and computational efficiency. However, challenges such as convergence issues and difficulty in capturing dynamic responses persist in implicit methods.

There are multiple approaches to estimating an acceptable deviation in the final temperature distribution from the desired one. Typically, it is necessary to specify a fixed maximum absolute value for the temperature variation. This implies ensuring that, at the end of the heating process, the temperature at any point within the workpiece does not exceed the prescribed value ε from the desired temperature T^*.

$$\max_{l\in[0,1]} |T(l, t_0 + \Delta t) - T^*| \leq \varepsilon, \tag{3.18}$$

where l is the radial direction of the cylinder vary from 0 to 1, ε is prescribed tolerance, T^* is a desired temperature.

The deviation of the final temperature distribution from the desired one is of equivalent importance, as in the case of uniform heating. Therefore, the objective of the heating process prior to subsequent hot working operations is to establish a desired temperature profile within the workpiece that meets specific heating requirements. In the following section, Equation (3.18) will be solved using different approaches within COMSOL Multiphysics version 6.0.

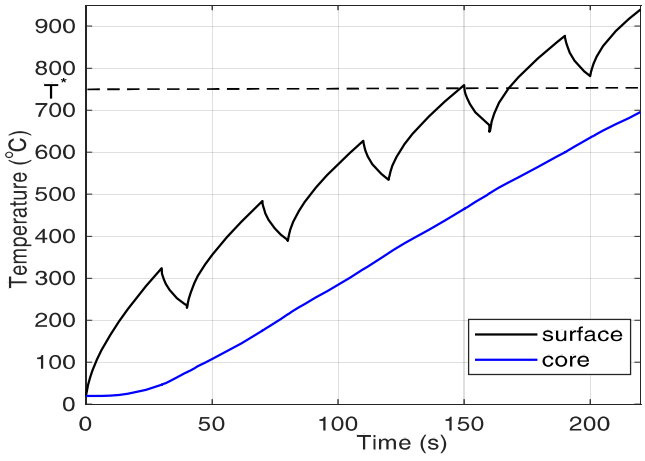

Figure 3.7: Explicit controlled event

In Figure 3.8a, the input power control uses an explicit event control technique, where the process events are explicitly described and synchronised with the coil current to control the switch. The computation duration was 210 s with a coil current 260 A and current frequency 6.5 kHz. The

term “pulse heating” refers to a series of “on” and “off” cycles that continue until the desired (usually uniform) temperature is achieved. This approach improves the effectiveness of induction heating, reduces the heating time, and maintains the consistency of the temperature from the surface to the core.

Optimal selection of power, frequency, and coil length in induction heating involves subjective decisions influenced by factors such as the metal being heated, desired temperature uniformity, and duration of heating. Among these parameters, frequency is of significant importance. When the frequency is too low, it can cause cancelation of the eddy current within the heated material, ultimately reducing the efficiency of the coil.

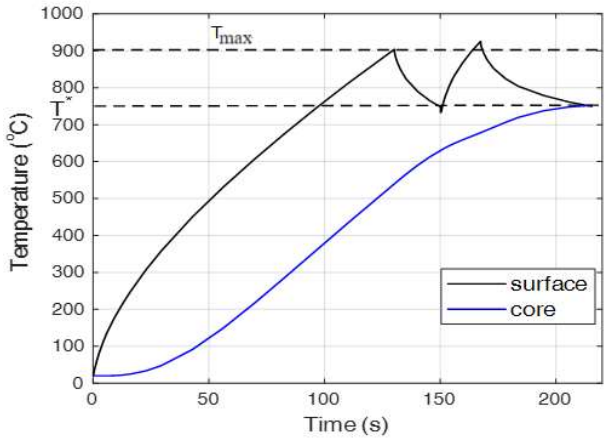

a)

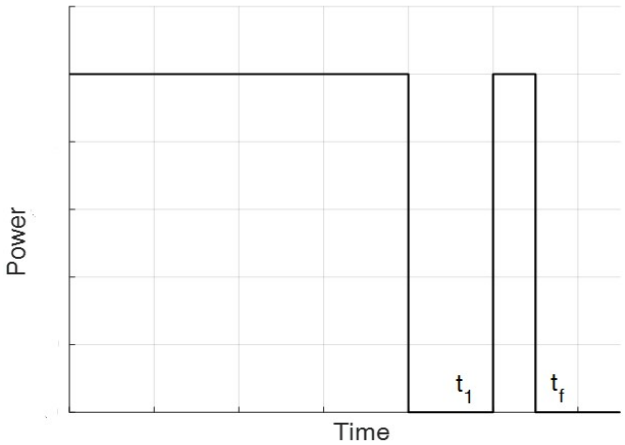

b)

Figure 3.8a: Implicitly controlled event, and 3.8b: Duration of power vs. time

On the contrary, when the frequency is excessively high, the skin effect becomes significantly pronounced, causing the current concentration to be reduced within an extremely thin

surface layer relative to the diameter/thickness of the heated component. This condition might not affect materials with high thermal conductivity (i.e., aluminium, copper). This requires prolonged heating time to ensure adequate heating of the internal areas and core. However, prolonged heating durations lead to increased radiation and convection heat losses, which reduces the thermal efficiency of the induction heater. Therefore, selecting an appropriate frequency is always a matter of finding a reasonable compromise.

The computation duration was 210 s with the coil current 320 A and the current frequency 10 kHz. When the event meets the indicator condition, it switches on or off. The indicator state controls the induced current switch in this scenario, and the process repeats. With the higher and lower temperature limits set, strict control is imposed on the surface temperature not to exceed these boundaries. Consequently, the temperatures of both points converge towards the same value.

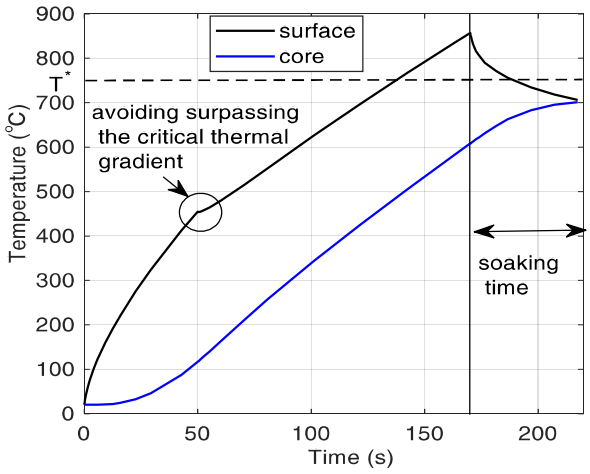

Figure 3.9: Modification of accelerated heating

The control process faces a complication arising from the challenges associated with achieving the desired spatial distribution of internal heat sources. Many existing methods for controlling the power distribution are constrained by strict limitations to produce the required spatial distribution of internal heat sources. This limitation is particularly evident when certain metals have fixed frequency inverters, as the frequency is uniquely determined by the law of electromagnetic wave propagation in metals.

Low frequency is applicable to heat large areas of the workpiece without affecting the surface. However, this method results in long heating durations, leading to inadequate heating of the surface area. Consequently, achieving a uniform desired temperature at the required location

becomes challenging. However, high frequency offers good energy efficiency as a result of a high-power supply but is limited to heating only the surface. This limitation results in a lack of proper thermal energy distribution across a large area of the workpiece, which affects its desired mechanical properties.

The ability to adjust control output power and frequency while ensuring thermal gradients remain below critical values helps us achieve optimised heating durations. Figure 3.9 illustrates high-frequency heating with power breaks implemented to prevent exceeding critical values of the thermal gradient. This approach helps to avoid accelerated thermal gradients and reduces the duration of heating. Furthermore, at the end of the heating duration, the soak stage is crucial to achieving the desired temperature profile. The computation duration was 210 s with a coil current parameter of 260 A, high current frequency 7kHz, low current frequency 4 kHz, and 50 s soaking duration.

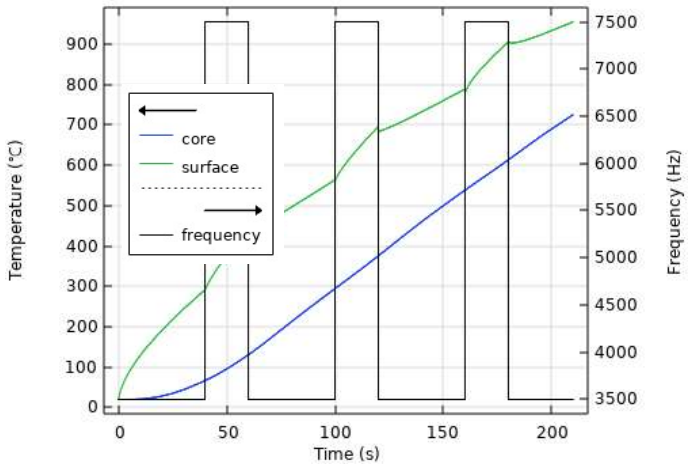

Figure 3.10: Asynchronised frequency-controlled event

The asynchronous dual-frequency approach employs two distinct frequencies that alternately become active as the event condition dictates. Lower frequencies allow significant current penetration and a deeper skin effect, making them more efficient for heating larger parts. At high frequencies, current penetration is limited to the surface. On the contrary, higher frequencies restrict current penetration, and influence eddy current generation within the workpiece.

In Figure 3.10, the dual frequency setup is depicted with frequencies set at 3.5 kHz and 7.5 kHz, displayed on the right side of the graph. The frequencies are arranged to operate sequentially,

with one following the other for a specified time duration. This alternating activation pattern affects current penetration, particularly surface current and temperature.

3.5 Boundary conditions

Careful consideration must be given to the selection of boundary conditions, as artificial reflections at the boundary of the air domain can alter finite-element computations of electromagnetic fields within the air. In this study, the Robin boundary condition (a weighted combination of the Dirichlet and Neumann boundary conditions) was employed for an enclosed surrounding air domain with dimensions wide enough to avoid perturbation of magnetic field lines.

The surface boundary conditions of induction heating involve the three modes of heat transfer: conduction, convection, and radiation.

$$-k\frac{\partial T_s}{\partial n} = \alpha(T_s - T_0) + \sigma C(T_s^4 - T_r^4). \tag{3.19}$$

At the axis of symmetry,

$$n \cdot (-k\nabla T) = 0. \tag{3.20}$$

Here, T_s is the temperature of surface of the heat source, α is the coefficient of convective heat transfer, T_0 denotes the temperature of the surrounding medium (air), $\sigma = 5.67 \times 10^{-8}\ \mathrm{W/m^2K^4}$ is the Stefan-Boltzmann constant, C stands for the emissivity of the heated body and T_r is the temperature of the surface to which the heat is radiated and all are nonlinear functions of the temperature.

In induction heating problems, boundary conditions include heat losses due to convection. In this case, the boundary condition of the third kind can be written as (Rapoport & Pleshivtseva, 2007).

$$\frac{\partial\theta(1,t)}{\partial l} = \mathrm{Bi}\big(\theta_a(t) - \theta(1,t)\big), \tag{3.21}$$

where $\partial\theta/\partial l$ is the temperature gradient of the surface at the point under consideration, , $Bi = \alpha X/$ is the Biot number, l depth along radial direction $= x/X$, t denotes time, α is the convection heat transfer coefficient, X is the radius of the workpiece and $\theta_a(t)$ denotes a relative value of ambient temperature $T_a(\tau)$; calculated as:

$$\theta_a(t) = \frac{T_a(\tau) - T_b}{P_{max}X^2}k \tag{3.22}$$

where T_b is the base temperature, P_{max} is the maximum power, k is the thermal conductivity.

Heat loss at the surface of the workpiece is highly fluctuating because of the nonlinear nature of convection losses. Since the heated body is geometrically symmetric along the axis of symmetry, the Neumann boundary condition can be formulated as;

$$\frac{\partial\theta(0,t)}{\partial l} = 0, \tag{3.23}$$

$$\frac{\partial\theta(1,t)}{\partial l} = q(t) < 0, \tag{3.24}$$

where $q(t)$ denotes the relative value of heat losses. The condition in Equation (3.21) implies that the temperature gradient in a direction normal to the axis of symmetry is zero, which means that no heat exchange occurs on the axis of symmetry.

$$q(t) = \frac{Q_s(t)}{P_{max}X}, \tag{3.25}$$

where $Q_s(t)$ is a flow of heat loss from the surface of the heated body.

3.6 Temperature and electric power density

The primary flow of the generated current is concentrated within the surface layer, with its depth determined by factors such as the frequency of the alternating field, the density of surface power, the permeability of the material, the duration of heat and the diameter of the workpiece or the thickness of the material.

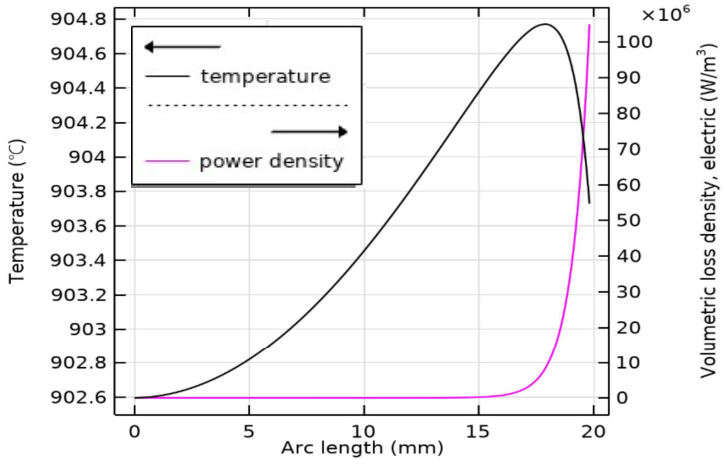

Figure 3.11: Electric power density along the radial direction

Quenching this heated layer in water, oil, or a polymer-based solution alters the surface layer to develop a martensitic structure, enhancing its hardness compared to that of the base metal. In Figure 3.11, a high electric power density (W/m^3) has observed on the surface of the workpiece followed by a high temperature value.

To optimise the design, manufacturers of induction heating systems must prioritise minimising losses in system components and maximising energy transfer to the load. These are key strategies to improve overall efficiency. Combining both electrical and thermal efficiency provides a comprehensive measure of the system's effectiveness in converting electrical energy into useful heat for the intended application. Many factors influence the efficiency of induction heating, which requires collective improvements to achieve the desired efficiency of the system.

Electrical efficiency can be influenced by various factors, including the design of the power supply, the frequency of the alternating current, and the quality of the coil. Thermal efficiency, on the other hand, gauges how effectively the electromagnetic field generated is converted into heat within the load. Factors affecting thermal efficiency encompass the design and material of the inductor coil, the distance between the coil and the workpiece, and the frequency and power settings.

Chapter 4

Mathematical modelling of thermal stresses in induction surface hardening

4.1 Induction surface hardening methods

Surface hardening involves a wide variety of techniques designed to improve the wear resistance of components without affecting their softer and tough interior. These techniques are categorised into three: thermochemical diffusion methods, applied energy (thermal methods), and surface coating (modification) techniques (Davis, 2002). The first method, thermochemical diffusion, involves modifying the chemical composition of the surface by introducing hardening elements such as carbon, nitrogen, and boron. These techniques effectively harden the entire surface of a part and are commonly used for large-scale surface hardening projects. Examples of these methods include carburising, nitriding, carbonitriding, nitrocarburising, boriding, and thermal diffusion processes. The second method, applied energy or thermal methods, does not alter the chemical composition of the surface. Instead, they enhance properties by modifying the surface metallurgy. In other words, they create a hardened surface through quenching without introducing additional alloying species. Examples of these methods include flame hardening, induction hardening, laser beam hardening, and electron beam hardening. The third is surface coating, or surface modification methods involve intentionally adding a new layer onto the steel substrate or altering the subsurface chemical composition, as seen in ion implantation. Examples of these methods include hard chromium plating, electroless nickel plating, thermal spraying, weld hard facing, chemical vapour deposition, physical vapour deposition, ion implantation, and laser surface processing.

The distribution of hardness in the hardened material can be determined from the CCT diagram provided that the austenitisation temperature and the cooling rate are known with a sufficient accuracy (Geng et al., 2020). The cooling model can be well described and solved numerically when the convective coefficient of heat transfer is known. Its value (or its temperature dependence), most of which is unknown in advance, must be found by measurement of the temperature in selected parts of the hardened sample, on its surface, and in its interior. The contents of the steel levels in the interior are then estimated from the CCT diagram (Figure 4.6). However,

the results must be considered only indicative because both the CCT diagram and the level domains exhibit uncertainties and vary from manufacturer to manufacturer.

4.2 Applications of surface hardening

There are numerous applications associated with induction surface hardening, which is required to enhance strength and wear resistance. For example, crankshafts, axle shafts, modern transmission shafts, and gears are among the components that require surface hardening. The induction hardening process for crankshafts, axles, and transmission shafts is increasingly becoming automated (Dziatkiewicz et al., 2023). The control system of this line is designed to enable decision making with a programmable controller. Consequently, all aspects of the heat treatment process and mechanical operations are pre-programmed and can be easily adjusted to accommodate various part sizes and heat treatment parameters. With such a process, users have managed to increase production rates compared to those achievable with conventional heat treatment.

Most induction surface hardening requires high power densities and short heating cycles to restrict heating to the surface area. The main metallurgical advantages of induction-based surface hardening include increased wear resistance and improved fatigue strength.

4.3 Basics of thermal stress analysis

4.3.1 Thermal expansion and material behaviour

Induction hardening is a form of transformation hardening, involves heating the surface layer beyond the critical temperature Ac_1 to trigger austenitization, followed by quenching to form hardened martensite. It is based on the fundamental principles of physical metallurgy, which connect processing, properties, and structure. Properties such as strength, ductility, and toughness, which are highly influenced by structure, play an important role in determining the feasibility of manufacturing processes, performance during service, and limitations under service conditions. The development of thermal stresses, crucial in this context, is significantly influenced by factors such as thermal conductivity, heat capacity, and thermal expansion shown in Figures 4.1 and 4.2. The magnitude and variation of these residual stresses are primarily influenced by the carbon content, with alloying elements having a lesser impact (Grum, 2001).

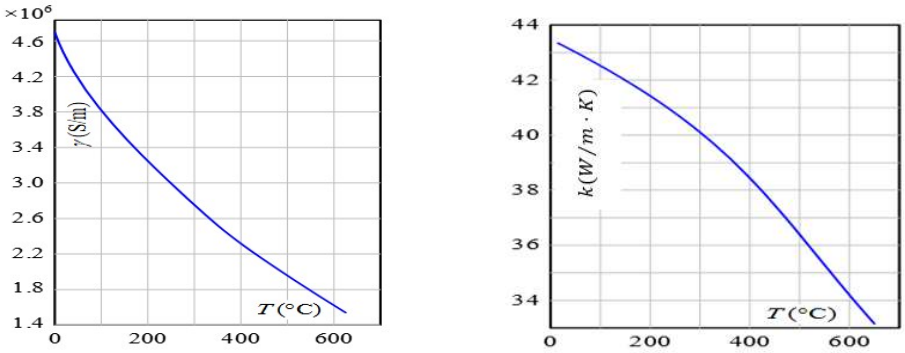

Figure 4.1: Electrical conductivity (left) and thermal conductivity (right) as function of temperature (steel AISI 4140)

In the domain of induction heating, the development of thermal stress is dictated not only by material properties that; electromagnetic properties also play a significant role. Key electromagnetic properties such as electrical resistivity (or electrical conductivity) and magnetic permeability significantly influence the depth of heating. Consequently, the electrical resistivity and relative magnetic permeability of the workpiece exert a substantial impact on various aspects of an induction heating system, including coil efficiency, selection of primary design, and process parameters. In certain electrically conductive materials, electrical resistivity decreases with increasing temperature. In contrast, for most steels and cast irons, electrical resistivity increases with temperature, following a nonlinear trend (Rudnev et al., 2003).

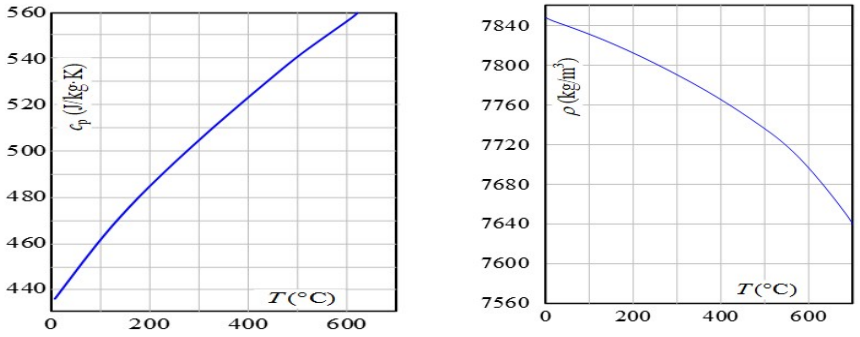

Figure 4.2: Specific heat (left) and specific mass (density) (right) as a function of temperature (steel AISI 4140)

4.3.2 Distortion and residual stresses

Distortion during induction hardening can occur during austenitizing or during quenching. Austenitizing-induced distortion usually arises from the release of residual stresses accumulated

during prior processes such as forging or machining, as well as from nonuniform heating (Bedekar et al., 2019). When only the surface of the part is austenitised and hardened, the cooler core metal helps minimise distortion. Moreover, the use of induction scanning, which heats only a small section of the workpiece at any given time, proves advantageous in preventing such problems. This scanning method has also been shown to be effective in keeping distortion levels low in through-hardening applications. Particularly in the case of symmetric parts, rotating the component improves heating uniformity and reduces the chances of irregularities in the final shape (Rego et al., 2018)(Samuel & Prabhu, 2022; Totten et al., 2002).

The distortion caused by the quenching process is largely a function of the austenitizing temperature, the uniformity of the quenching process, and the choice of the quenching medium. Higher austenitizing temperatures, which induce higher residual stresses, result in increased non-uniform contraction during cooling. Severe quenching mediums, such as water or brine, known for their ability to create substantial residual stresses, can also lead to significant distortions.

Distortion can cause cracking, which is closely related to the design of the part and the development of residual stresses. Components with significant variations in cross-sectional area present notable challenges during the heat treatment process. Moreover, there is often a critical case depth beyond which cracking becomes unavoidable. In such cases, tensile stresses near the surface of the induction-hardened part, which counteract the compressive residual stresses formed, contribute to the issue of cracking (Samuel & Prabhu, 2022a; Totten et al., 2002).

The steel composition also contributes to the susceptibility to cracking in induction hardening applications, with this susceptibility increasing with higher levels of carbon or manganese (Davis, 2002; Prisco, 2018). The influence of carbon content on the tendency towards quench cracking is most significant in through-hardened parts, primarily due to its effect on lowering the martensite start (M_s) temperature and impacting the hardness of the resulting martensite.

4.3.3 Mathematical modelling

The process of hardening itself consists of two parts: induction heating and subsequent cooling. The time gap between both processes is very short and will not be considered. The induced electromagnetic field in the workpiece is governed by Maxwell's equations. For an axisymmetric

problem in cylindrical coordinates (r, z), the key equation is the azimuthal component of the magnetic field $\boldsymbol{H}_{\phi}$:

$$\frac{\partial}{\partial r}\left(r\mathbf{H}_{\phi}\right) + \frac{\partial}{\partial z}(r\mathbf{E}_{z}) = -\mu_0\gamma\frac{\partial T}{\partial t}, \tag{4.1}$$

where μ_0 is the permeability of free space, γ is the electrical conductivity, $\mathbf{E}_z$ is the electric field intensity, and T is the temperature.

The heat generated by the induced currents increases the temperature of the material. The heat conduction equation in cylindrical coordinates for an axisymmetric process is as follows:

$$\rho c_p \frac{\partial T}{\partial t} = \frac{1}{r}\frac{\partial}{\partial r}\left(rk\frac{\partial T}{\partial r}\right) + \frac{\partial}{\partial z}\left(k\frac{\partial T}{\partial z}\right) + q, \tag{4.2}$$

where ρ is the density, c_p is specific heat capacity, k is the thermal conductivity and q is the volumetric heat generation due to induction heating.

Induction heating is a coupled problem characterised by a non-linear interaction of the magnetic and temperature field. Assume that the displacement current is negligible; the diffusion equation that describes electromagnetic phenomena can be written as (Karban & Donátová, 2010).

$$\gamma\frac{\partial \boldsymbol{A}}{\partial t} - \nabla\left(\frac{1}{\mu}\nabla\mathbf{A}\right) - \gamma v \times \mathbf{A} = \mathbf{J}_s, \tag{4.3}$$

$$\nabla \cdot (k(t)\nabla T) = \rho_m c_p\left(\frac{\partial T}{\partial t}\right) - w_{J,} \tag{4.4}$$

where $\mathbf{A}$ is the magnetic vector potential, μ is the magnetic permeability and $\mathbf{J}_s$ represents the current density delivered to the inductor from the source, k(t) is the thermal conductivity of the material, ρ_m denotes the specific mass density, T is the temperature, c_p stands for the specific heat at a constant pressure and w_J are the volumetric Joule losses.

The next equation accompanying the heating and cooling processes is the phase transformation. At the beginning of heating $(t = t_0)$, the steel workpiece contains more levels of steel (martensite, pearlite, bainite and ferrite), whose partial percentage is unknown, but this mixture denoted as z_0 and $z_0(t_0) = 1$. At the end of heating (time t_1), the outer layers of the workpiece are transformed into austenite (denoted as z_1, about 98 %), but there remains small amount of ferrite, pearlite, and bainite. After cooling (time t_2), a mixture of ferrite (z_2), pearlite (z_3), bainite (z_4), and about 98 % of martensite (z_5) was obtained.

In accordance with the previous text and (Areitioaurtena et al., 2022) given by

$$z_0(t_1) + z_1(t_1) = 1, \tag{4.5}$$

$$z_1(t_2) + z_2(t_2) + z_3(t_2) + z_4(t_2) + z_5(t_2) = 1. \tag{4.6}$$

Another field that directly affects the mechanical stresses in the material is the field of deformations. This is modelled independently of the magnetic field, but the temperature field must be considered.

For mapping of this field considering only small deformations and balance of momentum without inertial terms. In such a case, the following equations hold

$$\nabla \cdot \sigma = 0, \tag{4.7}$$

$$\rho_m \dot{e} + \nabla \cdot q = \sigma : \varepsilon(\dot{u}) + Q \tag{4.8}$$

where σ is the stress tensor, ρ denotes the specific mass density, e stands for the volumetric internal energy, q represents the volumetric heat flux, u is the vector of displacement, $\varepsilon(\dot{u})$ represents the symmetric part of the strain rate tensor and Q denotes eventual external heat source. Symbol ":" stands for the scalar product in $\mathbb{R}^{3\times3}$.

The total strain $\varepsilon(u)$ additively decomposed into elastic part ε^{el}, thermal part ε^{th} and nonelastic part induced by phase transformation, denoted by ε^{TRIP} part (Hömberg, 2004b).

$$\varepsilon(u) = \varepsilon^{el} + \varepsilon^{th} + \varepsilon^{TRIP} \tag{4.9}$$

Equations (5) and (6) have to be supplemented with the Fourier and Hooke laws

$$q = -k\nabla T, \tag{4.10}$$

$$\sigma = C \cdot \varepsilon^{el}. \tag{4.11}$$

Here C is the isotropic stiffness tensor. The symmetric part of the strain rate tensor can be written as (Hömberg, 2004b; Montalvo-Urquizo et al., 2013)

$$\varepsilon(\dot{u}) = \frac{1}{2}(\nabla u + \nabla u^T) \tag{4.12}$$

The thermal strain can be expressed in terms of the thermal expansion caused by density variations. Changes in density of levels in steel can also be used to describe both thermal and transformation strains in a unified way which can be written as

$$\rho_m(T, z) = \sum_{i=1}^{5} z_i \rho_i(T), \tag{4.13}$$

where $\rho_m(T)$ is the measured homogenous temperature dependent density of the level z_i. Then the thermal strain is given as

$$\varepsilon^{th} = \left(\left(\frac{\rho_0}{\rho\ (T,z)}\right)^{1/3} - 1\right) \cdot I\ , \tag{4.14}$$

where ρ_0 is the homogenous measured density of initial phase configuration $z_0(t_0)$ at the initial temperature $T(t_0)$ and I is the unit matrix.

The TRIP model (transformation-induced plasticity), used exclusively during the cooling process, is derived from the Franitza-Mitter-Leblond proposal (Wolff et al., 2006, 2007; Wölfle et al., 2022). For the case of multiphase formations, the corresponding equation will be

$$\begin{cases} \varepsilon^{TRIP}\ (t) = 0 & t \le t_1 \\ \dot{\varepsilon}^{TRIP}(t) = \frac{3}{2}\sigma^* \sum_{i=2}^{5} K_i^{gj}\left(T(t), z_i\ (T(t),t)\right) \frac{d\phi_1(x)}{dx}\Big|_{z_1(\theta(t),t)} \dot{z}_1(T(t),t),\ t_1 \le t\ \le t_2 \end{cases} \tag{4.15}$$

where $\sigma^* = \sigma - 1/3\,\sigma \mathrm{I}$ is the stress deviator, $\mathrm{K_i^{gj}} \in \mathrm{C}(\mathbb{R} \times [0,1])$ the respective Greenwood-Johnson parameter possibly depending on $\mathrm{T}, \mathrm{z_i}\,(\mathrm{i} = 2, \ldots, 5)$, t and $\phi_1 \in \mathrm{C}[0,1] \cap C_1(0,1)$ the monotone saturation function with $\phi_1(0) = 0, \phi_1\ (1) = 1$. Here volume conservation for the TRIP deformation is assumed as, $\mathrm{tr}(\varepsilon^{\mathrm{TRIP}}) = 0$

Substituting for ε^{el} into the Hooke law Equation (4.9) can be written as

$$\sigma = E \cdot [\varepsilon(u) - \varepsilon^{th} - \varepsilon^{TRIP}]. \tag{4.16}$$

Let the constants L_A , L_F , L_P , L_B , and L_M , indicate the latent heats of the z_0 phase change: austenite, austenite-ferrite, austenite-pearlite, austenite-bainite, and austenite-martensite, respectively. The equations derived to describe the heating process (Taleb & Sidoroff, 2003)

$$\rho_m c_p \left(\frac{\partial T}{\partial t}\right) - \nabla \cdot (k(t) \nabla\, T) = -L_A \dot{z}_1 + \sigma : \varepsilon(\dot{u}) + Q, \tag{4.17}$$

and for the cooling process

$$\rho_m c_p \left(\frac{\partial T}{\partial t}\right) - \nabla \cdot (k(t) \nabla T) = L_F \dot{z}_2 + L_P \dot{z}_3 + L_B \dot{z}_4 + L_M \dot{z}_5 + \sigma : (\varepsilon^{th} + \varepsilon^{TRIP}). \tag{4.18}$$

4.3.4 FEA of induction surface hardening

A computer experiment was carried out on a simple case of induction surface hardening of a cylinder made of steel AISI 4140 (Table 4.1). The workpiece has a radius of 20 mm and a length of 100 mm. The experimental data was collected at points A, B, C, and D (Figure 4.3). Six copper

conduction coils surrounded the workpiece, through which sinusoidal currents flowed at an operating frequency of approximately 20 kHz. These currents induced eddy currents or power density in the workpiece, resulting in heating its surface temperature to above 900 °C, the required austenitizing temperature.

Moreover, as a result of the temporal fluctuation of temperature throughout the induction heating process, each temperature range within the model was associated with a distinct time duration. The total time required for the induction heating and cooling phases was subdivided into numerous small-time intervals within the numerical solution.

Table 4.1: Percentage of elements in AISI 4140 (Sahin et al., 2019)

C	Mn	Cr	Mo	Si	P	S	Fe
0.45	0.90	1.20	0.30	0.40	0.025	0.035	balance

The tabulated values may, however, change from manufacturer to manufacturer. The density of this steel at room temperature is 7850 kg/m^3 and its melting point is 1416 °C.

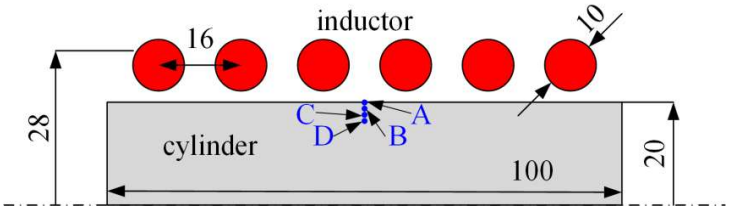

Figure 4.3: Arrangement of the tested cylinder and inductor (all dimensions given in mm)

The computations were performed using the commercial software COMSOL Multiphysics 6.0. FE simulations were used to solve this model numerically with 1360 elements and 972 nodes. A free triangular mesh has been used, covering an area of 0.002 m2, and, due to symmetry, only half of the cylindrical geometry is considered. The chosen mesh is fine, with a focus on quality measures such as skewness. The boundary layer mesh is applied to a depth of 4 mm, consisting of 6 layers with a stretching factor of 1.5, as shown in Figure 4.4. This type of mesh is commonly used to accurately resolve thin boundary layers. This approach facilitates a comprehensive analysis of the quenching process, providing a detailed understanding of the temperature distribution, phase transitions, and mechanical properties over a small depth (surface) of the workpiece. The aim of

the study is to investigate the surface hardness by measuring the depth of the indentations using a conventional hardness scale. It took five hours to complete the calculation on a desktop computer with 3.8 GHz and 1.8 TB of local disk capacity.

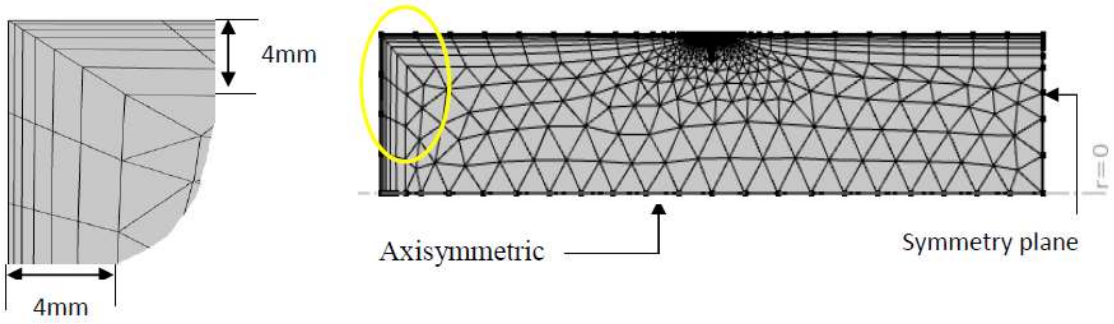

Figure 4.4: Finite element mesh

The workpiece, initially at a temperature of 20 °C, was rapidly heated to 900 ° C in 10 seconds, followed by immediate quenching with water sprayed onto the cylinder. The simulation involves two steps: the first step involves heating to the austenite temperature, where coupled electromagnetic and thermal phenomena occur, while the second step involves cooling to the martensite finish (M_f) temperature.

The cooling rate significantly influences the final microstructure and mechanical properties of the material. Figure 4.5 illustrates the cooling profile on the surface (0.1mm below the surface). The workpiece was cooled by quenching the crossflow water jet at a constant speed (1 m/s), aiming to achieve uniform mechanical properties on the surface. The average cooling rate from maximum temperature (900 °C) to martensite start temperature (350 °C) is about 253 °C/s, which is much higher than the critical cooling rate for martensite transformation in AISI 4140. In the 350 °C to 140 °C range, the average cooling rate is approximately 58.28 °C / s, and below 140 °C, it is approximately 3.70 °C/s. The cooling rate offered by the quenchant should be high enough to exceed the critical cooling rates for achieving desirable mechanical properties. Conversely, the average cooling rate must be slow enough in the martensitic transformation range to minimise distortion in the quenched component.

The highest temperature was observed at point A, reaching approximately 910 °C at the end of the heating process. This value signifies a temperature sufficient for austenite transformation, despite the Ac_3 temperature of this model is 772.60 °C, generated by JMatPro, (Figure 4.6). The

average heat rate in this model is approximately 89.15 ℃/s. The higher heating rate may tend to elevate both Ac_1 and Ac_3 temperatures. This is because the transformation from ferrite/pearlite to austenite is a time-dependent process, and faster heating rates facilitate faster phase transformations.

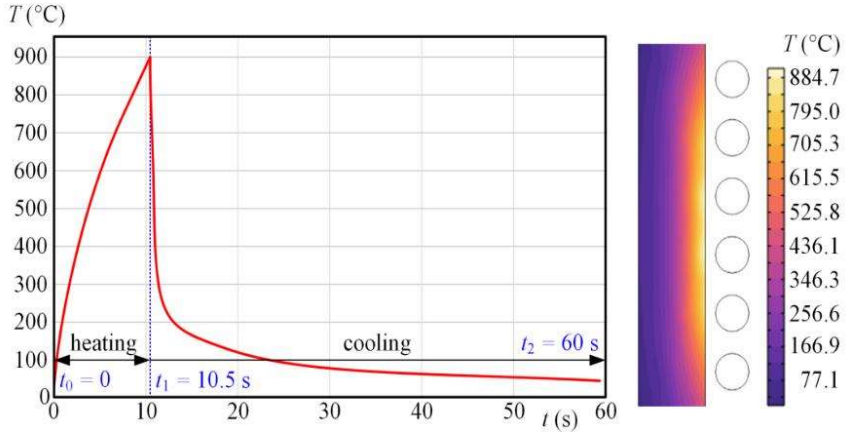

Figure 4.5: The left and right parts show the time evolution of the heating on the surface and the distribution of the temperature in the axial cross section of the cylinder, respectively.

Detail testing confirmed that the process of heating practically does not depend on the value of α and emissivity C (testing was performed for field current 88.3 A and frequency 20 kHz for α ranging from 5 to 20 $W/m^2 \cdot$ K and for C ranging from 0.4 to 0.8). The main role is always played by the field current and its frequency.

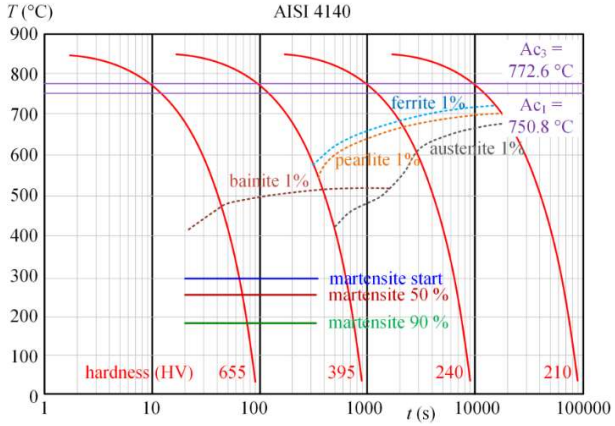

Figure 4.6: CCT diagram of steel AISI 4140

The CCT diagram depends on several factors, including the chemical composition of the steel, the nature of cooling, the grain size, the degree of homogenisation of austenite, as well as austenitizing temperature and time. This diagram was specifically developed for individual steels to document the transformational changes of austenite during the cooling process along the temperature and time axes (typically log time).

The construction of a CCT diagram can be achieved through various methods. In research papers (Mandal et al., 2022; Moravec et al., 2022), dilatometric measurements, structural analysis, and hardness measurements were used to construct CCT diagrams. Alternatively, software programs can be used, as demonstrated in the article (Geng et al., 2020), where the results were compared with the commercial software JMatPro and experimentally determined CCT diagrams.

The curve typically encompasses regions representing various transformations, such as austenite decomposition into ferrite, pearlite, bainite, and martensite. When the CCT curve is used, the optimal cooling rate, and the temperature range can be determined to achieve the desired microstructure and mechanical properties in the final product. The sample was initially austenitised at $900\ °C$ and then cooled at constant rate.

4.4 Modelling thermal stresses

COMSOL Multiphysics can solve coupled harmonic magnetic field and transient thermal problems. The Galerkin method, (Álvarez Hostos et al., 2018; Pant et al., 2010) was employed in the program for both the magnetic and thermal processes. The field equation for an axisymmetric problem in a cylindrical coordinate system is provided as follows.

$$\frac{\partial}{\partial x}\left(\frac{D_x}{x}\frac{\partial}{\partial x}(x\phi)\right) + \frac{\partial}{\partial y}\left(D_y\frac{\partial \phi}{\partial y}\right) + Q = k\frac{\partial \phi}{\partial t}, \tag{4.19}$$

where D_x , D_y , Q and k are linear or non-linear parameters.

When the Galerkin formulation is applied, the weighted residual integral for an axisymmetric time-dependent field problem is expressed as the volume integral (Carrera et al., 2017).

$$\{R^{(e)}\} = \int [N]^T \left(\frac{\partial}{\partial x}\left(\frac{D_x}{x}\frac{\partial}{\partial x}(x\phi)\right) + \frac{\partial}{\partial x}\left(D_y\frac{\partial \phi}{\partial y}\right) + Q - k\frac{\partial \phi}{\partial t}\right) dV = 0, \tag{4.20}$$

where [N] is the row vector comprises the element shape functions, Q is the heat flow rate between nodes i and j .The evaluation of equation (4.19) gives the global matrix equation for axisymmetric problems with equation (4.20) as the governing equations,

$$[C]\{\dot{\Phi}\} + [K]\{\Phi\} = \{F\}, \tag{4.21}$$

where $\{\dot{\Phi}\}$ nodal value vector of $\partial\phi/\partial t$, $\{\Phi\}$ is the nodal value vector, $[C]$, $[K]$ capacity and coefficient matrix respectively, $\{F\}$ is the load vector.

4.5 Initial and boundary conditions

Initial conditions:

$$T(r, z, 0) = T_0, \tag{4.22}$$

where T_0 is the initial uniform temperature of the workpiece.

Boundary conditions:

The boundary condition of the surface subjected to induction heating may include a convective heat loss term and an imposed heat flux from the induction coil. However, during the quenching process, because of the short duration caused by the intense thermal gradient, radiation can be neglected. This concept is further explained in the experimental investigations by (Barglik et al., 2018.; Barglik et al., 2015). They illustrate that the convection heat transfer coefficient, denoted as $\alpha_{cc}(P, Q)$, is a function of the pressure (P) and flow rate (Q) of the quenchant.

$$-k \cdot \frac{\partial T}{\partial n} = \alpha_{cc}(P, Q) \cdot (T - T_q), \tag{4.23}$$

where n denotes onward normal and T_q is the temperature of quenchant.

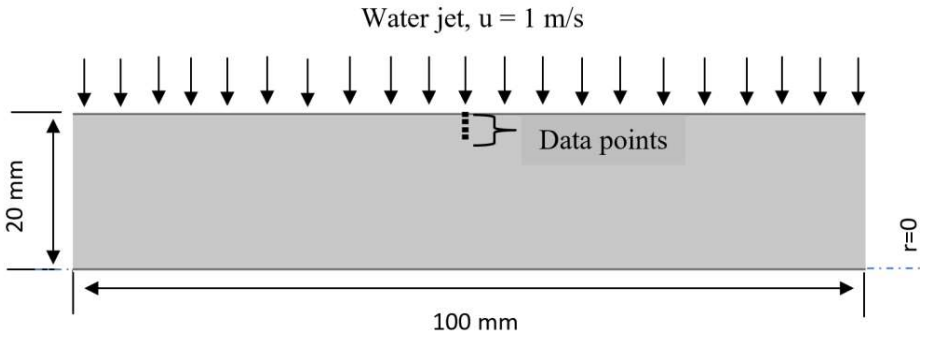

Figure 4.7: Crossflow water jet quenching with constant speed

Figure 4.7 illustrates the computational domain for the quenching of crossflow water jets with a constant speed to achieve uniform mechanical properties. In the FE simulation, the

assumption was made that the nozzle sprays water over the impingement area. The quenchant (water) heated by the workpiece under quenching at the locations of jet impingement experienced an increase in temperature and dispersed radially on the cylinder, gradually losing its velocity.

4.6 Martensite transformation process

The martensitic reaction is initiated during the cooling process, when the austenite reaches the martensite start (M_s) temperature, causing the parent austenite to become mechanically unstable. As controlling the quenching process can be challenging, numerous steels are quenched to generate an excess of martensite, which is then gradually tempered to achieve the desired structure for the intended application. In certain alloys, this effect is reduced by incorporating elements such as tungsten, which disrupt the nucleation of cementite (Canale et al., 2014; Penha et al., 2015).

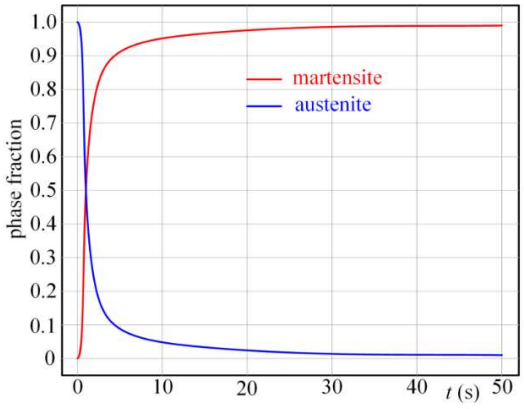

Figure 4.8: Phase decomposition rate vs time

Figure 4.8 shows the time dependence of the percentages of austenite and martensite in the cooling steel on time during the process at point A, and Figure 4.9 shows the phase fractions (austenite and martensite) in the steel as functions of the temperature at the same point. As the cooling rate is very high, the transformation contains neither ferrite nor pearlite or bainite. Therefore, the material consists only of martensite and retained austenite.

As the sample undergoes quenching, a progressively larger proportion of the austenite transforms into martensite until it reaches the lower transformation temperature, M_f, signifying the completion of the transformation. A full conversion to martensite can be achieved when the cooling rapidly reaches the M_f temperature.

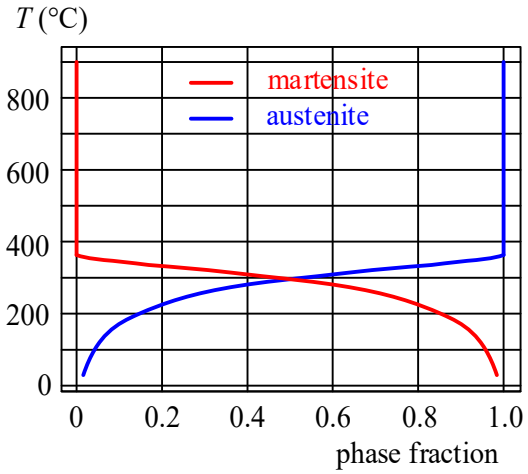

Figure 4.9: The formation and austenite decrease as a function of temperature

In particular, the severity of the quench experienced by the surface martensite, compared to the martensite formed in the core, significantly influences the distribution of residual stresses.

The effective yield stress in the martensitic transformation is the stress needed to initiate and sustain the transition from austenite to martensite. It indicates the stress required to overcome the energy barrier for phase transformation to occur. Its behaviour depends on composition (compound material) and processing conditions.

- Effective yield stress is influenced by various factors, including alloy composition, temperature, strain rate, and microstructure.
- Yield stress is affected by the temperature and strain rate and is generally lower than martensite.
- The martensite yield stress is strongly influenced by the cooling rate, is typically higher than the austenite yield stress, and involves a diffusionless transformation.

Figure 4.10 illustrates the dependence of the yield stress on the temperature and cooling rate. Changes in the cooling rate can influence yield stress by affecting the size and distribution of grains or phases. Rapid cooling can result in the formation of smaller grains in metals.

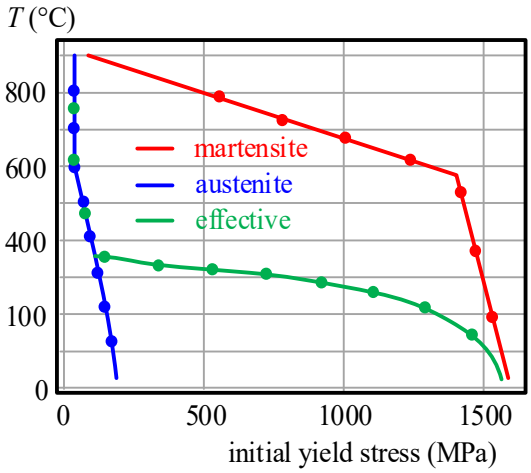

Figure 4.10: Dependence of yield stress in austenite and martensite on temperature

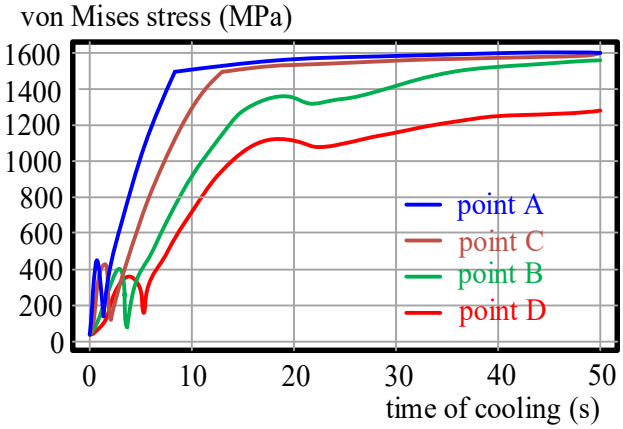

Figure 4.11: Evolution of von Mises stress in material at points A, B, C, and D

Figure 4.11 shows the time evolution of the von Mises stress at points A, B, C, and D during the cooling process. I noticed that the von Mises stress exhibits oscillation during the first few seconds. This occurs because the quenching process initiates rapid tensile stresses on the surface and compression stresses at the core. When the martensitic transformation begins at M_s point on the surface, dilatational phase-transformation strains and the transformation plasticity led to rapid unloading and reverse loading on the surface, which is the reason why von Mises stress shows oscillation at this point.

I observed a non-smooth transition in the graph around 8 to 9 seconds, specifically at point A. This is because point A is located near the surface of the workpiece, while points B, C, and D are within the material. The sharp change at point A is likely due to a sudden drop in thermal stresses at the surface, which inhibits further martensite transformation. In contrast, within the

body, the decrease in thermal stress is more gradual, resulting in subtle changes in von Mises stress. This difference highlights the variations in the shapes of the curves (A, B, C, D) at the M_f temperature.

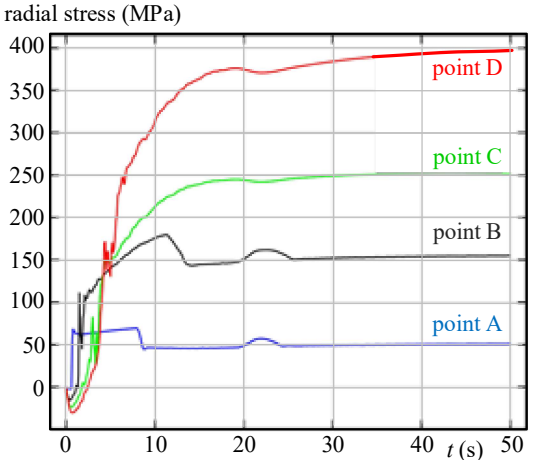

Figure 4.12: Time evolution of radial stress at points A, B, C, and D

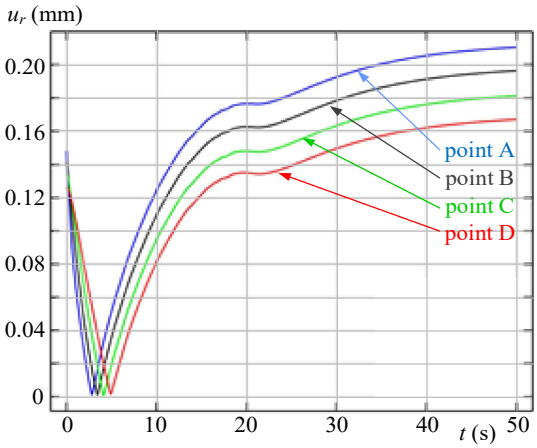

Figure 4.13: Time evolution of radial deformations at points A, B, C, and D

Understanding the distribution of strains and stresses within hardened layers is crucial to assessing the risk of cracks and other damage, particularly in critical components used in machinery, automotive, or aerospace industries. Figure 4.12 illustrates the temporal evolution of the radial component of mechanical stress within the material during the cooling process at all testing points A, B, C, and D. Higher stress values are observed in deeper layers of the cylinder.

Figure 4.13 shows the time evolution of the radial displacements during the cooling process at points A, B, C, and D. The highest values (at point A) reach about 0.2 mm. The dimensions of

the cylinder shrink. I noticed that the radial displacement ((u_r) on the graph is non-zero at the start of quenching. This is because quenching immediately follows heating, causing a non-zero displacement (u_r) at the onset of quenching. Essentially, this displacement results from the prior austenite transformation during heating, with no time gap between heating and quenching.

For an accurate computation of thermal stress and strain, it is crucial to parallel track the entire sequence of phase transformations alongside the temperature evolution. In isotropic materials, both temperature variations and transformations induce a uniform volume change in an expansible body. Therefore, predicting residual stress and strain begins by tracing the thermal history of the workpiece during quenching. The temperature distribution within the quenched part is affected by the intensity of the quenching process. Faster cooling rates result in a steeper temperature gradient, leading to increased thermal strain within the object. The formation of thermal stresses at various temperatures depends on the degree of strain and, in cases of plastic deformation, on the flow stress at that temperature. Figure 4.14 shows the temperature dependent transformation behaviour until it reaches the M_s temperature (temperature of starting the martensitic transformation), but it shifts from the stress-induced to the strain-induced at the M_s temperature.

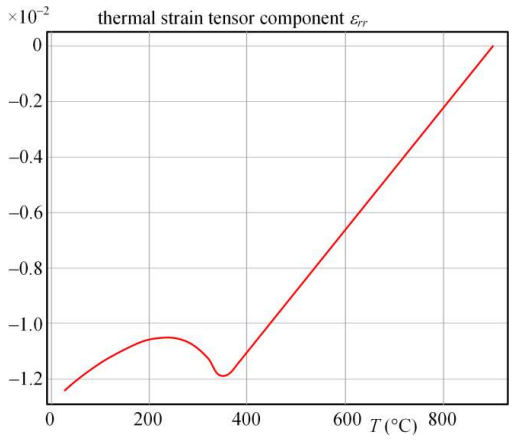

Figure 4.14: Radial component of the thermal strain tensor vs temperature (Point A)

Initially, the surface cooled more rapidly than the centre, resulting in tensile stress on the surface and balanced compressive stress on the centre. As the temperature gradient increased, both the surface and the centre experienced plastic flow when the stress level reached the flow stress of the material. When the cooling rate in the centre exceeded that of the surface, the surface tensile stress unloaded, leading to stress reversal. At the same time, the centre underwent simultaneous

unloading and subsequent reversal of compressive stress. As the surface cooled to the M_s temperature, martensite transformation began, causing expansion in that region.

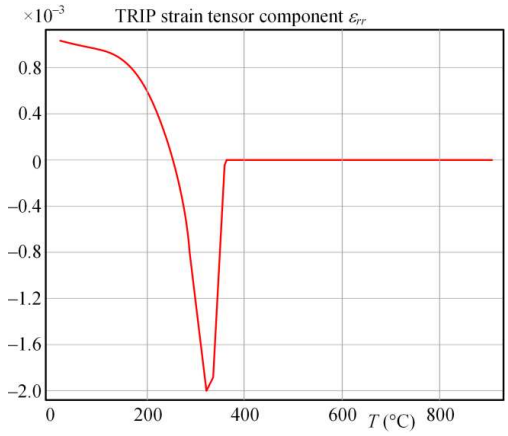

Figure 4.15: Radial component of the TRIP strain tensor vs temperature (point A)

However, in the $140°C$ temperature range just below Ms, transformation plasticity strain predominated, limiting further compressive stress development. The martensite transformation involves a plastic deformation that necessitates the shifting of the entire interface. The obstacle to this movement is called frictional work, which is enhanced by strengthening the solid solution of alloying elements.

Below the M_s temperature, the martensitic transformation is classified as stress-assisted because transformation causes nucleation on preexisting sites such as dislocations, grain boundaries, and phase boundaries. Figure 4.15 shows the temperature at which the TRIP strain can be related to the martensitic transformation. Above the M_s, the TRIP strain remains constant while the applied stress thermodynamically assists to the transformation below the M_s temperature.

Chapter 5

Model calibration of the induction hardening process for gearwheels

5.1 Introduction

The process of hardening gear wheels demands a high degree of precision, relying on the application of an effective mathematical model to adjust input parameters for heating and subsequent cooling, ensuring the desired outcomes are achieved (Barglik et al., 2014, 2021b; Semenov et al., 2014). These input parameters typically encompass factors such as the shape of the inductor, the amplitude, and current frequency (which may require modification during heating), the material chemical composition, its prior microstructure, and the chosen cooling method. The desired output involves achieving a specified distribution of hardness and microstructure within the surface layers of the tooth, often accompanied by the evaluation of the overall efficiency of the system.

Due to the inherent uncertainties associated with certain input variables, particularly the physical properties of materials and factors such as emissivity or convective heat transfer coefficients, it becomes essential to calibrate the process model accurately. This calibration process relies on gathering a substantial amount of experimental data to refine the accuracy and ensure its alignment with real-world conditions. Consequently, calibration serves as a crucial preparatory step for subsequent optimisation procedures or the development of a digital twin for the process. Taking into account the significant investment of time and resources required for extensive experimentation in this domain, effective calibration minimises costs and maximises efficiency.

From the mathematical viewpoint, induction hardening represents a coupled task characterised by a strongly nonlinear interaction of magnetic and temperature fields, which is accompanied by metallurgical and chemical changes in the structure of the processed material (Asadzadeh et al., 2019; Le et al., 2022; Naar & Bay, 2013). The hardening arrangement is mostly 3D and solution of the full forward model is long (many hours or even days), while the solution of the backward model (optimisation) is practically unfeasible.

Gear wheels pose a unique challenge because of their irregular shapes, which requires careful management of heat distribution to achieve the desired depth within a reasonable time frame. Induction surface hardening (ISH) offers an innovative solution for gear wheels, allowing for the creation of a thin, hardened layer across their entire working surface. This results in a hardened microstructure in the contour zone and a less hard microstructure in the transition zone (Rudnev et al., 2014). Importantly, the microstructure within the internal portion of the gear wheel remains practically unaffected (Barglik et al., 2014).

The inductor material used in the current model is copper wire, known for its high electrical conductivity $5.998 \times 10^7\ Sm^{-1}$. Using a formula $R = \rho l/A$, coil resistance of 0.290 mΩ was obtained, where ρ is the resistivity of the material, l and A are length and cross-sectional area of the coil respectively. The inductance of 7.9173 nH was observed from the simulation. To optimise performance and safety, a long bus bar was chosen. Using long busbar offers several advantages, including efficient heat absorption during operation, effective transmission and distribution of electricity, and a reduction in energy loss (total loss, $Q_{rh} = 185.6$ W). Furthermore, the use of a long busbar results in a lower electromagnetic field, which ensures safety, ease of use, and efficient current distribution.

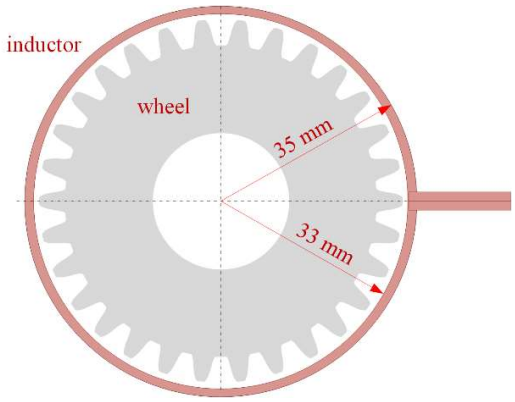

Figure 5.1: Principal dimensions of the inductor

For larger gear wheels, achieving the desired temperature distribution during induction surface hardening (ISH) can be easily achieved with the tooth-by-tooth induction heating (TTIH) method (Barglik et al., 2014; Lupi, 2017). However, for smaller gear wheels, this approach is not feasible, making it difficult to achieve a uniformly thick hardened contour zone across the entire surface of the tooth using TTIH methods.

During the induction heating process, the desired temperature distribution can typically be achieved in one or two cycles. In a single-cycle heating process, single frequency induction hardening (SFIH) or, more commonly, simultaneous dual frequency induction hardening (SDFIH) is used, employing both medium-frequency (MF) and high frequency (HF) (Cha et al., 2020; Pleshivtseva et al., 2019; Szychta & Szychta, 2020). The two-cycle process involves initial MF induction heating, followed by immediate shifting of the body between inductors, and then finally with HF induction heating.

In this model, SFIH is used, with a focus on enhancing its efficiency through the implementation of innovative ideas, defining the objective function discussed in Section 5.4. Initially, the process is calibrated to meet the objectives defined in the function using the commercial software COMSOL Multiphysics 6.0. This involves understanding the combination of parameters required to achieve the desired hardness. This calibration is conducted through low-computing sweep analysis. The second step involves detailed modelling to provide a visual representation of the actual process. Finally, the obtained optimised parameters are implemented in practical applications.

The task was to calibrate and optimize the hardening gear wheels manufactured of AISI 4340. The chemical composition of this material was given in (Table 3.1). This examined steel, AISI 4340, is classified as a medium alloy steel, with its primary alloying elements being nickel (Ni), chromium (Cr), molybdenum (Mo) and vanadium (V). Its mechanical properties and high strength make it a part of special high-strength steels, commonly used in the production of military equipment. In particular, it finds extensive application in tank barrels and other heavily stressed components due to its notable resistance to material fatigue (Eckert et al., 2020). The basic dimensions of the wheel are shown in Figure 5.2.

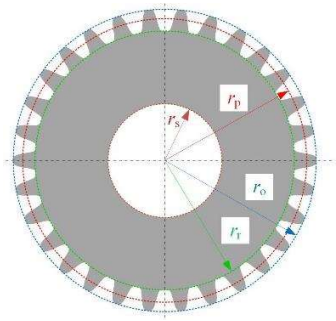

Number of teeth, N: 30

Radius of shaft, r_s: 12 mm

Root radius, r_r: 27.5 mm

Pitch circle radius, r_p: 30 mm

Outer radius, r_0: 32 mm

Thickness of wheel, t: 7.5 mm

Figure 5.2: Basic dimensions of gearwheel

5.2 Induction surface hardening model

Induction heating differs significantly from classical hardening methods due to its short duration (Barglik, 2016). It starts at the lower critical temperature Ac_1 and progresses until the material reaches the upper critical temperature Ac_3, resulting in an austenite microstructure. However, this microstructure is nonuniform. The critical temperatures that govern the transformation from any previous microstructure to a uniform austenite microstructure depend on the rate of induction heating.

CCT diagram is a crucial basis for making an optimal heat treatment process for steels with required microstructure and properties. The diagram provides insight into the hardening behaviour of steels and the process of austenite transformation at different cooling rates. Hence, a rapid and precise prediction of the CCT diagram has significant practical value. The configuration and placement of the diagram are predominantly influenced by factors such as the chemical composition of the steel, the size of its austenite grains, as well as the temperature and duration of the austenitizing process. For the analysed problem of medium-frequency induction hardening, the heating rate reaches values of 100 K/s or less. Therefore, such a simplification can be accepted. Also, when cooling starts, the temperature distribution in the volume of the tooth is not uniform.

Currently, three main methods are employed to determine the CCT diagram. The first method uses traditional experimental techniques, such as metallography hardness testing and dilatometry. The second method relies on empirical formulas or mathematical models to calculate transition points of time and temperature, which are then used to construct the CCT diagram by connecting these points (Ollat et al., 2018; Pohjonen et al., 2018). This method has been incorporated into commercial software like JMatPro, allowing for the calculation of ferrite, pearlite, and bainite transformations in high-strength low-alloy (HSLA) steel, as well as the conversion of TTT diagrams to CCT diagrams using Scheil's addition rule (Saunders et al., 2004). Thus, JMatPro can compute TTT and CCT diagrams for steel by entering parameters such as composition, austenite temperature, and crystal size. The third method involves the emerging approach of machine learning to predict nonlinear curves (Trzaska & Jagie, 2009).

The full model described in Equations (5.2) and (5.5) is formally correct. However, certain coefficients in these equations, such as those related to temperature dependence, and the physical parameters including dependence of magnetic permeability on temperature and magnetic flux

density $\boldsymbol{B}$, or coefficients α and C in the boundary conditions include some uncertainties. Therefore, the model has to be calibrated to provide the correct values.

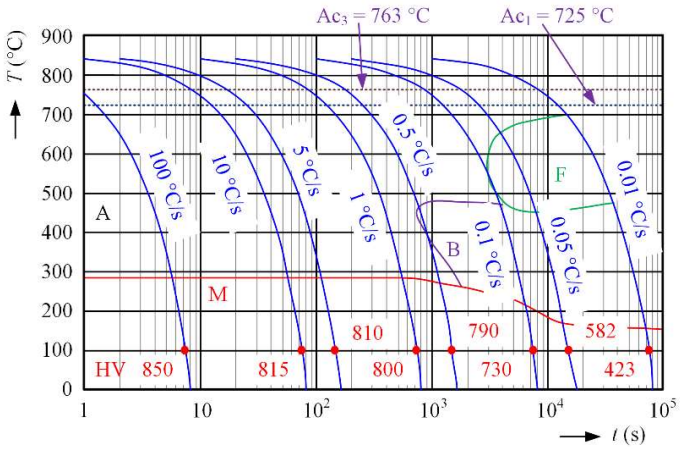

Figure 5.3: CCT diagram of material AISI 4340

5.3 Simplified model and its processing

The simplified model is used to build on a thorough investigation of the full model and sensitivity analysis. First, suppose that the temperature Ac_3 when the structure of the steel becomes a perfect austenite solution does not depend on the rate of heating and its CCT diagram does not depend on it either. The description of chemical changes in the material structure is only qualitative (which means that all these levels are supposed to have the same temperature dependencies on the corresponding physical parameters). The procedure of cooling of the heated teeth that is realised by spraying a suitable quenchant is described using a constant or linearly dependent coefficient of convection that must agree with the real time of cooling. Here, the coefficient of convective heat transfer is extremely difficult to determine, and this fact belongs to one of the serious reasons why the model must be calibrated.

The results of the model are then compared with the data captured experimentally in the transverse cut through the tooth, namely the hardness at selected points of the material (both on the surface and at selected points of its internal layers). This comparison will then allow for calibrating the simplified model so that it provides acceptable results not only for the arrangement under investigation but also for several similar arrangements. For further verification and increased reliability, the model must be tested for several more sets of points. In the case of optimising the whole process from the viewpoint of the power balance (or efficiency), the parameters of the field

current (amplitude, frequency and time evolution) are also of great importance. The model is then expected to be valid for a number of similar arrangements.

The calibration itself is performed automatically using suitable optimisation techniques. Based on experience in simulations and experiments, only the key parameters of the model are selected using the sensitivity analysis. Here, the material characteristics of the gearwheel (including their temperature dependencies) are sufficiently known and accurate, so the focus is mainly on the convective coefficients in the course of heating and cooling, respectively. Consider, optimising the convective coefficient, which is modelled as a linearly decreasing function. Its starting point and eventual slope are subject to optimisation. Although a constant value may suffice, the decreasing function better reflects reality, as indicated by several numerical experiments.

Regarding the optimisation of the field current, two frequencies are commonly employed: a low frequency for fundamental heating and a high frequency for finishing. However, since the frequencies of the converter can only vary within a narrow range, it is often adequate to optimise its amplitude. However, even within this narrower frequency band, a sweep analysis can be conducted to determine the optimal value.

5.4 Mathematical model of the process

Numerical simulations play a vital role in engineering design and optimisation, allowing researchers to study and replicate real-world physical systems. With advances in computational power and simulation software, these models can now capture increasingly intricate details of real systems, minimising the gap between the physical and simulated world. However, performing high-fidelity simulations remains a time-consuming task, largely due to the growing complexity of simulation models. This complexity includes factors such as the incorporation of more solving equations and finer meshing, etc. The direct application of these time-consuming simulation models to optimisation problems may lead to unaffordable design costs. Mathematical and surrogate models are essential prerequisites before optimisation, involving the utilisation of available input parameter values and their corresponding output performance or quantities of interest (QOIs) to provide predictions.

The mathematical description of the process comprises two models: the forward model, which characterises the induction hardening itself, and the backward model, tasked with proposing

a surrogate model of the process and optimising the input parameters to achieve optimal design outcomes. The use of surrogate models in engineering design and optimisation involves two key steps: constructing accurate surrogate models and applying them to diverse optimisation problems. Construction involves data collection, model selection, and accuracy validation. The application involves integrating surrogate models into optimisation algorithms to efficiently explore design spaces and identify optimal solutions.

5.4.1 Forward problem

The forward mathematical model of the process is fully described by two partial differential equations describing the time evolution of magnetic and temperature fields in the system. The magnetic field obeys the equation for magnetic vector potential $\boldsymbol{A}$ in the form (Balanis, 2012; Mosayebidorcheh et al., 2014).

$$curl\ \left(\frac{1}{\mu} curl\ \boldsymbol{A}\right) + \gamma \frac{\partial A}{\partial t} = \boldsymbol{J}_{s.} \tag{5.1}$$

Here, μ denotes the magnetic permeability, γ is the electric conductivity, t stands for time and $\boldsymbol{J}_s$ represents the current density delivered to the inductor from the source. However, the numerical solution to this equation in a generally 3D arrangement would be extremely demanding. That is why the equation was slightly simplified assuming that in every cell of the discretization mesh the magnetic permeability is constant, so that all field quantities are harmonic. Then, equation (5.1) can be modified (using the phasors) as follows:

$$curl\left(curl\ \underline{\boldsymbol{A}}\right) + j \cdot \gamma\omega\mu\underline{\boldsymbol{A}} = \mu\underline{\boldsymbol{J}}_s, \tag{5.2}$$

where ω is the angular frequency. Although the magnetic permeability in every cell of the mesh is constant, its values generally differ from cell to cell because they are determined from the actual value of the magnetic flux density. The boundary condition along a sufficiently distant artificial boundary is of Dirichlet type.

The harmonic magnetic field in the system inductor-hardened gear wheel produces induced currents of local densities.

$$\underline{\boldsymbol{J}}_i = -j \cdot \gamma\omega\underline{\ } \tag{5.3}$$

that are sources of specific Joule losses, whose value is

$$w_J = \frac{1}{2} \cdot \frac{|\underline{J}_i|^2}{\gamma} \tag{5.4}$$

Further losses that may contribute are the magnetisation losses, but their magnitude is small compared with the above Joule losses and may be neglected.

The temperature field T in the system is described by the heat transfer equation in the form (De Flaviis et al., 1998).

$$\nabla \cdot (k \nabla T) = \rho c_p \frac{\partial T}{\partial t} - w_J, \tag{5.5}$$

where λ is the thermal conductivity, ρ stands for the specific mass and symbol c_p represents the specific heat capacity at a constant pressure. As for the quantity w_J, it is nonzero in the case of heating; in the case of cooling, it vanishes. The boundary condition along the external surface of the wheel can be written in the form

$$-k \frac{\partial T_s}{\partial n} = \alpha (T_s - T_0) + \sigma C (T_s^4 - T_r^4). \tag{5.6}$$

Here, T_s is the temperature of surface of the workpiece, α is the coefficient of convective heat transfer, T_0 denotes the temperature of the surrounding medium (air), $\sigma = 5.67 \times 10^{-8}\ \mathrm{W/m^2K^4}$ is the Stefan-Boltzmann constant, C stands for the emissivity of the heated body and T_r is the temperature of the surface to which the heat is radiated and all are nonlinear functions of the temperature.

5.4.2 Backward problem

The backward problem consists of the proposal of the surrogate model. It is a simple model of the hardness that is supposed to be a function of the important input parameters (usually containing polynomial or power expressions) whose coefficients are determined from several results calculated from the full model of the process at suitably selected points of the design space. After completing this simplified model, it is necessary to test it for a sufficient number of further points in this space. Provided that the results are in the prescribed tolerance zone, the model can be considered correct. If not, it has to be redesigned, considering the unsatisfactory results.

In the next step, it is necessary to propose one or more objective functions that have to be extreme in agreement with the requirements. Extremisation is achieved by a relevant optimisation scheme, using a suitable deterministic algorithm. The optimisation scheme described in Figure 5.4.

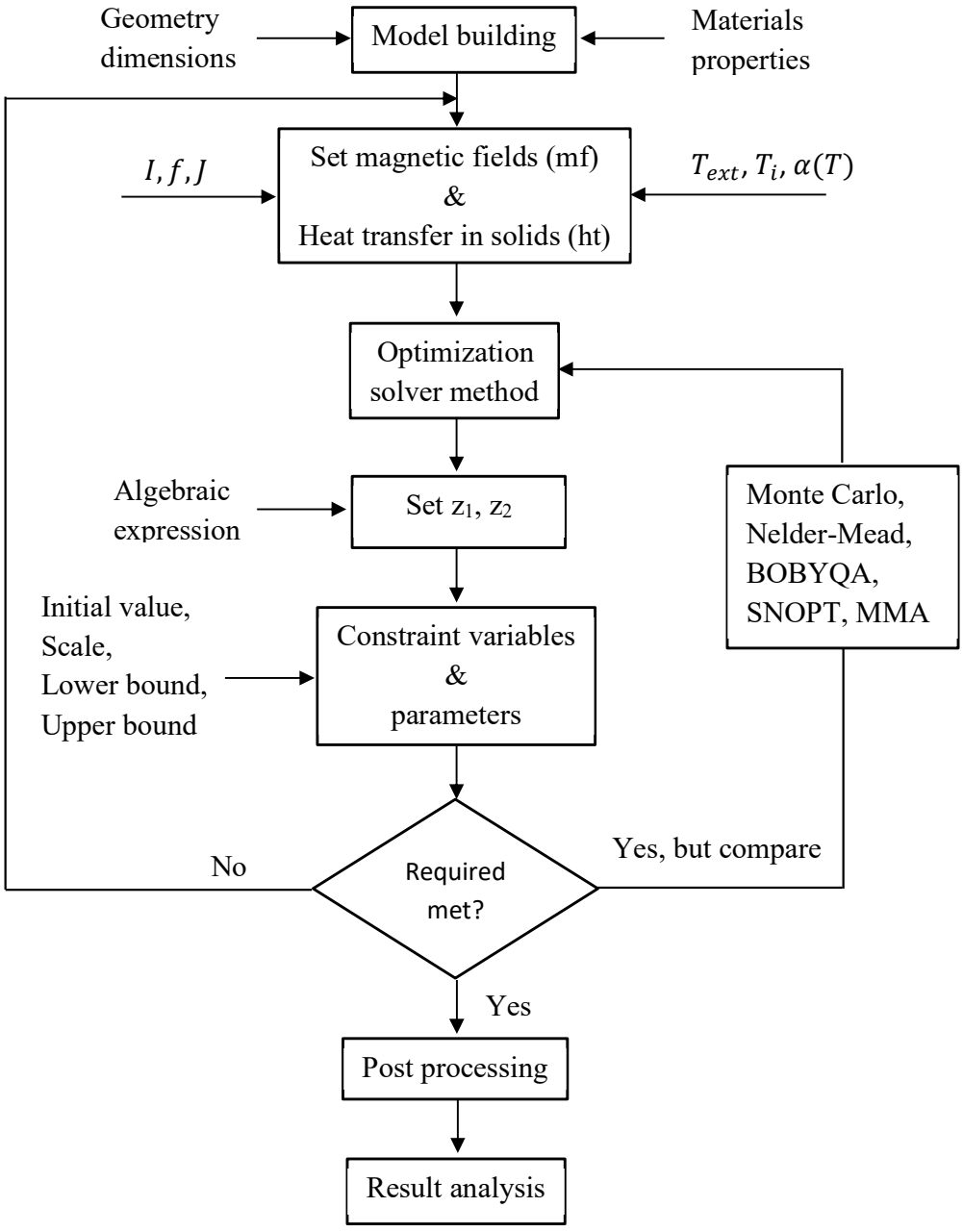

Figure 5.4: Model optimisation scheme

Given that many engineering design challenges involve time-intensive simulations and analyses, surrogate models are frequently used for rapid calculations, sensitivity analysis, and exploration of the design space, ultimately helping to achieve optimal designs. One common approach is to construct surrogate models for objective functions and constraints that are computationally expensive. The accuracy of the final optimal solution depends on the precision of

these surrogate models. Since the optimal solution to the original problem is typically unknown beforehand, designers must ensure that each surrogate model maintains high predictive accuracy throughout the design space. This ensures that the resulting optimal solution closely approximates the true optimal solution to the original problem. The details of the process will be provided below.

5.5 Material characteristics as a function of temperature

Thermal characteristics are linked to how materials respond to temperature changes, affecting various properties such as physical, chemical, mechanical, electrical, magnetic, and optical behaviours.

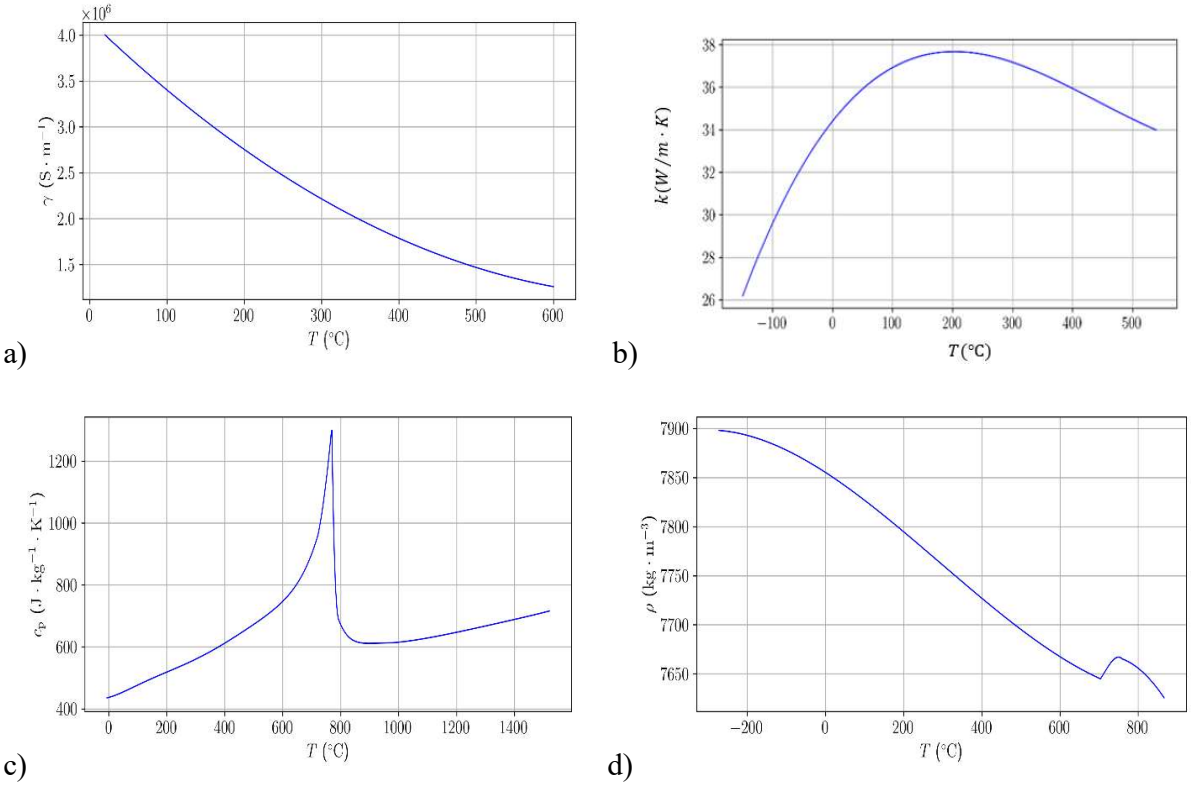

Figure 5.5: Temperature-dependent characteristics of steel AISI 4340. 5.5a: electrical conductivity γ, 5.5b: thermal conductivity k, 5.5c: specific heat capacity c_p, and 5.5d: specific mass ρ

Although most metal materials exhibit temperature-dependent characteristics, some withstand extreme heat. Key thermal characteristics in engineering include heat capacity, thermal conductivity, thermal expansion, electrical conductivity, and weldability.

The magnetisation characteristic of AISI 4340 steel at room temperature is shown in Figure 5.6.

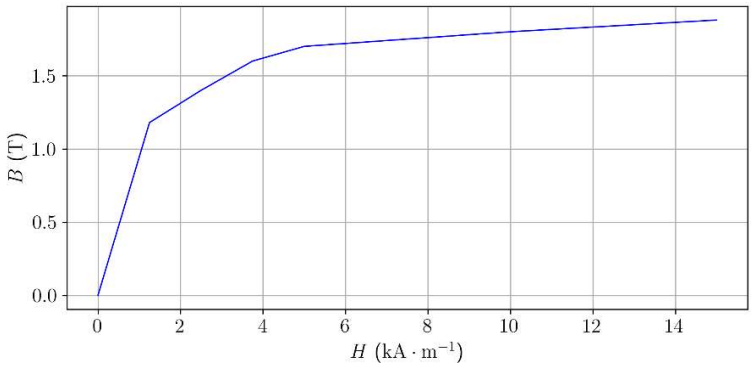

Figure 5.6: Magnetisation curve of steel AISI 4340 at room temperature

The magnetisation characteristic is also a function of the temperature T. Unfortunately, this dependence was not available, but its suggested approximation in the form

$$\mu_r(B,T) = \mu_r(B,T_0) \cdot \Psi(T), \tag{5.7}$$

where T_0 is the room temperature and $\Psi(T)$ is a suitable temperature function. After some experiments, the accepted function can be written as

$$\Psi(T) = a - bT^2 \text{ for } T_0 \leq T \leq T_C. \tag{5.8}$$

The constants a and b are given by the formulae

$$a = \frac{\mu_r(B,T_0) \cdot T_C^2 - T_0^2}{\mu_r(B,T_0)(T_C^2 - T_0^2)}, \tag{5.9}$$

$$b = \frac{\mu_r(B,T_0) - 1}{\mu_r(B,T_0)(T_C^2 - T_0^2)}, \tag{5.10}$$

$$\Psi(T) = \frac{1}{\mu_r(B,T_0)} \text{ for } T \geq T_C. \tag{5.11}$$

Here T_C is the Curie temperature.

5.6 Calibration and optimal model of the gear wheels

Model simulation helps predict system performance, allowing exploration of the design space and the search for an optimal design. Model calibration involves the precise adjustment and simulation of the induction hardening process applied to gear wheels. Calibration ensures that the parameters of the hardening process, such as power settings, frequency, and duration, are accurately set to

achieve the desired hardness and mechanical properties in the gearwheels. Optimal modelling involves creating computational simulations or mathematical models to predict how the induction hardening process will affect the material properties, allowing for optimisation and fine-tuning before actual implementation. The overall process aims to improve the efficiency, durability, and performance of the gear wheels through advanced engineering techniques.

5.6.1 Model calibration

The task to be solved was to find the input parameters (amplitude and frequency of the current) that would provide the distribution of temperature in the region of teeth such that the temperature of the top land exceeds the value Ac_3 (which is higher than Ac_3 denoted in Figure 5.3 due to high rate of heating) and should be well hardened, while the temperature inside the tooth at the base diameter should not exceed about 800 °C, so that the material there remains tenacious.

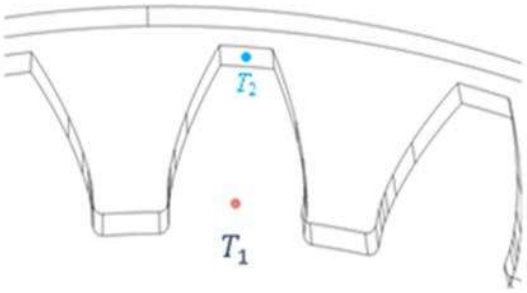

Figure 5.7: Data point location in gear tooth

The objective functions aim to maximize the temperature difference $T_2 - T_1$, as described in equation (5.12), by selecting two specific points were introduced in the form

$$z_1 = \min 1/(T_2 - T_1)^2, \tag{5.12}$$

$$z_2 = \min(T_1 - 800), \tag{5.13}$$

where temperatures T_2 and T_1 are functions of the amplitude I and frequency f of the field current, time of heating t_h and coefficient α of the convective heat transfer. The constraints are the following:

$$I \in \langle 200, 1000 \rangle \text{A}, f \in \langle 10, 50 \rangle \text{kHz}, \alpha \in \langle 4, 20 \rangle \text{W}/m^2\text{K},$$

while the heating process of heating stops when $T_2 > 1000$ ℃

The calculations were performed using the commercial software COMSOL Multiphysics 6.0 and SolidWorks to construct geometry. For the forward problem, the number of DOFs was about 700,000, and evaluation of one variant took about three hours on a top-parameter personal computer. An effective approach to striking a balance between accuracy and efficiency is through the adoption of multifidelity surrogate models. These techniques play a crucial role in supporting engineering design and optimisation. During the computations, attention was paid to the position of the artificial boundary and discretisation of the area with respect to the convergence of the numerical results. The required precision was established in the first three digits.

Figures 5.8 show the current distributions in the centre line of the top land for different values of I and f after the specified time of heating t_h, the coefficient α being 10 $\mathrm{W}/m^2\mathrm{K}$.

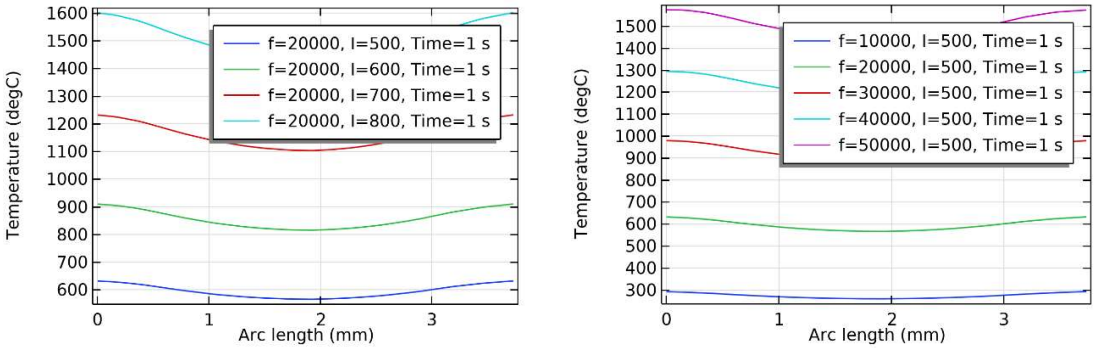

Figure 5.8: The dependencies of the temperature in the top of the centre line of the tooth are based on the frequency and amplitude of field current for $t_h = 1s$.

From Figure 5.8 (left), it can be seen that for frequency 20 kHz the current I about 680 A is enough to reach the temperature $1000\ °C$ across the whole top land, while for the current $I = 500\ A$ it is necessary to use frequency about 38 kHz to reach the same results as shown in Figure 5.8(right).

Figure 5.9 shows the results of the sensitivity analysis, specifically illustrating how the heating time t_h varies with different values of I and f. Here, the coefficient α being 10 $\mathrm{W}/m^2\mathrm{K}$.

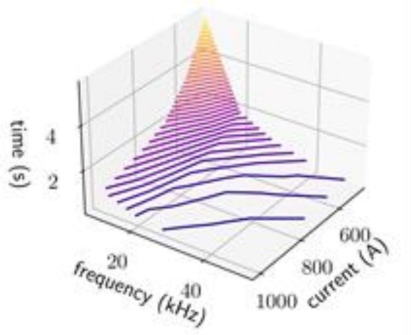

Figure 5.9: Effect of heating t_h duration on the values of I and f for $\alpha = 10\,\mathrm{W/m^2K}$.

5.6.2 Optimal model of the process

The field of optimisation focuses on quantitative modelling processes and the determination of the best decisions within the confines of these models. Every optimisation problem consists of three key elements: an objective function, decision variables, and constraints. Formulating an optimisation problem involves translating real-world challenges into mathematical equations and variables that represent these components.

Optimisation was performed by several techniques; the best results were obtained using the Nelder–Mead and BOBYQA algorithms. To avoid a poor-quality model, it is common practice to construct multiple surrogate models based on input and output data from simulations, assess their accuracy, and then select the one with the highest quality.

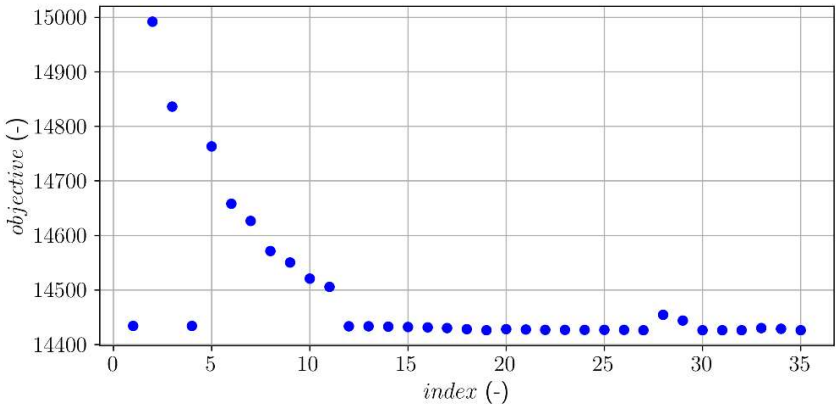

Figure 5.10: Dependence of the sum of both objective functions on the number of iteration steps (Nelder-Mead algorithm) (Barglik et al., 2023).

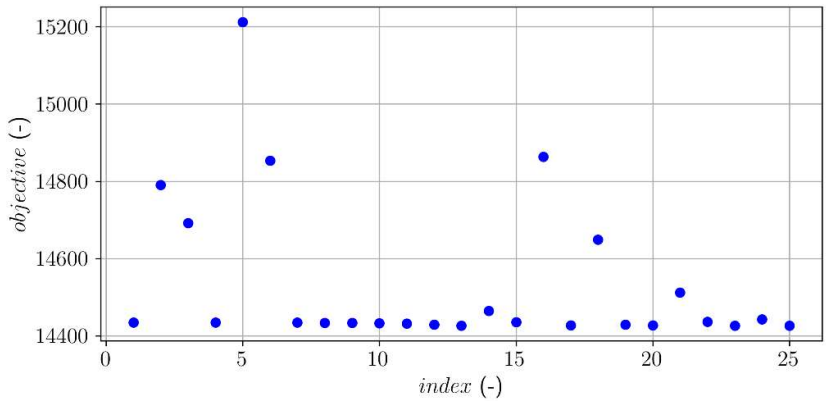

Figure 5.11: Dependence of the sum of both objective functions on the number of iteration steps (BOBYQA algorithm) (Barglik et al., 2023).

Figures 5.10 and 5.11 show the convergence of the sum of both objective functions obtained by the particular algorithms. The process converged after about 25 iteration steps.

The quality of the model significantly affects both the computational cost and the convergence characteristics in the optimisation process. An alternative approach to mitigate these limitations and improve predictive accuracy is to create an ensemble by combining individual models. Both figures show that the results (sum of the minima of the objective functions) are practically the same. But, since this sum is a slightly wavy function with a considerable number of extremes, the input parameters for both optimisation processes are somewhat different. Particularly:

Nelder–Mead: $I = 230$ A, $f = 10.5$ kHz, $\alpha = 10.9$ W/m^{2}K

BOBYQA: $I = 280$ A, $f = 10$ kHz, $\alpha = 10$ W/m^{2}K

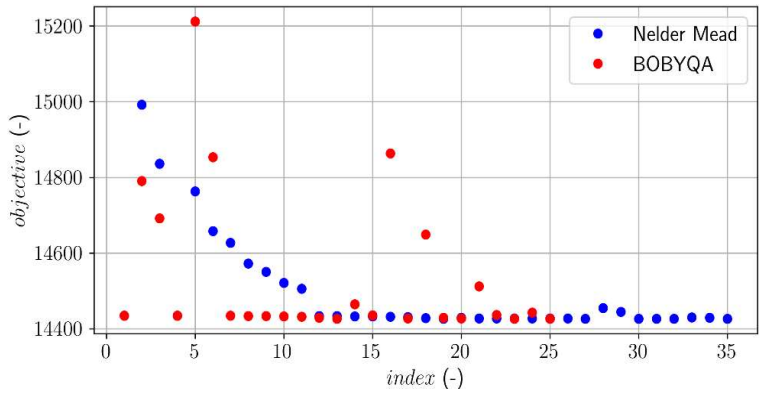

Figure 5.12: Comparison of algorithms

Chapter 6

Analysis of thermoelastic-plastic properties including TRIP strain

6.1 Introduction

Thermoelastic-plastic properties refer to the behaviour of materials under the combined influence of thermal effects (temperature changes) and mechanical loads, specifically focussing on the transition from purely elastic behaviour to plastic deformation. The idealised elastoplastic behaviour of a material during uniaxial loading is characterised by linearity in stress up to the initiation of yield stress, σ_y with a stress-strain slope equal to the elastic modulus E. As the stress increases beyond the yield point, the material behaviour transitions, and the slope changes to the elastoplastic tangent modulus, E^{ep} (Porter et al., 2009).

The impact of thermal input on a stress field within a solid can be viewed as influencing three main aspects: (1) thermal stress induced by dilatation, (2) change in material properties, and (3) change in the yield surface when the solid undergoes loading beyond its elastic limit.

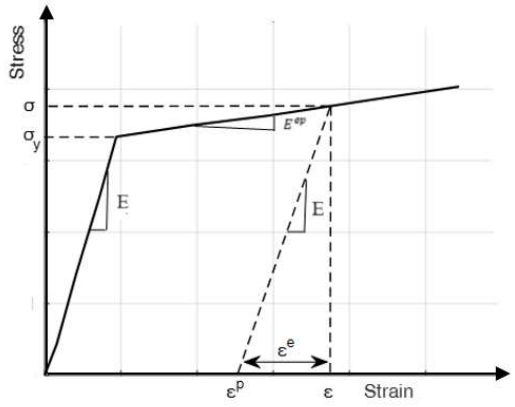

Figure 6.1: Ideal elastoplastic behaviour of material during a uniaxial loading

During the unloading process, the material follows an elastic path with a slope of E. However, it has not returned to its initial state. Residual strain, ε^p, is induced that has same slope E as loading. Total strain can be decomposed additively into two parts: elastic and plastic strains, Equation (6.6).

Transformation-induced plasticity (TRIP) occurs during phase transformations, typically from austenite to martensite, under certain conditions of mechanical loading and temperature. When these materials undergo deformation, such as during forming processes or in-service loading, the transformation from one crystal structure to another can lead to additional plastic deformation. This additional deformation, known as TRIP strain, enhances the overall ductility and formability of the material while maintaining high strength, making it valuable for applications requiring both strength and toughness. TRIP steels are often used in automotive components, where lightweight materials with high crashworthiness are desired.

Extracting TRIP strain involves capturing additional plastic deformation resulting from thermal and mechanical stresses during cooling. This extraction of total strain through experimental analysis of quenching poses significant challenges. Moreover, this phenomenon can occur even when the locally effective stress is below the yield strength of the softer phase at the current temperature (M. Wang & Huang, 2020; Wang et al., 2016). Modelling these processes requires addressing inherent complexities such as phase transformations, significant variations in material properties, and diverse boundary conditions (Barglik, 2018). An accurate assessment of the TRIP strain is crucial for predicting the final residual stresses. Computer simulation emerges as an unparalleled tool for effectively predicting and illustrating the fundamental mechanisms of stress development and the distribution of residual stresses during the induction hardening process (Montalvo-Urquizo et al., 2013; Şimşir & Gür, 2008b).

The Finite Element Method (FEM) plays a crucial role in addressing the challenges associated with extracting TRIP strain and enabling the prediction of multiple concurrent physical phenomena. These include forecasting the temperature history, phase evolution, and internal stresses during quenching processes. Additionally, the interaction between applied load and the stresses required to accommodate the inherent strain of a transformation leads to an irreversible strain during uniaxial loading (Fischer et al., 2000a). Such a plasticity arising from phase transformation occurs as the softer phase undergoes plastic deformation to equalise internal stresses between the parent and product phases. Detailed discussions on the attributes of transformation plasticity and thermomechanical simulation can be found in (Inoue, 2011).

Due to a limited coupling of the model (non-strong coupling), thermal and metallurgical simulations, along with their results, are independent of the mechanical constitutive laws. The constitutive laws are the same for both thermal and metallurgical models. Details of the elastic-

viscoplastic constitutive laws under thermomechanical solidification were discussed in (Fischer et al., 2000a; Inoue, 2011).

Greenwood and Johnson made the first groundbreaking efforts to elucidate the TRIP strain in 1965 (Taleb & Sidoroff, 2003). A researcher (Zhong et al., 2020) highlighted the role of transformation plasticity in the management of internal stress during martensitic transformation, using the transformation plasticity coefficient (K). However, their study did not explore changes in mechanical properties when TRIP strain is not considered. The TRIP strain significantly influences the distortions and residual stresses of the components (Afzal & Buhl, 2022; Behrens et al., 2022; Wang et al., 2016). A recent study by (Kaiser et al., 2020) reported the impact of the TRIP effect induced by carbide precipitation during the tempering of AISI 4140 steels. They compared residual tensile stresses on the surface with and without TRIP, finding that in the absence of TRIP, the plastic compression in the surface zone is significantly reduced. The conclusion is that TRIP must be considered for the simulation of surface hardening.

Researchers have developed various methods to predict the accurate temperature distribution, phase transformation, and mechanical properties of quenched steel. For example, in the study (Kianezhad et al., 2015), the authors used quenching factor analysis (QFA) and artificial neural network (ANN) approaches to predict the hardness of the quenched steel. Other researchers (Carlone et al., 2010, 2010; Chen et al., 2019b) used FE model-based analysis and (Ariza et al., 2014; Zhong et al., 2020; Zhu et al., 2013) used numerical simulation-based analysis to obtain accurate prediction of mechanical properties in quenched steel. However, in most of these studies, the complexity of the quenching process is indicated to determine the temperature distribution, phase transformation, and mechanical properties. They concluded that more work is necessary to fully understand and address these complexities.

In this work, FEA was utilised to examine the proposed models, accounting for the influence of coupled thermal, metallurgical, and mechanical phenomena during quenching operations. These models were integrated into COMSOL Multiphysics, where numerical simulations were conducted. The results suggest that by assigning suitable behaviours to each stage, particularly by leveraging the elastic-viscoplastic properties during high-temperature phase changes and considering TRIP strain, more accurate predictions of residual strain and stresses in heat treatment processes can be achieved.

6.2 Deformation in steel materials

Quenching is a process designed to achieve specific material properties in the desired balance between hardness, strength, and other mechanical characteristics. The cooling rate during quenching determines the properties of the material, including density and linear expansion. Higher cooling rates during quenching result in higher material density, whereas slower cooling rates may allow for more relaxed atomic arrangements, potentially resulting in lower density; see Figure 6.2 (right).

The TRIP strain generated during the austenitisation phase has a negligible effect on the final residual stress state. However, the TRIP strain produced during the martensite transformation significantly influences the mechanical properties of the steel. Two key factors are responsible for the irreversible deformation of an iron-based alloy during and after a martensitic phase transformation (Majaty et al., 2018; Nagayama et al., 2001b).

1. The accommodation process, driven by the change in the transformation volume change and the shear stress τ that leads to additional elastic and plastic straining, results in a compatible deformation and strain state. This phenomenon is commonly called the "Greenwood–Johnson" effect.
2. The orientation process is triggered by forming preferred variants that may align themselves in partially self-accommodating groups. This effect is often termed the "Magee" effect.

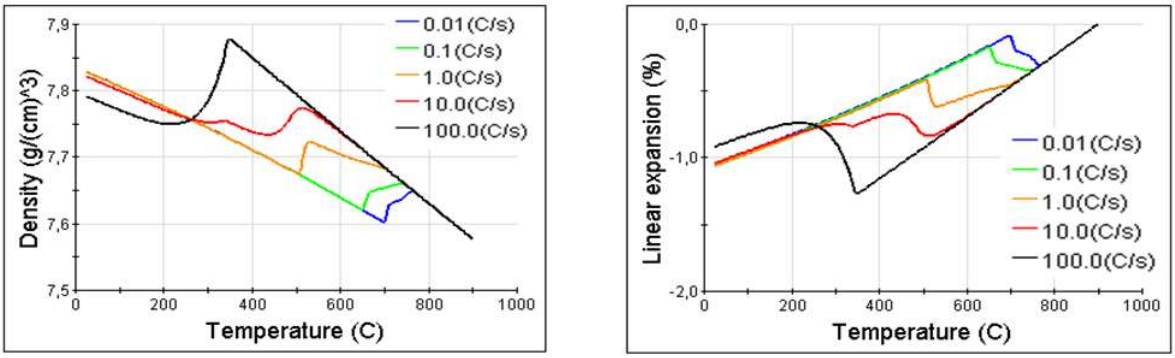

Figure 6.2: Relation of the cooling rate to the density (left) and linear expansion during quenching (right)

Additionally, a higher cooling rate leads to a reduced linear expansion. Rapid cooling suppresses thermal expansion, resulting in a more compact structure and less expansion. On the other hand,

slower cooling rates may allow for more pronounced linear expansion due to thermal effects; see Figure 6.2 (left).

6.3 Phase transformation in quenching

The quenching process is characterised by a significant temperature variation, leading to phase transformations. The phase decomposition of austenite into ferrite, pearlite, or bainite during cooling and its reverse transformation during heating is influenced by diffusion, depending on temperature and time. When the steel is quenched rapidly enough from the austenitic field, there is not sufficient time for eutectoidal diffusion-controlled decomposition processes to occur. As a result, the steel undergoes a transformation into martensite or, in some cases, martensite with a small amount of retained austenite. The transformation of austenite to martensite during cooling and its reversal during heating is characterised by a diffusionless growth process, primarily independent of temperature. Various approaches have been proposed in the literature to model this diffusionless transformation, employing specific techniques to account for the irreversibility of the martensite transformation.

The volume fraction of martensite increases through the gradual transformation of the remaining austenite between the already formed plates. The initial plates start forming at the M_s temperature, which is associated with a specific driving force for the diffusionless transformation of austenite (γ) into martensite (α'). In low-carbon steels, M_s is approximately 500°C, but higher carbon content progressively lower the M_s temperature (Porter et al., 2009). The martensite finish (M_f) temperature is the temperature below which further cooling does not increase the amount of martensite. In practice, M_f might not guarantee 100% martensite, as some retained austenite may persist even below M_f. The retention of austenite in such cases could be attributed to the high elastic stresses between the last martensite plates formed, which hinders further growth or thickening of existing plates. Here, the initial step involves estimating specific levels within the heated steel. During the onset of cooling, it can be possible to assume a perfect austenite solution, i.e., $\xi_A(t_1) = 1$, in the outer layers of the sample. However, determining the initial proportions of austenite, pearlite, ferrite, and bainite in the deeper layers, which are subjected to lower temperatures, can be a challenge. That is why Equation (6.1) is problematic, as the value of $\xi_0(t_1)$ varies from one layer to another. The same holds for Equation (6.2), because in the deeper layers, the fractions of particular levels may be determined only experimentally. It is a question whether

relevant information could be found in the literature or not. That is why the description of both mentioned equations should be discussed in more detail.

Following the previous text (Areitioaurtena et al., 2022)

$$\xi_0(t_1) + \xi_A(t_1) = 1, \tag{6.1}$$

before cooling and after cooling

$$\xi_{\mathrm{A}}(t_2) + \xi_{\mathrm{F/P}}(t_2) + \xi_{\mathrm{B}}(t_2) + \xi_{\mathrm{M}}(t_2) = 1. \tag{6.2}$$

The aspect of deformations is another field that directly affects the mechanical stresses in a material. It is modelled independently of the magnetic field, but the temperature field must be considered. If the phase fraction is denoted as ξ, resulting from the decomposition of isothermal austenite, the JMAK-type equation can be used to determine it (Moumni et al., 2011).

$$\xi = 1 - \exp(-kt^n). \tag{6.3}$$

Here, t represents the total transformation time at a specific temperature, k is the rate constant that depends on both the temperature and the transformation mechanism, and n stands as a constant applicable throughout the temperature range in cases where a singular transformation mechanism is in effect.

In the absence of diffusion during the transformation of austenite to martensite (Martensite transformation), the Koistinen-Marburger model (Koistinen & Marburger, 1959; Moumni et al., 2011) can be used to calculate the volume fraction of martensite (ξ_{M}). The martensitic transformation is exclusively temperature dependent and occurs without diffusion (Chen et al., 2019b; H. Li et al., 2008).

$$\xi_M = 1 - \exp\left[-\alpha(M_s - T)\right] \tag{6.4}$$

Where $\alpha = 1.10 \times 10^{-2}\ \mathrm{K}^{-1}$ is a constant parameter determined through experiment and M_s is the martensite start temperature, T is the temperature in Kelvin to which the material was quenched.

Although the equation of Koistinen and Marburger (the K-M model) (Koistinen & Marburger, 1959), dates to 1959, it continues to be widely utilised to predict the kinetics of martensite. This equation generates a C-curve shape when plotting the martensite volume fraction against the cooling temperature below M_s. However, for most low-alloy steels, the kinetic martensitic transformation curve typically displays a sigmoid shape (Lee & Lee, 2008). To address

these limitations of the K-M model, Lee et al. (Lee & Van Tyne, 2012) introduced a new kinetic model for martensite transformation in low-alloy steels, based on dilatometric analysis.

The thermophysical properties $\rho_m(T, \xi_k)$ of the phase mixture are estimated using the linear rule of mixtures (Samuel & Prabhu, 2022b) in the form

$$\rho_m(T, \xi_k) = \sum_{k=1}^{5} \rho_k \, \xi_k, \tag{6.5}$$

where ρ_k and ξ_k are the measured temperature-dependent density and volume fraction of the k^{th} phase, respectively.

The temperature at which M_s occurs is linked to the arrangement of the nuclei, which might be influenced by the orientation or configuration of the dislocations.

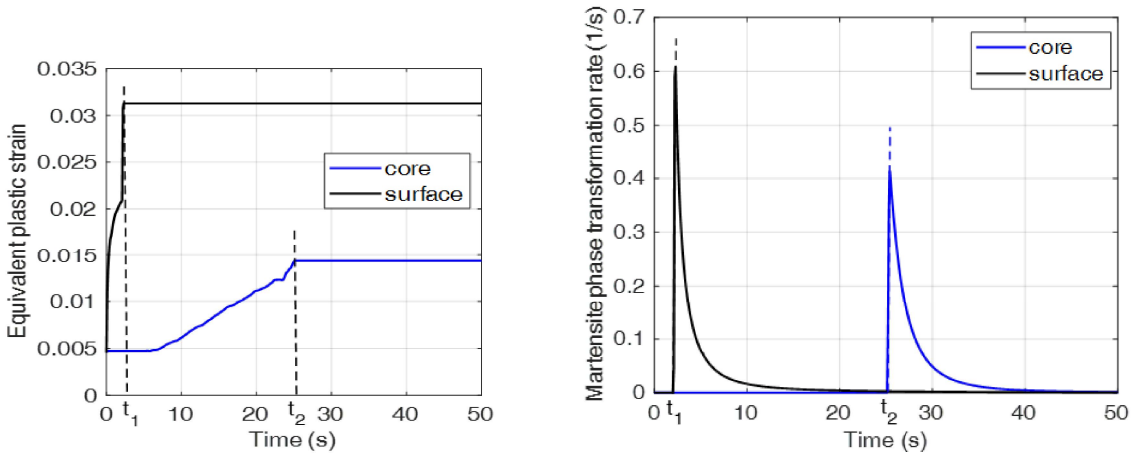

Figure 6.3: Martensite phase transformation rate (1/s) (right) and equivalent plastic strain (right) vs. cooling time (s).

Figure 6.3 (left) shows that the surface and core experience M_s temperature at different times due to variations in cooling rates. The plastic strain observed on the surface developed rapidly, reaching its maximum value at time t_1, followed by a constant value. In contrast, in the core, it grows slowly and reaches its maximum at time t_2.

Figure 6.3 (right) shows that the phase transformation rate is typically expressed as the number of transformations per unit of time, representing the frequency at which phase transformations occur within the material. These transformations involve changes in the arrangement or structure of atoms and are influenced by factors such as temperature or composition. A high transformation

rate is observed on the surface during the initial cooling stages. At the core, no phase transformation rate was observed till t_2.

6.4 Thermal stresses and strain

Thermomechanical analysis serves as a technique in thermal analysis that is used primarily to measure thermal expansion and changes in mechanical properties, such as thermal stress, deformation, and strain. The constitutive equations used to simulate quenching are derived from the additive decomposition of the total strain as elastic and plastic.

$$\varepsilon = \varepsilon^e + \varepsilon^p \tag{6.6}$$

The relationship between stress and strain can be described as follows:

$$\sigma = E\varepsilon^e = E(\varepsilon - \varepsilon^p) \tag{6.7}$$

The uniaxial relation of stress and strain can be generalised using Hooke's law as follows:

$$\sigma_{ij} = E_{ijkl}\varepsilon^e_{kl} = E_{ijkl}\left(\varepsilon_{kl} - \varepsilon^p_{kl}\right), \tag{6.8}$$

where E_{ijkl} is the fourth order elasticity tensor.

Further decomposing into rate form associated with various physical events, more realistic in temperature variation and phase transformations (Samuel & Prabhu, 2022b).

$$\dot{\varepsilon}_{ij} = \dot{\varepsilon}^{\mathrm{e}}_{ij} + \dot{\varepsilon}^{\mathrm{p}}_{ij} + \dot{\varepsilon}^{\mathrm{th}}_{ij} + \dot{\varepsilon}^{\mathrm{tr}}_{ij}, \tag{6.9}$$

where $\dot{\varepsilon}_{ij}, \dot{\varepsilon}^{\mathrm{e}}_{ij}, \dot{\varepsilon}^{\mathrm{p}}_{ij}, \dot{\varepsilon}^{\mathrm{th}}_{ij}$ and $\dot{\varepsilon}^{\mathrm{tr}}_{ij}$ are the total, elastic, plastic, thermal, and transformation-induced plasticity strain rates, respectively.

Using Hook's law and elastic strain rate, the stress rate tensor accounting the TRIP effect can be written as

$$\dot{\sigma}_{ij} = E_{ijkl}\dot{\varepsilon}^e_{kl} = E_{ijkl}\left(\dot{\varepsilon}_{ij} - \dot{\varepsilon}^{\mathrm{p}}_{ij} - \dot{\varepsilon}^{\mathrm{th}}_{ij} - \dot{\varepsilon}^{\mathrm{tr}}_{ij}\right), \tag{6.10}$$

where $\dot{\sigma}_{ij}$ is the objective stress rate tensor, whose elements can be calculated using the following equations (H. Li et al., 2008).

$$\dot{\varepsilon}^{\mathrm{e}}_{ij} = \frac{1+\nu}{E}\dot{\sigma}_{ij} - \frac{\nu}{E}\dot{\sigma}_{ij}\delta_{ij}, \tag{6.11}$$

$$\dot{\varepsilon}_{ij}^{\mathrm{p}} = \mathrm{d}\lambda \cdot \frac{\partial \Phi}{\partial \sigma_{ij}}, \tag{6.12}$$

$$\dot{\varepsilon}_{ij}^{\mathrm{th}} = \alpha \cdot \delta_{ij} \cdot \frac{\mathrm{d}T}{\mathrm{d}t}, \tag{6.13}$$

$$\dot{\varepsilon}_{ij}^{\mathrm{pt}} = \Delta_k \cdot \frac{\mathrm{d}\xi_k}{\mathrm{d}t}, \tag{6.14}$$

$$\dot{\varepsilon}_{ij}^{\mathrm{tr}} = \frac{3}{2} \cdot K_k \cdot (1 - \xi_k) \cdot S_{ij} \cdot \frac{\mathrm{d}\xi_k}{\mathrm{d}t}, \tag{6.15}$$

where ν is Poison's ratio, E is the elastic modulus, $d\lambda$ is the plastic multiplier, α is the thermal expansion coefficient, $\Phi = \sqrt{\frac{2}{3}\sigma'_{ij}\sigma'_{ij}}$ is the equivalent stress, Δ is the structural dilatation due to the phase transformation, K is the TRIP constant, and S_{ij} is the stress deviator.

The deviator of the trace-free part of the stress tensor is defined as follows (Hömberg, 2004b; Taleb & Sidoroff, 2003).

$$\sigma'_{ij} = \sigma - \frac{1}{3}\mathrm{tr}(\sigma) \cdot I, \tag{6.16}$$

where σ'_{ij} is the deviator stress tensor, σ is the applied stress tensor, tr(σ) is the sum of its diagonal elements and I is the identity tensor.

The general governing equations of coupled thermoelasticity can also be expressed in terms of the stress tensor and temperature. In classical linear thermoelasticity theory, the components of the strain tensor are linearly a function of both the components of the stress tensor and those of the strain tensor resulting from temperature changes (Hetnarski & Eslami, 2019).

$$\varepsilon_{ij} = \varepsilon_{ij}^{e} + \varepsilon_{ij}^{T}, \tag{6.17}$$

where ε_{ij}^{e} denotes the elastic strain and ε_{ij}^{T} stands for the thermal strain.

Thermal strain due to temperature change given by

$$\varepsilon_{ij}^{T} = \alpha(T - T_0)\delta_{ij}, \tag{6.18}$$

where α is the coefficient of linear thermal expansion, T_0 and T is the reference and measured temperature respectively.

The elastic strain tensor is linearly proportional to the stress tensor as

$$\varepsilon_{ij}^{e} = \frac{1}{2G}\left(\sigma_{ij} - \frac{\nu}{1+\nu}\sigma_{kk}\delta_{ij}\right). \tag{6.19}$$

The total strain tensor is

$$\varepsilon_{ij} = \frac{1}{2G}\left(\sigma_{ij} - \frac{\nu}{1+\nu}\sigma_{kk}\delta_{ij}\right) + \alpha(T - T_0)\delta_{ij}, \tag{6.20}$$

using the strain-displacement relation

$$\varepsilon_{ij} = \frac{1}{2}\left(u_{i,j} + u_{j,i}\right). \tag{6.21}$$

Solving equation (6.20) for the stress tensor σ_{ij} gives

$$\sigma_{ij} = 2G\left[\varepsilon_{ij} + \frac{\nu}{1-2\nu}\left(\varepsilon_{kk} - \frac{1+\nu}{\nu}\alpha(T - T_0)\right)\delta_{ij}\right]. \tag{6.22}$$

6.5 Finite element model

The FE simulation of the quenching process was used to visualise and investigate the distribution of the temperature, phase fraction, and mechanical characteristics of the quenched steel. The physical model setup and the FE mesh are depicted in Figure 6.3a. The initial temperature of the workpiece and the quenching medium were set at 900 °C and 20 °C, respectively. The model configuration for the interface of study involved solving the physics of heat transfer in solids, solid mechanics, and austenite decomposition. It was accomplished through multiphysics coupling of phase transformation latent heat and phase transformation strain sequentially under a time-dependent solver.

The computations were performed using the commercial software COMSOL Multiphysics 6.0. The phase transformation model is based on the Koistinen-Marburger framework, with a coefficient value $\beta = 0.011$ K^{-1}, and from the source to the destination phase with a coefficient of $K_{s\to d}^{\mathrm{TRIP}} = 5\mathrm{e}^5$ MPa^{-1}. Initially, during quenching, the presence of austenite as the source phase $\xi_0^s = 1$, and martensite as the destination phase $\xi_0^d = 0$, along with zero plastic recovery for the destination phase $\Theta_{s\to d} = 0$.

6.6 Material and methods

6.6.1 Material

A 100 mm long AISI 4140 steel cylinder with a workpiece of 20 mm radius quenched in water, with heat transfer occurring uniformly across its boundary via a temperature-dependent heat transfer coefficient. The density of this steel at room temperature is $7850\ kg/m^3$, and its melting

point is 1416 °C. The heat flux type is convective, employing externally forced convection, and the fluid flows around the cylinder in crossflow. The finite element (FE) code COMSOL Multiphysics was chosen for numerical simulations because of its capacity to handle systems of analytical equations and logical conditions. The chemical composition of the AISIS 4140 steel is given in Table 4.1.

6.6.2 Methods

A 2D axisymmetric model is used to demonstrate the coupled phenomena of austenite decomposition, heat transfer, and solid mechanics. Initially, the workpiece is heated to 900°C, followed by quenching (spray water). During the subsequent cooling phase, austenite undergoes decomposition, transforming into a combination of ferrite, pearlite, bainite, and martensite. Additionally, phase transformation strains arising from thermal expansion and TRIP are computed. This involves coupling a temperature-dependent phase transformation with an elastoplastic transformation to compute stresses resulting from thermal and TRIP strains. Here, the latent heat of the phase transformation and the phase transformation strain are coupled. The solution uses a generic solution for ordinary differential equations (ODE). Physics interphases can solve these aspects collectively in a time-dependent multiphysics interface.

- Heat transfer module -------> heat transfer in solids (ht)
- Structural mechanics module -------> solid mechanics (solid)
- Heat transfer module ------> metal processing ------> austenite decomposition (Audc)

The FEM solution of induction hardening is complicated for studying complex industrial cases and needs to compute fully coupled Multiphysics. This model reduces such complexity by categorizing the physics interface in different studies and computing them in a selected step. In the same model builder, it is possible to solve different types of study by adding different Multiphysics modules and categorising them into study groups (study 1 and study 2). To do this, first, the physics-controlled to user-defined control, then allowed it to compute in a selected sequence for variables that have not been solved. As part of this model, magnetic fields, heat transfer, and solid mechanics are solved in study 1, and austenite decomposition in study 2. The results of study 1 are referred to as preliminary findings for study 2, which specifically analyses the mechanical properties resulting from the martensite transformation.

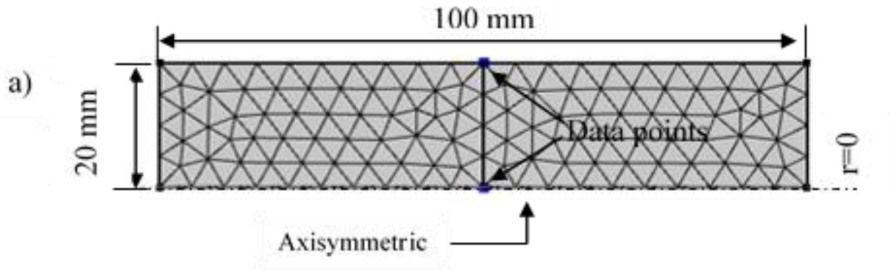

Figure 6.3 Finite element mesh

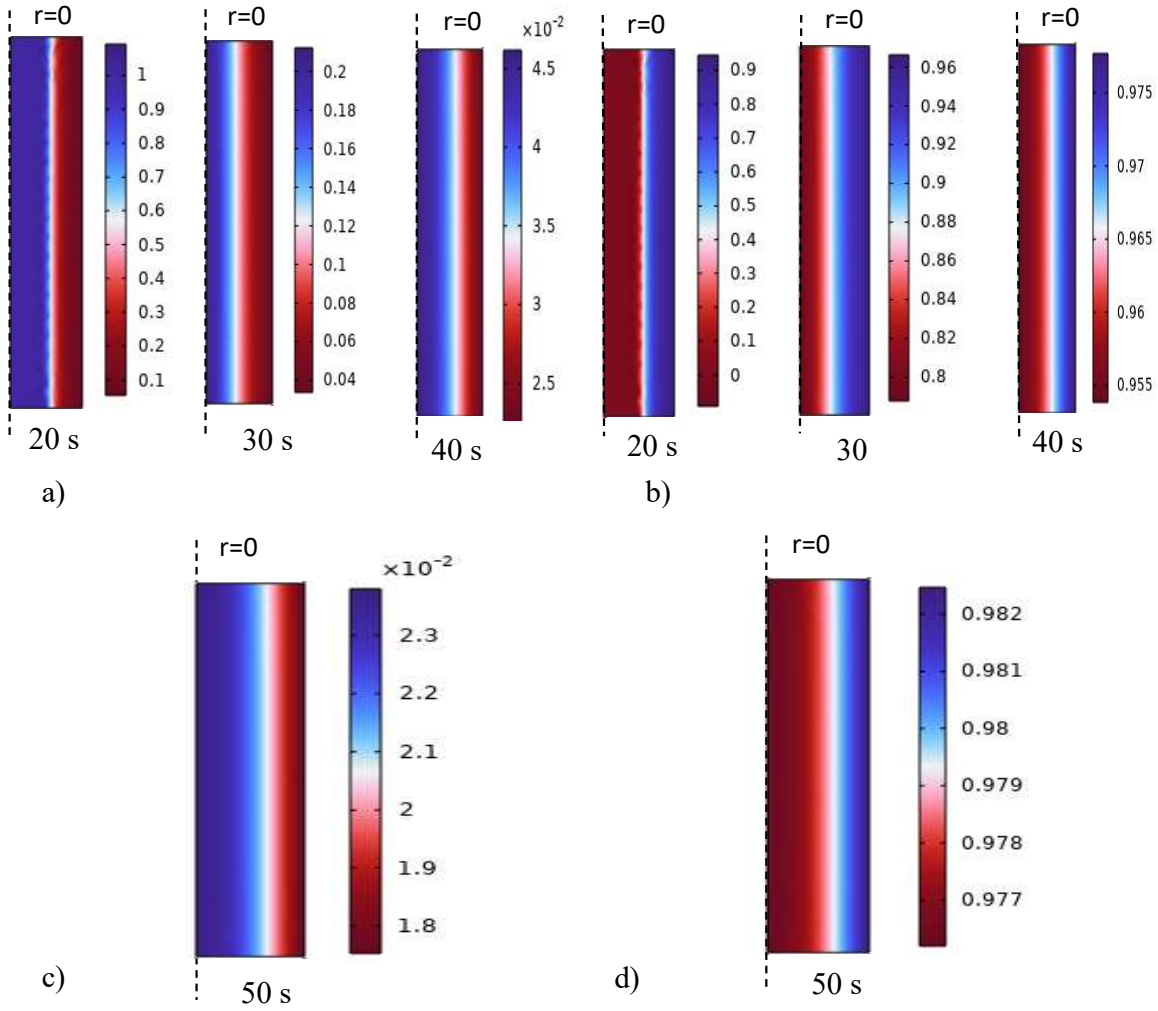

Figure 6.4: Phase distribution during martensite phase transformation, 6.4a: Austenite phase fraction rate, 6.4b: Martensite phase fraction rate, 6.4c: Final austenite phase fraction, 6.4d: Final martensite phase fraction.

The percentage of austenite decreases with the cooling temperature, while the percentage of martensite rises as the cooling progresses. As the rate of cooling is highly rapid until it attains M_s temperature, the transformation contains neither ferrite, nor pearlite or bainite, only consists of martensitic transformation with small percentage of retained austenite. Figures 6.4 a and b show sensitivity analysis of phase fraction as cooling progresses. Rapid quenching is essential to prevent formation of other phases than martensite with small amounts of retained austenite.

In this work convective cooling was performed by providing a uniform and intense water jet to the surface. The average cooling rate from maximum temperature to M_s start temperature is about 253 °C/s, which is much greater than the critical cooling rate (CCR) of complete martensite transformation of AISI 4140 (see section 4.3.4). Final percentage of martensite on the surface of the workpiece is approximately 98% while retained austenite is less than 2% (Figure 6.4c and 6.4d).

The simulation was conducted twice: one involving the transformation with TRIP consideration and the other without considering TRIP. It utilised 2436 elements and 1728 nodes, employing a free triangular mesh covering an area of $0.002\ \mathrm{m}^2$. Due to symmetry only half of the geometry is shown. It took 3 hours and 10 minutes to complete the calculation with TRIP consideration, whereas 1 hour and 51 minutes for the computation without TRIP on a desktop computer with 3.8 GHz and 1.8 TB of local disk capacity. The computation time for the simulation with TRIP was slightly longer. The preferred mesh was fine, with quality measures focussing on skewness.

Colour contour analysis is also essential to demonstrate the care with which an analyst explores input assumptions and derives inferences (Figure 6.3b). At the end of 50 seconds, less than 2% retained austenite, and approximately 98% martensite was present in the composition.

6.7 Boundary condition

A boundary condition of the quenching process requires a separate definition of thermal and mechanical boundary conditions. Thermal boundaries differ from mechanical boundaries in that they involve an unknown scalar temperature and only two types of boundary: those associated with thermal flow during quenching and symmetry planes where thermal flow is assumed to be zero.

Heat flux for the surfaces in contact with the quench medium is evaluated as follows (Lee & Van Tyne, 2012).

$$q(T_s, T_q) = h(T_s)(T_s - T_q), \tag{6.23}$$

where q is the heat flux from the surface, T_s and T_q are the surface temperature of the workpiece and the temperature of the quench medium, and $h(T_s)$ is the temperature-dependent heat transfer coefficient on the surface. The surface that is not in contact with the quench medium or the symmetry surface is defined as

$$-\lambda \frac{\partial T}{\partial n} = 0, \tag{6.24}$$

Where $\partial T/\partial n$ is the directional derivative of the temperature concerning the outward normal. At time $t = 0$, $T(x, y, z, t) = T_0$, where T_0 is the austenitizing temperature.

6.8 Kinetics of athermal martensite transformation

The kinetics of athermal martensite transformation describes how martensite forms within a sample. The overall rate of transformation is controlled by nucleation and growth. Thus, the nucleation event holds significant importance in martensitic transformations, because of its impact on the final shape of the fully developed plate. If a number of nuclei is large, it results in a finer final grain size of martensite, potentially enhancing the strength of steel. This indicates that the initiation of martensite nucleation affects the strength and toughness of martensitic steels for a given grain size. Because growth can occur rapidly, each nucleation event immediately results in the formation of a volume of the new phase.

Therefore, the proportion of the volume of martensite fluctuates only based on the level of undercooling, indicating the thermal nature of the transformation. Figure 6.4 (left) illustrates the temperature histories on the surface and at the core during quenching, obtained from the FE simulation. The transformation at the surface begins earlier than at the core. The surface temperature rapidly decreases to the martensite starting ($M_s = 350$ °C) temperature at $t_1 = 2.15$ s, while the temperature at the core gradually decreases, reaching the M_s point at about $t_2 = 25.2$ s. The surface transformation is almost complete by the time the core begins its transformation.

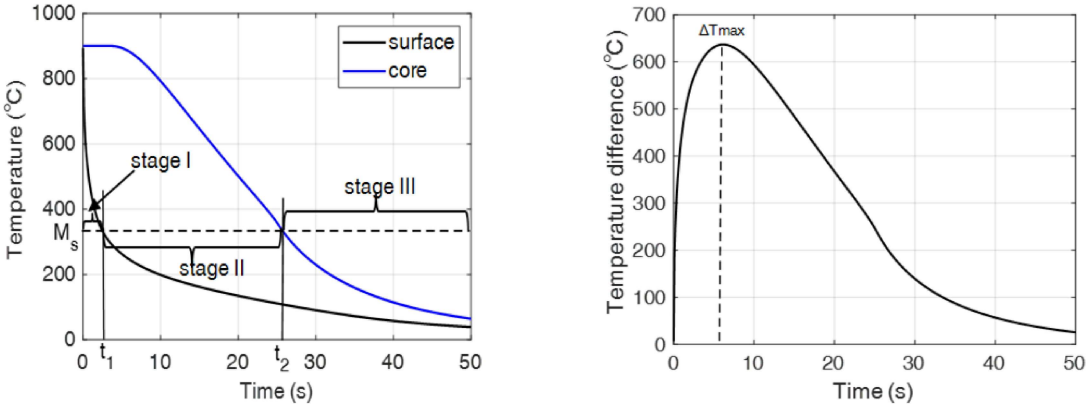

Figure 6.5: Temperature profiles on the surface and the core (left) and difference in temperatures between the surface and core (right).

When the temperature difference between the surface and the core reaches its maximum value ($\Delta T_{\max}$), as illustrated in Figure 6.5 (right), the cooling rate in the core exceeds that of the surface. Beyond this point, approximately at t = 6 s, the core changes rapidly changes until it reaches the M_s point at $t_2 = 25.2$ s. As the cooling time continues to 50 s, the core completes its transformation to martensite and the surface transformation is nearly completed. After 50 s of cooling, the difference in temperature between the surface and the core reaches less than 50 °C, Figure 6.5 (right).

At the initial stage of quenching, austenite cools down without phase transformations due to significant thermal gradients. Consequently, the surface contracts faster than the core, resulting in tensile stresses on the surface and compression stress at the core Figure 6.5 (left) to maintain a balanced stress state on the surface. The second stage begins when the martensitic transformation starts on the surface. The third stage begins when phase transformations start at the core leading to a complete transformation and cooling of the surface.

6.9 Induction hardening process

As the material undergoes plastic deformation, its mechanical properties vary, leading to changes in both the geometry and location of its yield surface. This resulting yield surface in a material experiencing plastic deformation is commonly referred to as the loading surface, which behaves similarly to the yield surface. The evolution of the initial yield surface during plastic deformation is governed by the hardening rule. Several hardening rules have been developed to describe the

behaviour of elastoplastic materials, including isotropic, kinematic, and mixed mode hardening rules.

The loading surface can be defined as a function of stress, plastic strain, and hardening parameters k as

$$f = f\ (\sigma_{ij}, \varepsilon_{ij}^{p}, k) \tag{6.25}$$

Here, the hardening parameter k is a function of the plastic strain ε_{ij}^{p}. To establish the loading/unloading condition, first define the normal unit vector to the loading surface as

$$N_{ij} = \frac{\partial f / \partial \sigma_{ij}}{\left(\frac{\partial f}{\partial \sigma_{kl}} \frac{\partial f}{\partial \sigma_{kl}}\right)^{1/2}}. \tag{6.26}$$

Loading, and consequently plastic deformation occurs if

$$f = 0 \text{ and } N_{ij} \cdot \dot{\sigma}_{ij} > 0, \tag{6.27}$$

where $\dot{\sigma}_{ij}$ represents stress rate, and the angle between the N_{ij} and σ_{ij} is acute.

Unloading condition can be described as

$$f = 0 \text{ and } N_{ij} \cdot \dot{\sigma}_{ij} < 0. \tag{6.28}$$

Sometimes there is a neutral loading condition in which neither loading nor unloading occurs.

$$f = 0 \text{ and } N_{ij}\dot{\sigma}_{ij} = 0 \tag{6.29}$$

In this case, no plastic deformation occurs.

6.9.1 Isotropic hardening

Isotropic hardening is the most straightforward hardening model that involves the expansion of the yield surface without any distortion or translation. The loading surface of a material can be characterised as

$$f(\sigma_{ij}, k) = \overline{f}(\sigma_{ij}) - k(\varepsilon_p), \tag{6.30}$$

where ε_p is the effective plastic strain which regulates the hardening, and it can be defined using two distinct methodologies. ε_p can be determined first as the accumulative plastic strain and second using the plastic work per unit volume as follows in the absence of rate dependence.

$$\dot{\varepsilon}_p = C\sqrt{\dot{\varepsilon}_{ij}^P \dot{\varepsilon}_{ij}^p}\,, \tag{6.31}$$

where $C = \sqrt{2/3}$ according to the uniaxial stress state.

$$\dot{W}_p = \sigma_e \dot{\varepsilon}_p\,, \tag{6.32}$$

where σ_e is the effective stress defined based on the loading surface and $\dot{W}_p$ can be also defined as,

$$\dot{W}_p = \sigma_{ij} \dot{\varepsilon}_{ij}^p\,. \tag{6.33}$$

In the case of the von Mises loading surface, $\sigma_e = \sqrt{3J_2}$ and Equations (6.32) and (6.33) lead to a similar $\dot{\varepsilon}_p$. Here, J_2 is second invariant of the deviatoric stress tensor.

6.9.2 Kinematic hardening

In some materials, an increase in yield stress occurs in the direction of applied stress and plastic deformation, resulting in a decrease in yield stress in the opposite direction. This phenomenon is commonly termed the Bauschinger effect, representing directional anisotropy. Isotropic hardening predicts an increase in yield stress in both directions, and thus fails to capture this effect (Hakansson et al., 2005). To model such types of hardening, kinematic hardening can be introduced. Kinematic hardening involves a rigid body translation of the loading surface while keeping the remaining geometric properties of the loading surface unchanged.

The loading surface with kinematic hardening can be defined as follows:

$$f\left(\sigma_{ij}, \varepsilon_{ij}^p\right) = \overline{f}\left(\sigma_{ij} - \alpha_{ij}\right) - k, \tag{6.34}$$

where k is a material constant and α_{ij} defines the center of the loading surface. The relationship between the center of the loading surface α_{ij} and plastic strain tensor ε_{ij} can be defined as in equation (6.35). The simplest kinematic hardening rule is assuming the linear relation between α_{ij} and ε_{ij}^p, which is commonly termed as Prager hardening rule (Hunsaker et al., 1976).

$$\dot{\alpha}_{ij} = c\dot{\varepsilon}_{ij}^p \tag{6.35}$$

Here, c is a material constant. However, this model exhibits inconsistencies in stress subspaces (i.e., when some stress components are zero, while others are not), leading to distortion in the loading surface. (Ziegler, 1959) proposed a modification to Prager's kinematic hardening rule:

$$\dot{\alpha}_{ij} = \dot{\mu}\sigma_{ij} - \alpha_{ij}, \tag{6.36}$$

where $\dot{\mu}$ parameter depends on the plastic deformation.

$$\dot{\mu} = a\dot{\varepsilon}_{p,} \tag{6.37}$$

where a is material constant.

6.9.3 Mixed hardening

The evolution of the loading surface might follow a combination of isotropic and kinematic hardening rules to capture both loading surface expansion and translation of the loading surface respectively.

$$f(\sigma_{ij}, \varepsilon_{ij}^{p}) = \overline{f}(\sigma_{ij} - \alpha_{ij}) - k(\varepsilon_{p}) \tag{6.38}$$

Here, the expansion of the loading surface is regulated by the term $k(\varepsilon_p)$, while the translation is determined by the term α_{ij}.

6.10 Stress tensor

During the initial cooling stage, the surface experiences tension while the centre is compressed due to thermal gradients, leading to plastic strains in the austenite. As martensitic transformation initiates at the surface (at the M_s temperature), unloading follows due to volume expansion, accompanied by transformation plasticity strains. In the final stage, the surface is unloaded. While the transformation progresses on the surface, the center initially undergoes compression unloading. Subsequent tension loading generates plastic strains, followed by a final unloading stage due to martensitic transformation in the centre.

Figure 6.6 illustrates the loading path and the impact of TRIP both at the surface and in the core during martensitic transformation.

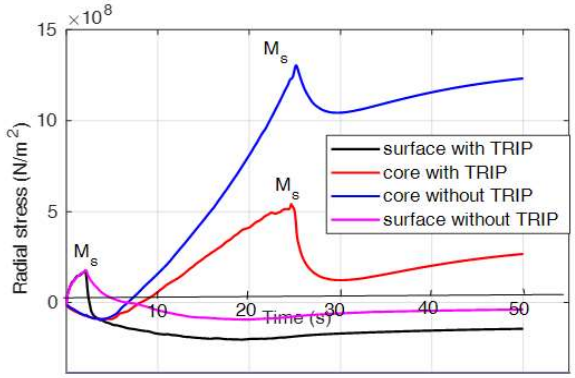

Figure 6.6: Radial stress loading and reverse loading with and without TRIP

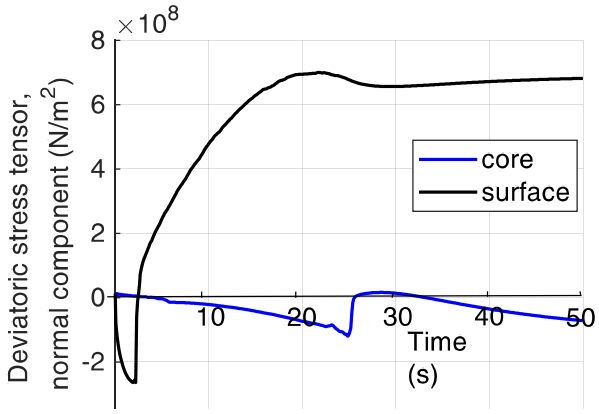

Figure 6.7: Deviatoric stress tensor (Gauss point evaluation)

In the computations involving TRIP, since the martensitic transformation begins on the surface (beginning at 350°C), the material undergoes unloading: the equivalent total strain increases, and the stress transitions more rapidly from tension to compression. The unloading between $140\,°C$ and room temperature is attribute to the martensitic transformation occurring within the interior of the piece.

Deviatoric stress deviates from hydrostatic pressure, quantifying the difference between the applied stress and the average stress as shown in Equations (6.16). In Figure 6.7, the deviatoric at the surface and the core is depicted during the quenching process.

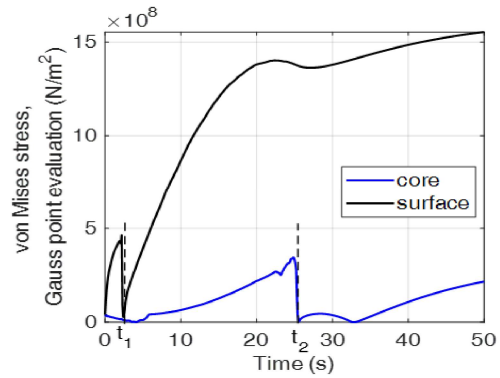

Figure 6.8: Von Mises stress vs time (s)

The material undergoes rapid cooling during quenching, resulting in thermal stresses and phase transformations. The von Mises stress considers these components, offering a single scalar value that represents the equivalent uniaxial stress. Figure 6.8 illustrates the von Mises stress on the surface and core. The von Mises stress is used to predict the yield of material under complex loading based on the results of the uniaxial tensile test.

6.11 Strain tensor

In Figure 6.9, the development of the strain tensor on the surface and the core is illustrated. Before the M_s temperature on the surface, a significant strain development rate is observed due to intense contraction during quenching.

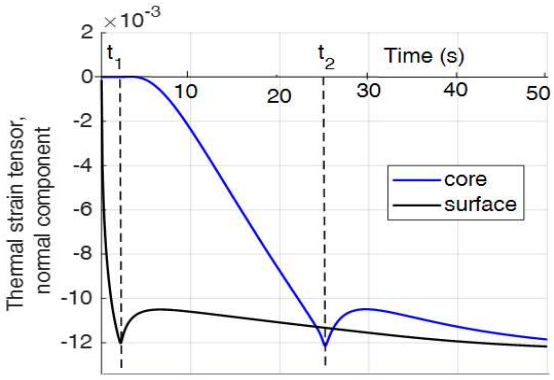

Figure 6.9: Thermal strain tensor vs duration of quenching time

Beyond this point t_1, gradual development is observed. Initially, the core does not strain for about 5 seconds due to the high-temperature difference. Subsequently, the rapid growth of thermal strain

occurs until it reaches t_2, the point at which the core temperature crosses the M_s point. After that, a gradual increase in magnitude is observed throughout cooling.

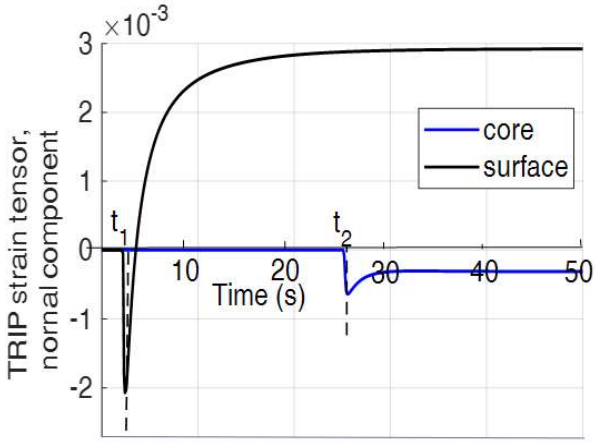

Figure 6.10: TRIP strain tensor

The TRIP effect enhances the work-hardening rate, delays the onset of necking, and promotes excellent formability. The magnitude of TRIP strain increases in the applied stress direction and reaches its maximum value when the applied stress is equal to the yield strength of austenite, as shown in Figure 6.10. As the transformation continues, the TRIP strain diminishes in the direction of applied stress due to stress relaxation caused by plastic deformation (Lee & Van Tyne, 2012).

On the surface of the tested quenched steel, the TRIP strain observed reaches its maximum at t_1 and then changes direction due to stress relaxation. In the core, a minor TRIP strain is observed after point t_2 (Figure 6.10). The TRIP strain tensor is a crucial parameter for characterising the mechanical behaviour of materials that undergo plastic transformation. It aids in understanding how materials deform plastically during phase transformations and is essential for designing advanced materials with enhanced mechanical properties.

Figure 6.11 shows the combined effect of temperature change and phase transformations during quenching. This combined effect is essential to predict and manage the mechanical behaviour of materials throughout quenching processes. It encompasses the sum of thermal and TRIP strains.

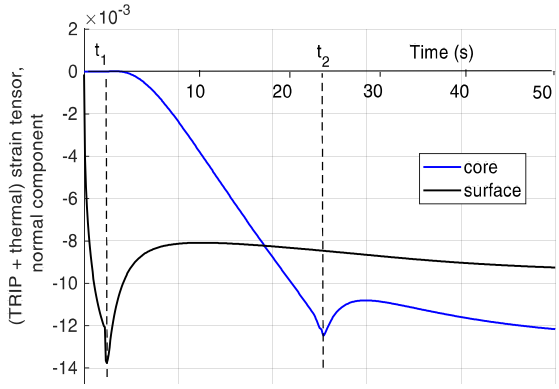

Figure 6.11: Combined effect of TRIP and thermal strain tensors

6.12 Influence of TRIP on strain hardening

Transformation plasticity refers to the excessive plastic that occurs because of the deformation that occurs in the soft austenite phase during cooling, driven by the interplay between thermal and transformation stresses. Only those variants orientated toward the applied stress (thermal stress) nucleate during the transformation process. This nucleation induces anisotropic deformation of austenite, resulting in a TRIP strain.

The total strain energy of an isotropic linear elastic material is often divided into two parts: the dilatation energy, associated with a volume change, and the distortion energy, associated with a change in shape.

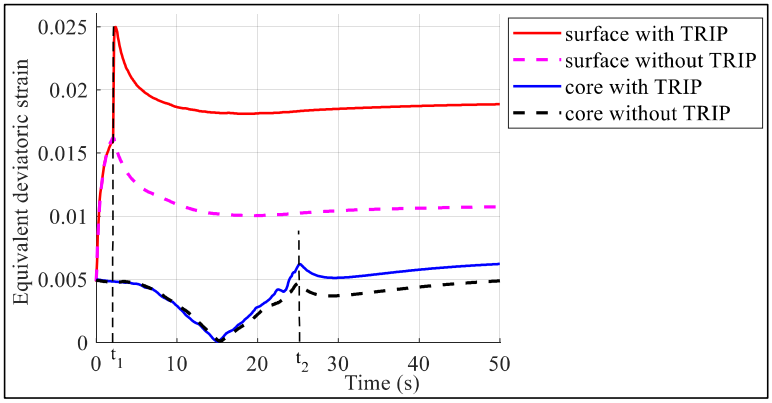

Figure 6.12: Equivalent deviatoric strain on the surface and core, with and without TRIP

Deviatoric strain refers to the part of the strain tensor that represents the change in the shape of a material without considering its volume change. Figure 6.12 shows the effect of TRIP on the

formation of deviatoric strains on the surface and core, respectively. The presence of TRIP effects in the analysis of deviatoric deformation involves considering the additional deformation associated with phase transformations during plastic deformation. Without TRIP, the material undergoes deviatoric deformation due to external forces or loads without considering additional phase transformations.

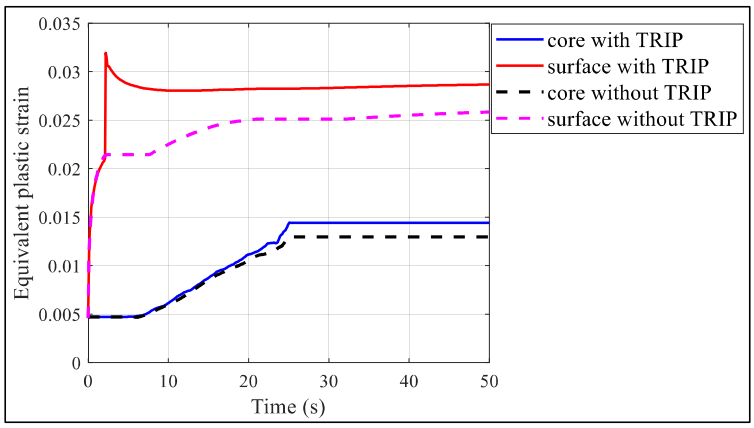

Figure 6.13: Equivalent plastic strain on the surface and core, with and without TRIP

Figure 6.13 illustrates the effect on developing equivalent plastic strain at the surface and core simultaneously. Equivalent plastic strain measures the cumulative plastic deformation during quenching. In the absence of TRIP, the equivalent plastic strain reflects the plastic deformation experienced by the material during quenching without any contribution from phase transformations. With TRIP effects, the material undergoes both conventional plastic deformation and phase transformations, and the equivalent plastic deformation reflects the cumulative impact of these processes.

In linear strain-hardening, the stress and strain field equations are incorporated with terms incorporating the strain-hardening parameter. However, the current study includes nonlinear strain hardening, characterized by a piece-wise linear behaviour.

Figure 6.14 demonstrates the effect of TRIP on the strain hardening function on the surface and the core, respectively. This function typically represents the conventional hardening behaviour associated with accumulating dislocations and other microstructural changes induced by plastic deformation. With TRIP effects, the hardening function must account for the traditional plastic deformation and the additional contribution from phase transformations during quenching.

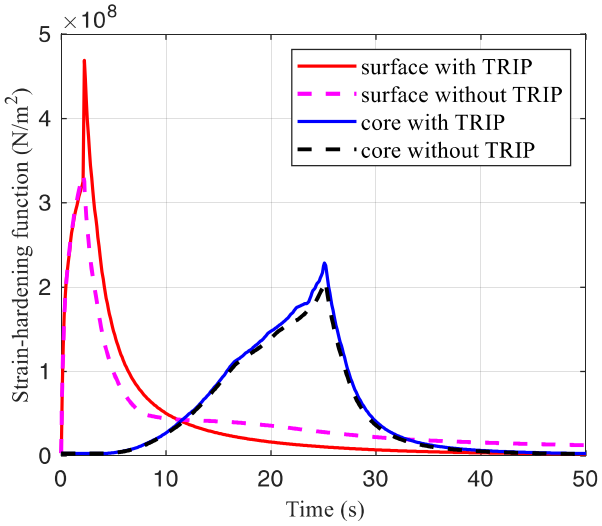

Figure 6.14: Strain-hardening function on the surface and core, with and without TRIP

The material can change its microstructure due to phase transformations, which influences its hardness and the effects of conventional plastic deformation. Consequently, the hardening function with TRIP during quenching considers both the traditional plastic deformation and the influence of phase transformations on the hardness of the material, making it more comprehensive than the hardening function without TRIP.

Chapter 7

Conclusions and Perspective

7.1 Conclusions

The analysis of thermal stress resulting from induction heating and cooling includes various aspects, including heat transfer, metallurgical changes, and mechanical effects. To achieve the desired mechanical properties, a comprehensive analysis of the entire process is essential. For such multiphysics experiments, numerical modelling makes invaluable contributions by providing visualisation and a deep understanding of the process. Although model analysis does not fully represent experimental work, it is crucial for optimisation approaches and reduces the time needed for trial calibration. The key findings and contributions of this dissertation to the field are summarised as follows.

7.1.1 Numerical modelling for the automation of induction power control

Low-frequency induction heating is suitable for heating large areas of a workpiece without significantly affecting the surface, but it requires long heating durations, leading to inefficient energy usage. In contrast, high-frequency induction heating offers good energy efficiency due to a high-power supply but is limited to heating only the surface. Consequently, achieving a uniform desired temperature at the required location becomes challenging. Therefore, controlling input power through a feedback control loop linked to the power generator is crucial to obtain the desired temperature and subsequent mechanical properties. Three distinct algorithms were developed to assess the temperature distribution from the surface to the core: explicit and implicit event control algorithms, along with discrete frequency control synchronised with the coil current. This approach addresses the common problem of electromagnetic heating "skin effect" and improves the efficiency of heat energy.

In an implicitly controlled event, it is typically necessary to specify a fixed maximum absolute value for the temperature variation. This ensures that at the end of the heating process, the temperature at any point within the workpiece does not exceed the prescribed value relative to the desired temperature. Implementing implicitly defined control parameters, with a soak stage at

the end of heating, is crucial before subsequent hot working operations. This establishes a desired temperature profile within the workpiece that meets specific requirements.

Controlling input power based on the temperature feedback loop does not affect heat transfer across the radial direction. As the core temperature is low, the high temperature on the surface continues to flow toward the lower temperature, significantly influencing the surface temperature and preventing overheating. The use of high-frequency electromagnetic energy for induction heating is problematic because the skin effect is more pronounced in materials with low thermal conductivity.

7.1.2 Mathematical modelling of thermal stresses in induction surface hardening

Controlling the quenching process is challenging, as quenched steel generates an excess of martensite, which is then gradually tempered to achieve the desired structure for the intended application. For an accurate computation of thermal stress and strain, it is crucial to track the entire sequence of phase transformations in parallel with the temperature evolution. The process involves solving Maxwell's equations for the electromagnetic field, the heat conduction equation for temperature evolution, and the Koistinen-Marburger equation for the martensitic phase transformation. It is highly coupled and requires consideration of temperature-dependent material properties and well-defined boundary conditions.

The quenching process initiates rapid tensile stresses on the surface and compressive stresses on the core. When the martensitic transformation begins at the M_s point on the surface, dilatational phase-transformation strains and transformation plasticity lead to rapid unloading and reverse loading on the surface, resulting in compression on the surface and tension at the core. Understanding the distribution of strains and stresses within hardened layers is crucial to assessing the risk of cracks and other damage, particularly in critical components used in machinery, automotive, or aerospace industries. Surface hardening aims to improve the mechanical properties of the workpiece surface for machine components subjected to surface loads (e.g., gears, sprockets, shafts).

The science behind martensite formation is complex and involves factors such as alloy composition, austenitizing temperature, cooling rate, quenching medium, and the shape or size of the workpiece. The cooling rate is a critical factor in martensite formation, significantly

influencing the final microstructure and mechanical properties of the material. The faster the cooling rate, the more likely it is to form martensite. From the CCT curve, one can determine the optimal cooling rate and temperature range can be determined to achieve the desired microstructure and mechanical properties in the final product.

7.1.3 Calibration of the gear wheel model as an optimisation strategy

The technique of model calibration for optimisation plays a crucial role in supporting engineering design and the adoption of multi-fidelity surrogate models. Calibration ensures that the parameters of the hardening process, such as power settings, frequency, and duration, are accurately set to achieve the desired hardness and mechanical properties. Optimal modelling involves creating computational simulations or mathematical models to predict how the induction hardening process will affect the material properties, allowing for optimisation and fine-tuning before actual implementation. The overall process aims to improve the efficiency, durability, and performance of the gear wheels through advanced engineering techniques.

For small gears where the tooth-by-tooth scanning method is not applicable, obtaining the desired temperature profile by conventional heating is challenging. Therefore, having insight into the calibration of the combinations of parameters at low computational cost for optimisation is essential. Defining key elements for optimisation (objective function, decision variables, and constraints) of the desired temperature profile and the consequent mechanical properties is the method implemented in this work. The accuracy of the final optimal solution depends on the precision of these surrogate models. Since the optimal solution to the original problem is typically unknown beforehand, designers must ensure that each surrogate model maintains high predictive accuracy throughout the design space.

The quality of the model significantly affects both the computational cost and the convergence characteristics in the optimisation process. The proposed objective functions must be extremised in accordance with the requirements. Extremisation is achieved through a relevant optimisation scheme using a suitable deterministic algorithm. Among the various optimisation techniques performed, the best results were obtained using the Nelder–Mead and BOBYQA algorithms. An alternative approach to mitigate limitations and improve predictive accuracy is to create an ensemble by combining individual models.

7.1.4 Assess the impact of TRIP strain on the mechanical properties of a material

The material can change its microstructure due to phase transformations, which influence its hardness and the effects of conventional plastic deformation. Only those variants orientated toward the applied stress due to minimization of Gibbs free energy, which includes thermodynamic driving force and mechanical energy due to transformation stresses nucleate during the transformation process. This nucleation induces anisotropic deformation of austenite, resulting in TRIP strain. TRIP strain refers to the excessive plastic deformation that occurs in the soft austenite phase during cooling, driven by the interplay between thermal and transformation stresses. Consequently, the hardening function with TRIP during quenching considers both traditional plastic deformation and the influence of phase transformations on the hardness of the material, making it more comprehensive than the hardening function without TRIP

The TRIP effect enhances the work hardening rate, delays the onset of necking, and promotes excellent formability. The magnitude of TRIP strain increases in the direction of the applied stress and reaches its maximum value when the applied stress equals the yield strength of austenite. In the absence of TRIP, the equivalent plastic strain reflects the plastic deformation experienced by the material during quenching without any contribution from phase transformations. With TRIP effects, the material undergoes both conventional plastic deformation and phase transformations, and the equivalent plastic deformation reflects the cumulative impact of these processes. It aids in understanding how materials deform plastically during phase transformations and is essential for designing advanced materials with enhanced mechanical properties.

Extracting the TRIP strain from the total strain by experimental analysis of quenching poses significant challenges. However, using FEA can address these challenges and enable the prediction of multiple co-occurring physical phenomena. At the initial stage of quenching, austenite cools down without phase transformations as a result of significant thermal gradients. Consequently, the surface contracts faster than the core, resulting in tensile stresses on the surface and compression stresses at the core to maintain a balanced stress state. The second stage begins when the martensitic transformation starts on the surface. The third stage begins when phase transformations start at the core, leading to complete transformation and cooling of the surface resulting in compressive stress on the surface and tensile at the core.

7.2 Perspective

In this work, some of the knowledge gaps in assessing thermal stresses and strains in steel materials during induction heating and cooling (quenching) have been addressed. However, many research questions remain unanswered and need to be explored in future studies. The following research gaps should be addressed to gain a detailed understanding of thermal stresses and strains to optimise the induction hardening process.

1. The heating rate in the induction heating process influences the Ac_1 and Ac_3 temperatures. However, further studies are needed to incorporate a time-dependent analysis of the austenite transformation process, which can potentially lead to a shift in the Ac_1 and Ac_3 temperatures. This, in turn, would modify the CCT diagram, which depends on several factors, including the chemical composition of the steel, the nature of cooling, the grain size, the extent of austenite homogenisation, as well as the austenitizing temperature and time. From the CCT curve, one can determine the optimal cooling rate and temperature range can be determined to achieve the desired microstructure and mechanical properties in the final product.
2. Extracting the TRIP strain from the total strain using experimental analysis is highly challenging. Therefore, this is one of the core aspects that needs improvement in this field. The results of the modelling indicate that considering both conventional plastic deformation and the influence of phase transformations on the hardness of the material is more realistic in the design of advanced materials with enhanced mechanical properties. These results of the numerical model need to be supported by experimental evidence, which should be the focus of future work.
3. In hardening, optimisation of the surface and edges is crucial for enhancing the resistance to indentation in machine components. However, achieving uniform temperature distribution in complex-shaped components, particularly in specific corner zones, remains a challenging and unresolved task. This problem is highly pronounced in machine components such as gears, crankshafts, and sprockets. The solution lies in optimising the design parameters and operation modes of the induction system for the surface hardening process.

4. Transformation kinetics requires further research to include intermediate phase transformations and additional free-energy curves that appear in phase diagrams. Reaching total equilibrium in practical solid-state phase transformations is rare. However, modelling transformations using the concept of local equilibrium across an interphase interface and the deviation from local equilibrium can provide the driving force on the interface. The importance of surface energy on the thermodynamics of nanomaterials is significant, as the implementation of the concept of nano dimensions contributes to changes in crystal structure.
5. Induction hardening is among the oldest technologies in both industrial and domestic applications. It is often hindered by a reliance on traditional methods, mostly due to the simplicity in modelling, which may impede its growth. However, modern technologies, such as the implementation of machine learning and artificial neural networks (ANNs) for optimisation, have recently emerged but require further development. A promising way to achieve a trade-off between prediction accuracy and computational cost in modelling is to integrate realistic information into the construction of a surrogate model.
6. In the induction heating and cooling (quenching) process, assumptions and model simplifications are commonly observed in the work of many researchers. This indicates the need for further work in this field to build multi-fidelity surrogate models that incorporate important assumptions. A crucial factor for the successful use of multi-fidelity surrogate models is that the low-fidelity model should capture the overall trend of the responses from the high-fidelity model. In constructing multi-fidelity surrogate models, a large amount of low fidelity data is used to reduce computational burden, while a few high-fidelity samples are selected to ensure prediction accuracy. A promising solution to this challenge is to build multifidelity surrogate models that integrate both high and lowfidelity data, thus balancing prediction accuracy and computational cost.

Bibliography

Afzal, M. J., & Buhl, J. (2022). Numerical Study to Promote the Residual Stresses Development during ISF Process with Improvement in Two Point Incremental Die Forming. *Key Engineering Materials*, *926*, 752–759. https://doi.org/10.4028/p-yr4vg6

Alshaya, A. A. (2023). A developed hybrid experimental–analytical method for thermal stress analysis of a deep U-notched plate. *Theoretical and Applied Fracture Mechanics*, *124*, 103753. https://doi.org/10.1016/j.tafmec.2023.103753

Álvarez Hostos, J. C., Bencomo, A. D., & Cabrera, E. S. P. (2018). Simple iterative procedure for the thermal–mechanical analysis of continuous casting processes, using the element-free Galerkin method. *Journal of Thermal Stresses*, *41*(2), 160–181. https://doi.org/10.1080/01495739.2017.1389325

Amitava, M., De, P. K., Bhattacharya, D. K., Srivastava, P. K., & Jiles, D. C. (2004). Ferromagnetic properties of deformation-induced martensite transformation in AISI 304 stainless steel. *Metallurgical and Materials Transactions A*, *35*(2), 599–605. https://doi.org/10.1007/s11661-004-0371-6

Araneo, R., Dughiero, F., Fabbri, M., Forzan, M., Geri, A., Morandi, A., Lupi, S., Ribani, P. L., & Veca, G. (2008). Electromagnetic and thermal analysis of the induction heating of aluminum billets rotating in DC magnetic field. *COMPEL - The International Journal for Computation and Mathematics in Electrical and Electronic Engineering*, *27*(2), 467–479. https://doi.org/10.1108/03321640810847751

Areitioaurtena, M., Segurajauregi, U., Fisk, M., Cabello, M. J., & Ukar, E. (2022). Numerical and experimental investigation of residual stresses during the induction hardening of 42CrMo4 steel. *European Journal of Mechanics - A/Solids*, *96*, 104766. https://doi.org/10.1016/j.euromechsol.2022.104766

Areitioaurtena, M., Segurajauregi, U., Urresti, I., Fisk, M., & Ukar, E. (2020). Predicting the induction hardened case in 42CrMo4 cylinders. *Procedia CIRP*, *87*, 545–550. https://doi.org/10.1016/j.procir.2020.02.034

Ariza, E. A., Martorano, M. A., Batista De Lima, N., & Tschiptschin, A. P. (2014). Numerical Simulation with Thorough Experimental Validation to Predict the Build-up of Residual Stresses during Quenching of Carbon and Low-Alloy Steels. *ISIJ International*, *54*(6), 1396–1405. https://doi.org/10.2355/isijinternational.54.1396

Asadzadeh, M. Z., Raninger, P., Prevedel, P., Ecker, W., & Mücke, M. (2021). Hybrid modeling of induction hardening processes. *Applications in Engineering Science*, *5*, 100030. https://doi.org/10.1016/j.apples.2020.100030

Asadzadeh, Raninger, Prevedel, Ecker, & Mücke. (2019). Inverse Model for the Control of Induction Heat Treatments. *Materials*, *12*(17), 2826. https://doi.org/10.3390/ma12172826

Babu, K., & Prasanna Kumar, T. S. (2010). Mathematical Modeling of Surface Heat Flux During Quenching. *Metallurgical and Materials Transactions B*, *41*(1), 214–224. https://doi.org/10.1007/s11663-009-9319-y

Balanis, C. A. (2012). *Advanced engineering electromagnetics* (Second edition). Wiley.

Bardelcik, A., Salisbury, C. P., Winkler, S., Wells, M. A., & Worswick, M. J. (2010). Effect of cooling rate on the high strain rate properties of boron steel. *International Journal of Impact Engineering*, *37*(6), 694–702. https://doi.org/10.1016/j.ijimpeng.2009.05.009

Barglik, J. (2016). Mathematical modeling of induction surface hardening. *COMPEL: The International Journal for Computation and Mathematics in Electrical and Electronic Engineering*, *35*(4), 1403–1417. https://doi.org/10.1108/COMPEL-09-2015-0323

Barglik, J. (2018). Induction hardening of steel elements with complex shapes. *PRZEGLĄD ELEKTROTECHNICZNY*, *1*(4), 53–56. https://doi.org/10.15199/48.2018.04.13

Barglik, J., Kotlan, V., Smalcerz, A., Smagór, A., Desisa, D., & Doležzel, I. (2023). An improved model of hardening gear wheels and determining the electrical efficiency of the process. *2023 24th International Conference on Computational Problems of Electrical Engineering (CPEE)*, 1–4. https://doi.org/10.1109/CPEE59623.2023.10285320

Barglik, J., Smagór, A., & Smalcerz, A. (2018). *Computer simulation of single frequency induction surface hardening of gear wheels: Analysis of selected problems*.

Barglik, J., Smagór, A., Smalcerz, A., & Desisa, D. G. (2021a). Induction Heating of Gear Wheels in Consecutive Contour Hardening Process. *Energies*, *14*(13), 3885. https://doi.org/10.3390/en14133885

Barglik, J., Smagór, A., Smalcerz, A., & Desisa, D. G. (2021b). Induction Heating of Gear Wheels in Consecutive Contour Hardening Process. *Energies*, *14*(13), 3885. https://doi.org/10.3390/en14133885

Barglik, J., Smalcerz, A., Przylucki, R., & Doležel, I. (2014). 3D modeling of induction hardening of gear wheels. *Journal of Computational and Applied Mathematics*, *270*, 231–240. https://doi.org/10.1016/j.cam.2014.01.019

Barglik, J., Smalcerz, A., & Smagór, A. (2016). *Induction hardening of small gear wheels made of steel 50CrMo4*.

Barka, N., Bocher, P., Brousseau, J., Galopin, M., & Sundararajan, S. (2006). Modeling and Sensitivity Study of the Induction Hardening Process. *Advanced Materials Research*, *15–17*, 525–530. https://doi.org/10.4028/www.scientific.net/AMR.15-17.525

Barron, R. F., & Barron, B. R. (2012). *Design for Thermal Stresses*.

Bedekar, V., Voothaluru, R., Bunn, J., & Hyde, R. S. (2019). Measurement and prediction of through-section residual stresses in the manufacturing sequence of bearing components. *CIRP Annals*, *68*(1), 57–60. https://doi.org/10.1016/j.cirp.2019.03.004

Behrens, B. A., Brunotte, K., Wester, H., & Kock, C. (2022). Methodology to Investigate the Transformation Plasticity for Numerical Modelling of Hot Forging Processes. *Key Engineering Materials*, *926*, 547–558. https://doi.org/10.4028/p-51lv37

Bi, C., Lu, H., Jia, K., Hu, J., & Li, H. (2016). A Novel Multiple-Frequency Resonant Inverter for Induction Heating Applications. *IEEE Transactions on Power Electronics*, 1–1. https://doi.org/10.1109/TPEL.2016.2521401

Blondé, R., Jimenez-Melero, E., Zhao, L., Wright, J. P., Brück, E., Van Der Zwaag, S., & Van Dijk, N. H. (2014). Mechanical stability of individual austenite grains in TRIP steel studied by synchrotron X-ray diffraction during tensile loading. *Materials Science and Engineering: A*, *618*, 280–287. https://doi.org/10.1016/j.msea.2014.09.008

Bodart, O., Boureau, A.-V., & Touzani, R. (2001). Numerical investigation of optimal control of induction heating processes. *Applied Mathematical Modelling*, *25*(8), 697–712. https://doi.org/10.1016/S0307-904X(01)00007-5

Boudiaf, A., Taleb, L., & Belouchrani, M. A. (2011). Experimental analysis of the correlation between martensitic transformation plasticity and the austenitic grain size in steels. *European Journal of Mechanics - A/Solids*, *30*(3), 326–335. https://doi.org/10.1016/j.euromechsol.2010.12.004

Bouissa, Y., Shahriari, D., Champliaud, H., & Jahazi, M. (2019). Prediction of heat transfer coefficient during quenching of large size forged blocks using modeling and experimental

validation. *Case Studies in Thermal Engineering*, *13*, 100379. https://doi.org/10.1016/j.csite.2018.100379

Burkhart, T. A., Andrews, D. M., & Dunning, C. E. (2013). Finite element modeling mesh quality, energy balance and validation methods: A review with recommendations associated with the modeling of bone tissue. *Journal of Biomechanics*, *46*(9), 1477–1488. https://doi.org/10.1016/j.jbiomech.2013.03.022

Callister, W. D., & Rethwisch, D. G. (2015). *Fundamentals of materials science and engineering: An integrated approach* (5th edition, Wiley Binder version). Wiley.

Canale, L. C. F., Albano, L., Totten, G. E., & Meekisho, L. (2014). *HARDENABILITY OF STEEL*.

Carlone, P., Palazzo, G. S., & Pasquino, R. (2010). Finite element analysis of the steel quenching process: Temperature field and solid–solid phase change. *Computers & Mathematics with Applications*, *59*(1), 585–594. https://doi.org/10.1016/j.camwa.2009.06.006

Carrera, E., Fazzolari, F. A., & Cinefra, M. (2017). *Thermal stress analysis of composite beams, plates and shells: Computational modelling and applications*. Academic Press.

Cha, K.-H., Ju, C.-T., & Kim, R.-Y. (2020). Analysis and Evaluation of WBG Power Device in High Frequency Induction Heating Application. *Energies*, *13*(20), 5351. https://doi.org/10.3390/en13205351

Chen, X., Zhang, S., Rolfe, B., & Li, D. (2019a). The FEM simulation and experiment of quenching distortion of a U-shape sample and the sensitivity analysis of material properties. *Materials Research Express*, *6*(11), 116539. https://doi.org/10.1088/2053-1591/ab46ee

Chen, X., Zhang, S., Rolfe, B., & Li, D. (2019b). The FEM simulation and experiment of quenching distortion of a U-shape sample and the sensitivity analysis of material properties. *Materials Research Express*, *6*(11), 116539. https://doi.org/10.1088/2053-1591/ab46ee

Chereches, R.-L. (2011). *State of the Art in the Optimal Design of Electromagnetic Devices*. *52*(4).

Christensen, R. M. (1982). *Theory of viscoelasticity: An introduction* (2nd ed). Academic Press.

Davies, E. J., & Simpson, P. G. (1979). Induction heating for industry. *Electronics and Power*, *25*(7), 508. https://doi.org/10.1049/ep.1979.0295

Davis, J. R. (2002). *Surface Hardening of Steels*.

De Flaviis, F., Noro, M. G., Diaz, R. E., Franceschetti, G., & Alexopoulos, N. G. (1998). A time-domain vector potential formulation for the solution of electromagnetic problems. *IEEE Microwave and Guided Wave Letters*, *8*(9), 310–312. https://doi.org/10.1109/75.720465

Demidovich, V. B. (2012). Computer simulation and optimal designing of energy-saving technologies of the induction heating of metals. *Thermal Engineering*, *59*(14), 1023–1034. https://doi.org/10.1134/S0040601512140030

Denis, S., & Ura, C. (n.d.). CONSIDERING STRESS-PHASE TRANSFORMATION INTERACTIONS IN THE CALCULATION OF HEAT TREATMENT RESIDUAL STRESSES. *Residual Stresses*.

Dey, I., Ghosh, S. K., & Saha, R. (2019). Effects of cooling rate and strain rate on phase transformation, microstructure and mechanical behaviour of thermomechanically processed pearlitic steel. *Journal of Materials Research and Technology*, *8*(3), 2685–2698. https://doi.org/10.1016/j.jmrt.2019.04.006

Dulieu-Barton, J. M., & Stanley, P. (1999). Applications of thermoelastic stress analysis to composite materials. *Strain*, *35*(2), 41–48. https://doi.org/10.1111/j.1475-1305.1999.tb01124.x

Dziatkiewicz, G., Kuska, K., & Popiel, R. (2023). Evolutionary Optimizing Process Parameters in the Induction Hardening of Rack Bar by Response Surface Methodology and Desirability Function Approach under Industrial Conditions. *Materials*, *16*(17), 5791. https://doi.org/10.3390/ma16175791

Eckert, M., Krbata, M., Barenyi, I., Majerik, J., Dubec, A., & Bokes, M. (2020). Effect of Selected Cooling and Deformation Parameters on the Structure and Properties of AISI 4340 Steel. *Materials*, *13*(23), 5585. https://doi.org/10.3390/ma13235585

Esteve, V., Jordan, J., Sanchis-Kilders, E., Dede, E. J., Maset, E., Ejea, J. B., & Ferreres, A. (2015). Comparative Study of a Single Inverter Bridge for Dual-Frequency Induction Heating Using Si and SiC MOSFETs. *IEEE Transactions on Industrial Electronics*, *62*(3), 1440–1450. https://doi.org/10.1109/TIE.2014.2359411

Esteve, V., Pardo, J., Jordan, J., Dede, E. J., Sanchis-Kilders, E., & Maset, E. (2005a). High Power Resonant Inverter with Simultaneous Dual-frequency Output. *IEEE 36th Conference on Power Electronics Specialists, 2005.*, 1278–1281. https://doi.org/10.1109/PESC.2005.1581794

Esteve, V., Pardo, J., Jordan, J., Dede, E. J., Sanchis-Kilders, E., & Maset, E. (2005b). High Power Resonant Inverter with Simultaneous Dual-frequency Output. *IEEE 36th Conference on Power Electronics Specialists, 2005.*, 1278–1281. https://doi.org/10.1109/PESC.2005.1581794

Fakir, R., Barka, N., & Brousseau, J. (2018). Case study of laser hardening process applied to 4340 steel cylindrical specimens using simulation and experimental validation. *Case Studies in Thermal Engineering*, *11*, 15–25. https://doi.org/10.1016/j.csite.2017.12.002

Fang, X., Lu, J., Wang, J., & Yang, J. (2018). Parameter Optimization and Prediction Model of Induction Heating for Large-Diameter Pipe. *Mathematical Problems in Engineering*, *2018*, 1–12. https://doi.org/10.1155/2018/8430578

Favennec, Y., Labbé, V., & Bay, F. (2003). Induction heating processes optimization a general optimal control approach. *Journal of Computational Physics*, *187*(1), 68–94. https://doi.org/10.1016/S0021-9991(03)00081-0

Fischer, F. D., Reisner, G., Werner, E., Tanaka, K., Cailletaud, G., & Antretter, T. (2000a). A new view on transformation induced plasticity (TRIP). *International Journal of Plasticity*, *16*(7–8), 723–748. https://doi.org/10.1016/S0749-6419(99)00078-9

Fischer, F. D., Reisner, G., Werner, E., Tanaka, K., Cailletaud, G., & Antretter, T. (2000b). A new view on transformation induced plasticity (TRIP). *International Journal of Plasticity*, *16*(7–8), 723–748. https://doi.org/10.1016/S0749-6419(99)00078-9

Fisk, M., Lindgren, L.-E., Datchary, W., & Deshmukh, V. (2018). Modelling of induction hardening in low alloy steels. *Finite Elements in Analysis and Design*, *144*, 61–75. https://doi.org/10.1016/j.finel.2018.03.002

Forest, F., Laboure, E., Costa, F., & Gaspard, J. Y. (2000). Principle of a multi-load/single converter system for low power induction heating. *IEEE Transactions on Power Electronics*, *15*(2), 223–230. https://doi.org/10.1109/63.838094

Fujita, H., & Akagi, H. (1996). Pulse-density-modulated power control of a 4 kW, 450 kHz voltage-source inverter for induction melting applications. *IEEE Transactions on Industry Applications*, *32*(2), 279–286. https://doi.org/10.1109/28.491475

Fujita, H., Uchida, N., & Ozaki, K. (2007). Zone Controlled Induction Heating (ZCIH) A New Concept in Induction Heating. *2007 Power Conversion Conference - Nagoya*, 1498–1504. https://doi.org/10.1109/PCCON.2007.373162

Fujita, H., Uchida, N., & Ozaki, K. (2011). A New Zone-Control Induction Heating System Using Multiple Inverter Units Applicable Under Mutual Magnetic Coupling Conditions. *IEEE Transactions on Power Electronics*, *26*(7), 2009–2017. https://doi.org/10.1109/TPEL.2010.2101084

Gaussorgues, G. (1994). *Infrared Thermography*. Springer Netherlands. https://doi.org/10.1007/978-94-011-0711-2

Ge, Y., Hu, R., Zhang, Z., & Shen, Q. (2006). Optimization Control of Induction hardening Process. *2006 International Conference on Mechatronics and Automation*, 1126–1130. https://doi.org/10.1109/ICMA.2006.257783

Geijselaers, H. J. M. (Ed.). (2003). *Numerical simulation of stresses due to solid state transformations: The simulation of laser hardening: proefschrift*.

Geng, X., Wang, H., Xue, W., Xiang, S., Huang, H., Meng, L., & Ma, G. (2020). Modeling of CCT diagrams for tool steels using different machine learning techniques. *Computational Materials Science*, *171*, 109235. https://doi.org/10.1016/j.commatsci.2019.109235

Gomes, D. F., Tavares, R. P., & Braga, B. M. (2019). Mathematical model for the temperature profiles of steel pipes quenched by water cooling rings. *Journal of Materials Research and Technology*, *8*(1), 1197–1202. https://doi.org/10.1016/j.jmrt.2018.06.022

Green, A. M. (1996). Operation of inverters supplying mutually coupled induction heating loads. *IEE Half-Day Colloquium on Electromagnetics and Induction Heating*, *1996*, 4–4. https://doi.org/10.1049/ic:19961400

Grong, Ø., & Shercliff, H. R. (2002). Microstructural modelling in metals processing. *Progress in Materials Science*, *47*(2), 163–282. https://doi.org/10.1016/S0079-6425(00)00004-9

Grum, J. (2001). A review of the in¯uence of grinding conditions on resulting residual stresses after induction surface hardening and grinding. *Journal of Materials Processing Technology*.

Guo, E.-Y., Wang, M.-Y., Jing, T., & Chawla, N. (2013). Temperature-dependent mechanical properties of an austenitic–ferritic stainless steel studied by in situ tensile loading in a scanning electron microscope (SEM). *Materials Science and Engineering: A*, *580*, 159–168. https://doi.org/10.1016/j.msea.2013.04.060

Gür, C. H., & Pan, J. (Eds.). (2009). *Handbook of thermal process modeling of steels*. CRC Press : IFHTSE/International Federation for Heat Treatment and Surface Engineering.

Ha, P. N., Fujita, H., Ozaki, K., & Uchida, N. (2010). Analysis and control of the heat distribution in a zone-control induction heating system. *The 2010 International Power Electronics Conference - ECCE ASIA -*, 2324–2330. https://doi.org/10.1109/IPEC.2010.5543680

Ha Pham Ngoc, Fujita, H., Ozaki, K., & Uchida, N. (2009). Dynamic performance of a current-phase control method for zone-control induction heating systems. *2009 IEEE Energy Conversion Congress and Exposition*, 833–839. https://doi.org/10.1109/ECCE.2009.5315953

Hakansson, P., Wallin, M., & Ristinmaa, M. (2005). Comparison of isotropic hardening and kinematic hardening in thermoplasticity. *International Journal of Plasticity*, *21*(7), 1435–1460. https://doi.org/10.1016/j.ijplas.2004.07.002

He, B. (2020). On the Factors Governing Austenite Stability: Intrinsic versus Extrinsic. *Materials*, *13*(15), 3440. https://doi.org/10.3390/ma13153440

Hetnarski, R. B. (Ed.). (2014). *Encyclopedia of Thermal Stresses*. Springer Netherlands. https://doi.org/10.1007/978-94-007-2739-7

Hetnarski, R. B., & Eslami, M. R. (2019). *Thermal Stresses—Advanced Theory and Applications* (Vol. 158). Springer International Publishing. https://doi.org/10.1007/978-3-030-10436-8

Hömberg, D. (2004a). A mathematical model for induction hardening including mechanical effects. *Nonlinear Analysis: Real World Applications*, *5*(1), 55–90. https://doi.org/10.1016/S1468-1218(03)00017-8

Hömberg, D. (2004b). A mathematical model for induction hardening including mechanical effects. *Nonlinear Analysis: Real World Applications*, *5*(1), 55–90. https://doi.org/10.1016/S1468-1218(03)00017-8

Hunsaker, B., Vaughan, D. K., & Stricklin, J. A. (1976). A Comparison of the Capability of Four Hardening Rules to Predict a Material's Plastic Behavior. *Journal of Pressure Vessel Technology*, *98*(1), 66–74. https://doi.org/10.1115/1.3454329

Inan, E., & Tauchert, T. R. (2014). Idea of Coupled Theory of Plates. In R. B. Hetnarski (Ed.), *Encyclopedia of Thermal Stresses* (pp. 2363–2368). Springer Netherlands. https://doi.org/10.1007/978-94-007-2739-7_190

Inoue, T. (2011). Mechanics and Characteristics of Transformation Plasticity and Metallo-thermo-mechanical Process Simulation. *Procedia Engineering*, *10*, 3793–3798. https://doi.org/10.1016/j.proeng.2011.06.001

Kaiser, D., Damon, J., Mühl, F., De Graaff, B., Kiefer, D., Dietrich, S., & Schulze, V. (2020). Experimental investigation and finite-element modeling of the short-time induction quench-and-temper process of AISI 4140. *Journal of Materials Processing Technology*, *279*, 116485. https://doi.org/10.1016/j.jmatprotec.2019.116485

Karban, P., & Donátová, M. (2010). Continual induction hardening of steel bodies. *Mathematics and Computers in Simulation*, *80*(8), 1771–1782. https://doi.org/10.1016/j.matcom.2009.12.004

Kayacan, M. C., & Çolak, O. (2004). A fuzzy approach for induction hardening parameters selection. *Materials & Design*, *25*(2), 155–161. https://doi.org/10.1016/j.matdes.2003.09.017

Khalifa, M., Barka, N., Brousseau, J., & Bocher, P. (2019). Sensitivity study of hardness profile of 4340 steel disc hardened by induction according to machine parameters and geometrical factors. *The International Journal of Advanced Manufacturing Technology*, *101*(1–4), 209–221. https://doi.org/10.1007/s00170-018-2892-y

Kianezhad, M., Sajjadi, S. A., & Vafaeenezhad, H. (2015). A Numerical Approach to the Prediction of Hardness at Different Points of a Heat-Treated Steel. *Journal of Materials Engineering and Performance*, *24*(4), 1516–1521. https://doi.org/10.1007/s11665-015-1433-1

Knupp, P. M. (2001). Algebraic Mesh Quality Metrics. *SIAM Journal on Scientific Computing*, *23*(1), 193–218. https://doi.org/10.1137/S1064827500371499

Kobayashi, S., Takahashi, H., & Kamada, Y. (2013). Evaluation of case depth in induction-hardened steels: Magnetic hysteresis measurements and hardness-depth profiling by differential permeability analysis. *Journal of Magnetism and Magnetic Materials*, *343*, 112–118. https://doi.org/10.1016/j.jmmm.2013.04.082

Kohli, A., & Singh, H. (2011). Optimization of processing parameters in induction hardening using response surface methodology. *Sadhana*, *36*(2), 141–152. https://doi.org/10.1007/s12046-011-0020-x

Koistinen, D. P., & Marburger, R. E. (1959). A general equation prescribing the extent of the austenite-martensite transformation in pure iron-carbon alloys and plain carbon steels. *Acta Metallurgica*, *7*(1), 59–60. https://doi.org/10.1016/0001-6160(59)90170-1

Koric, S., & Thomas, B. G. (2008). Thermo-mechanical models of steel solidification based on two elastic visco-plastic constitutive laws. *Journal of Materials Processing Technology*, *197*(1–3), 408–418. https://doi.org/10.1016/j.jmatprotec.2007.06.060

Le, V. C., Slodička, M., & Van Bockstal, K. (2022). Existence of a weak solution to a nonlinear induction hardening problem with Leblond–Devaux model for a steel workpiece. *Communications in Nonlinear Science and Numerical Simulation*, *107*, 106156. https://doi.org/10.1016/j.cnsns.2021.106156

Lee, S.-J., & Lee, Y.-K. (2008). Finite element simulation of quench distortion in a low-alloy steel incorporating transformation kinetics. *Acta Materialia*, *56*(7), 1482–1490. https://doi.org/10.1016/j.actamat.2007.11.039

Lee, S.-J., & Van Tyne, C. J. (2012). A Kinetics Model for Martensite Transformation in Plain Carbon and Low-Alloyed Steels. *Metallurgical and Materials Transactions A*, *43*(2), 422–427. https://doi.org/10.1007/s11661-011-0872-z

Li, H., Zhao, G., & He, L. (2008). Finite element method based simulation of stress–strain field in the quenching process. *Materials Science and Engineering: A*, *478*(1–2), 276–290. https://doi.org/10.1016/j.msea.2007.05.101

Li, Z., & Ferguson, B. L. (2012). *Controlling Gear Distortion and Residual Stresses during Induction Hardening*.

Li, Z., Ferguson, B. L., Freborg, A., Goldstein, R., Jackowski, J., Nemkov, V., & Fett, G. (2014). *Stress Generation in an Axle Shaft during Induction Hardening*.

Lin, S. J., Samad, W. A., Khaja, A. A., & Rowlands, R. E. (2015). Hybrid Thermoelastic Stress Analysis. *Experimental Mechanics*, *55*(4), 653–665. https://doi.org/10.1007/s11340-014-9869-z

Lin, Z.-C., Chu, K.-T., & Pan, W.-C. (1994). A study of the stress, strain and temperature distributions of a machined workpiece using a thermo-elastic-plastic coupled model. *Journal of Materials Processing Technology*, *41*(3), 291–310. https://doi.org/10.1016/0924-0136(94)90167-8

Liu, H., & Rao, J. (2009). Coupled Modeling of Electromagnetic-Thermal Problem in Induction Heating Process Considering Material Properties. *2009 International Conference on Information Engineering and Computer Science*, 1–4. https://doi.org/10.1109/ICIECS.2009.5363964

Lucía, Ó., Burdío, J. M., Barragán, L. A., Acero, J., & Millán, I. (2010). Series-Resonant Multiinverter for Multiple Induction Heaters. *IEEE Transactions on Power Electronics*, *25*(11), 2860–2868. https://doi.org/10.1109/TPEL.2010.2051041

Lucia, O., Maussion, P., Dede, E. J., & Burdio, J. M. (2014). Induction Heating Technology and Its Applications: Past Developments, Current Technology, and Future Challenges. *IEEE Transactions on Industrial Electronics*, *61*(5), 2509–2520. https://doi.org/10.1109/TIE.2013.2281162

Lupi, S. (2017). *Fundamentals of Electroheat*. Springer International Publishing. https://doi.org/10.1007/978-3-319-46015-4

Lupi, S., Forzan, M., & Aliferov, A. (2015). *Induction and Direct Resistance Heating: Theory and Numerical Modeling*. Springer International Publishing. https://doi.org/10.1007/978-3-319-03479-9

Ma, N., Deng, D., Osawa, N., Rashed, S., Murakawa, H., & Ueda, Y. (2022). *Welding deformation and residual stress prevention* (Second edition). Butterworth-Heinemann.

Majaty, Y. E., Leblond, J.-B., & Kondo, D. (2018). A novel treatment of Greenwood–Johnson's mechanism of transformation plasticity—Case of spherical growth of nuclei of daughter-phase. *Journal of the Mechanics and Physics of Solids*, *121*, 175–197. https://doi.org/10.1016/j.jmps.2018.07.014

Mandal, G., Dey, I., Mukherjee, S., & Ghosh, S. K. (2022). Phase transformation and mechanical properties of ultrahigh strength steels under continuous cooling conditions. *Journal of Materials Research and Technology*, *19*, 628–642. https://doi.org/10.1016/j.jmrt.2022.05.033

Mao, J., Keefer, V. L., Chang, K.-M., & Furrer, D. (2000). An Investigation on Quench Cracking Behavior of Superalloy Udimet 720LI Using a Fracture Mechanics Approach. *Journal of Materials Engineering and Performance*, *9*(2), 204–214. https://doi.org/10.1361/105994900770346169

Martín Segura, G., & Montesinos Miracle, D. (2012). *Induction heating converter's design, control and modeling applied to continuous wire heating* [Universitat Politècnica de Catalunya]. https://doi.org/10.5821/dissertation-2117-94610

Masserey, A., Rappaz, J., Rozsnyo, R., & Touzani, R. (2004). Power formulation for the optimal control of an industrial induction heating process for thixoforming. *International Journal*

of Applied Electromagnetics and Mechanics, *19*(1–4), 51–56. https://doi.org/10.3233/JAE-2004-535

Matsumura, O., Sakuma, Y., & Takechi, H. (1987). *TRIP AND ITS KINETIC ASPECTS IN AUSTEMPERED 0.4C-I.SSi-0.8Mn STEEL*.

Matsuoka, Y., Iwasaki, T., Nakada, N., Tsuchiyama, T., & Takaki, S. (2013). Effect of Grain Size on Thermal and Mechanical Stability of Austenite in Metastable Austenitic Stainless Steel. *ISIJ International*, *53*(7), 1224–1230. https://doi.org/10.2355/isijinternational.53.1224

Miyagi, D., Sai, A., Takahashi, N., Uchida, N., & Ozaki, K. (2006). Improvement of zone control induction heating equipment for high-speed processing of semiconductor devices. *IEEE Transactions on Magnetics*, *42*(2), 292–294. https://doi.org/10.1109/TMAG.2005.860823

Montalvo-Urquizo, J., Liu, Q., & Schmidt, A. (2013). Simulation of quenching involved in induction hardening including mechanical effects. *Computational Materials Science*, *79*, 639–649. https://doi.org/10.1016/j.commatsci.2013.06.058

Moravec, J., Mičian, M., Málek, M., & Švec, M. (2022). Determination of CCT Diagram by Dilatometry Analysis of High-Strength Low-Alloy S960MC Steel. *Materials*, *15*(13), 4637. https://doi.org/10.3390/ma15134637

Mosayebidorcheh, S., Ganji, D. D., & Farzinpoor, M. (2014). Approximate solution of the nonlinear heat transfer equation of a fin with the power-law temperature-dependent thermal conductivity and heat transfer coefficient. *Propulsion and Power Research*, *3*(1), 41–47. https://doi.org/10.1016/j.jppr.2014.01.005

Moumni, Z., Roger, F., & Trinh, N. T. (2011). Theoretical and numerical modeling of the thermomechanical and metallurgical behavior of steel. *International Journal of Plasticity*, *27*(3), 414–439. https://doi.org/10.1016/j.ijplas.2010.07.002

Mühlbauer, A. (Ed.). (2008). *History of induction heating and melting*. Vulkan-Verl.

Naar, R., & Bay, F. (2013). Numerical optimisation for induction heat treatment processes. *Applied Mathematical Modelling*, *37*(4), 2074–2085. https://doi.org/10.1016/j.apm.2012.04.058

Nagasaka, Y., Brimacombe, J. K., Hawbolt, E. B., Samarasekera, I. V., Hernandez-Morales, B., & Chidiac, S. E. (1993). Mathematical model of phase transformations and elastoplastic stress in the water spray quenching of steel bars. *Metallurgical Transactions A*, *24*(4), 795–808. https://doi.org/10.1007/BF02656501

Nagayama, K., Terasaki, T., Tanaka, K., Fischer, F. D., Antretter, T., Cailletaud, G., & Azzouz, F. (2001a). Mechanical properties of a Cr–Ni–Mo–Al–Ti maraging steel in the process of martensitic transformation. *Materials Science and Engineering: A*, *308*(1–2), 25–37. https://doi.org/10.1016/S0921-5093(00)01999-7

Nagayama, K., Terasaki, T., Tanaka, K., Fischer, F. D., Antretter, T., Cailletaud, G., & Azzouz, F. (2001b). Mechanical properties of a Cr–Ni–Mo–Al–Ti maraging steel in the process of martensitic transformation. *Materials Science and Engineering: A*, *308*(1–2), 25–37. https://doi.org/10.1016/S0921-5093(00)01999-7

Ngoc, H. P., Fujita, H., Ozaki, K., & Uchida, N. (2011). Phase Angle Control of High-Frequency Resonant Currents in a Multiple Inverter System for Zone-Control Induction Heating. *IEEE Transactions on Power Electronics*, *26*(11), 3357–3366. https://doi.org/10.1109/TPEL.2011.2146278

Oberkampf, W. L., & Trucano, T. G. (2002). Verification and validation in computational fluid dynamics. *Progress in Aerospace Sciences*.

Okudaira, S., & Matsuse, K. (2000). Power control of an adjustable frequency quasi-resonant inverter for dual frequency induction heating. *Proceedings IPEMC 2000. Third International Power Electronics and Motion Control Conference (IEEE Cat. No.00EX435)*, *2*, 968–973. https://doi.org/10.1109/IPEMC.2000.884645

Ollat, M., Militzer, M., Massardier, V., Fabregue, D., Buscarlet, E., Keovilay, F., & Perez, M. (2018). Mixed-mode model for ferrite-to-austenite phase transformation in dual-phase steel. *Computational Materials Science*, *149*, 282–290. https://doi.org/10.1016/j.commatsci.2018.02.052

Ono, Y., Zheng, C.-Q., Hamel, F. G., Charron, R., & Loong, C. A. (2002). Experimental investigations on monitoring and control of induction heating process for semi-solid alloys using the heating coil as sensor. *Measurement Science and Technology*, *13*(8), 1359–1365. https://doi.org/10.1088/0957-0233/13/8/326

Pant, M., Singh, I. V., & Mishra, B. K. (2010). Numerical simulation of thermo-elastic fracture problems using element free Galerkin method. *International Journal of Mechanical Sciences*, *52*(12), 1745–1755. https://doi.org/10.1016/j.ijmecsci.2010.09.008

Patil, T. M., & Bhadade, U. S. (2015). Induction heating as fluid geyser. *2015 International Conference on Industrial Instrumentation and Control (ICIC)*, 170–174. https://doi.org/10.1109/IIC.2015.7150732

Patterson, E. A., & Rowlands, R. E. (2008). Determining individual stresses thermoelastically. *The Journal of Strain Analysis for Engineering Design*, *43*(6), 519–527. https://doi.org/10.1243/03093247JSA358

Penha, R. N., Vatavuk, J., Couto, A. A., Pereira, S. A. D. L., De Sousa, S. A., & Canale, L. D. C. F. (2015). Effect of chemical banding on the local hardenability in AISI 4340 steel bar. *Engineering Failure Analysis*, *53*, 59–68. https://doi.org/10.1016/j.engfailanal.2015.03.024

Persson, A. (2004). Strain-based approach to crack growth and thermal fatigue life of hot work tool steels. *Scandinavian Journal of Metallurgy*, *33*(1), 53–64. https://doi.org/10.1111/j.1600-0692.2004.00678.x

Persson, A., Hogmark, S., & Bergström, J. (2005). Thermal fatigue cracking of surface engineered hot work tool steels. *Surface and Coatings Technology*, *191*(2–3), 216–227. https://doi.org/10.1016/j.surfcoat.2004.04.053

Pleshivtseva, Y., Baldan, M., Popov, A., Nikanorov, A., Rapoport, E., & Nacke, B. (2019). Effective methods for optimal design of induction coils on example of surface hardening. *COMPEL - The International Journal for Computation and Mathematics in Electrical and Electronic Engineering*, *39*(1), 90–99. https://doi.org/10.1108/COMPEL-05-2019-0216

Pleshivtseva, Y., Popov, A., & Pavlushin, A. (2022). New Approach to Optimization of Surface Induction Hardening Process. *2022 4th International Conference on Control Systems, Mathematical Modeling, Automation and Energy Efficiency (SUMMA)*, 525–530. https://doi.org/10.1109/SUMMA57301.2022.9974146

Pohjonen, A., Somani, M., & Porter, D. (2018). Modelling of austenite transformation along arbitrary cooling paths. *Computational Materials Science*, *150*, 244–251. https://doi.org/10.1016/j.commatsci.2018.03.052

Popov, A. (2019). Optimization of Heating Stage for Induction Hardening of Cylindrical Billets. *2019 XXI International Conference Complex Systems: Control and Modeling Problems (CSCMP)*, 237–241. https://doi.org/10.1109/CSCMP45713.2019.8976805

Porpandiselvi, S., & Vishwanathan, N. (2015). Three-leg inverter configuration for simultaneous dual-frequency induction hardening with independent control. *IET Power Electronics*, *8*(9), 1571–1582. https://doi.org/10.1049/iet-pel.2014.0290

Porter, D. A. (2009). *Phase transformations in metals and alloys* (K. E. Easterling & M. Y. Sherif, Eds.; Third edtion). CRC Press.

Post, J., Datta, K., & Beyer, J. (2008). A macroscopic constitutive model for a metastable austenitic stainless steel. *Materials Science and Engineering: A*, *485*(1–2), 290–298. https://doi.org/10.1016/j.msea.2007.07.084

Poyraz, O., & Ögel, B. (2020). Recrystallization, grain growth and austenite formation in cold rolled steels during intercritical annealing. *Journal of Materials Research and Technology*, *9*(5), 11263–11277. https://doi.org/10.1016/j.jmrt.2020.08.015

Prisco, U. (2018). Case microstructure in induction surface hardening of steels: An overview. *The International Journal of Advanced Manufacturing Technology*, *98*(9–12), 2619–2637. https://doi.org/10.1007/s00170-018-2412-0

Qin, X., Gao, K., Zhu, Z., Chen, X., & Wang, Z. (2017). Prediction and Optimization of Phase Transformation Region After Spot Continual Induction Hardening Process Using Response Surface Method. *Journal of Materials Engineering and Performance*, *26*(9), 4578–4594. https://doi.org/10.1007/s11665-017-2887-0

Radionov, A. A., & Karandaev, A. S. (Eds.). (2020). *Advances in Automation: Proceedings of the International Russian Automation Conference, RusAutoCon 2019, September 8-14, 2019, Sochi, Russia* (Vol. 641). Springer International Publishing. https://doi.org/10.1007/978-3-030-39225-3

Rapoport, E., & Pleshivtseva, Y. (Eds.). (2007). *Optimal control of induction heating processes*. CRC/Taylor & Francis.

Rebba, R., Mahadevan, S., & Huang, S. (2006). Validation and error estimation of computational models. *Reliability Engineering & System Safety*, *91*(10–11), 1390–1397. https://doi.org/10.1016/j.ress.2005.11.035

Rego, R., Löpenhaus, C., Gomes, J., & Klocke, F. (2018). Residual stress interaction on gear manufacturing. *Journal of Materials Processing Technology*, *252*, 249–258. https://doi.org/10.1016/j.jmatprotec.2017.09.017

Reza Eslami, M., Hetnarski, R. B., Ignaczak, J., Noda, N., Sumi, N., & Tanigawa, Y. (2013). *Theory of Elasticity and Thermal Stresses: Explanations, Problems and Solutions* (Vol. 197). Springer Netherlands. https://doi.org/10.1007/978-94-007-6356-2

Rhein, S., Utz, T., & Graichen, K. (2015). Optimal control of induction heating processes using FEM software. *2015 European Control Conference (ECC)*, 515–520. https://doi.org/10.1109/ECC.2015.7330595

Rodriguez, J. I., & Leeb, S. B. (2006). A Multilevel Inverter Topology for Inductively Coupled Power Transfer. *IEEE Transactions on Power Electronics*, *21*(6), 1607–1617. https://doi.org/10.1109/TPEL.2006.882965

Rodriguez, J. I., & Leeb, S. B. (2010). Nonresonant and Resonant Frequency-Selectable Induction-Heating Targets. *IEEE Transactions on Industrial Electronics*, *57*(9), 3095–3108. https://doi.org/10.1109/TIE.2009.2037676

Rohde, J., & Jeppsson, A. (2000). Literature review of heat treatment simulations with respect to phase transformation, residual stresses and distortion. *Scandinavian Journal of Metallurgy*, *29*(2), 47–62. https://doi.org/10.1034/j.1600-0692.2000.d01-6.x

Rudnev, V., Loveless, D., & Cook, R. L. (2003). *Handbook of Induction Heating, Second Edition*.

Rudnev, V., Totten, G. E., ASM International, & ASM International (Eds.). (2014). *Induction heating and heat treatment*. ASM International.

Sadeghipour, K., Dopkin, J. A., & Li, K. (1996). A computer aided finite element/experimental analysis of induction heating process of steel. *Computers in Industry*, *28*(3), 195–205. https://doi.org/10.1016/0166-3615(95)00072-0

Sahin, I., Höke, G., Çinici, H., Findik, T., Koralay, H., & Arabaci, U. (2019). Effects of subzero treatments on the mechanical properties of the SAE 4140 steel. *Materiali in Tehnologije*, *53*(4), 489–494. https://doi.org/10.17222/mit.2018.135

Samuel, A., & Prabhu, K. N. (2022a). Residual Stress and Distortion during Quench Hardening of Steels: A Review. *Journal of Materials Engineering and Performance*, *31*(7), 5161–5188. https://doi.org/10.1007/s11665-022-06667-x

Samuel, A., & Prabhu, K. N. (2022b). Residual Stress and Distortion during Quench Hardening of Steels: A Review. *Journal of Materials Engineering and Performance*, *31*(7), 5161–5188. https://doi.org/10.1007/s11665-022-06667-x

Sasayama, T., Yanamoto, Y., Funaji, S., & Ao, T. (2015). Theoretical and Numerical Examination of Equivalent Resistances in Zone-Control Induction Heating System. *IEEJ Journal of Industry Applications*, *4*(1), 67–73. https://doi.org/10.1541/ieejjia.4.67

Saunders, N., Guo, Z., Li, X., & Miodownik, A. P. (2004). *The Calculation of TTT and CCT diagrams for General Steels*.

Seif, M., Main, J., Weigand, J., Sadek, F., Choe, L., Zhang, C., Gross, J., Luecke, W., & McColskey, D. (2016). *Temperature-Dependent Material Modeling for Structural Steels: Formulation and Application* (NIST TN 1907; p. NIST TN 1907). National Institute of Standards and Technology. https://doi.org/10.6028/NIST.TN.1907

Semenov, M. Yu., Gavrilin, I. N., & Ryzhova, M. Yu. (2014). Computation-Based Analysis of the Methods of Hardening of Gears from Heat-Resistant Steels. *Metal Science and Heat Treatment*, *56*(1–2), 45–49. https://doi.org/10.1007/s11041-014-9700-6

Sherif, M. Y., Mateo, C. G., Sourmail, T., & Bhadeshia, H. K. D. H. (2004). Stability of retained austenite in TRIP-assisted steels. *Materials Science and Technology*, *20*(3), 319–322. https://doi.org/10.1179/026708304225011180

Silva, E. P., Pacheco, P. M. C. L., & Savi, M. A. (2005). Finite element analysis of the phase transformation effect in residual stresses generated by quenching in notched steel cylinders. *The Journal of Strain Analysis for Engineering Design*, *40*(2), 151–160. https://doi.org/10.1243/030932405X7755

Şimşir, C., & Gür, C. H. (2008a). 3D FEM simulation of steel quenching and investigation of the effect of asymmetric geometry on residual stress distribution. *Journal of Materials Processing Technology*, *207*(1–3), 211–221. https://doi.org/10.1016/j.jmatprotec.2007.12.074

Şimşir, C., & Gür, C. H. (2008b). A FEM based framework for simulation of thermal treatments: Application to steel quenching. *Computational Materials Science*, *44*(2), 588–600. https://doi.org/10.1016/j.commatsci.2008.04.021

Soleimani, M., Kalhor, A., & Mirzadeh, H. (2020). Transformation-induced plasticity (TRIP) in advanced steels: A review. *Materials Science and Engineering: A*, *795*, 140023. https://doi.org/10.1016/j.msea.2020.140023

Sönmez, Ö., Kaya, D., Буканин, B., & Ivanov, A. (2022). Numerical simulation of a magnetic induction coil for heat treatment of an AISI 4340 gear. *European Mechanical Science*, *6*(2), 129–137. https://doi.org/10.26701/ems.1027181

Spezzapria, M., Forzan, M., & Dughiero, F. (2016). Numerical Simulation of Solid–Solid Phase Transformations During Induction Hardening Process. *IEEE Transactions on Magnetics*, *52*(3), 1–4. https://doi.org/10.1109/TMAG.2015.2484388

Srivastava, A., Sinha, A. N., & Verma, S. K. (2022). A mini-review on numerical approach of microstructure prediction in eutectoid steel. *Materials Today: Proceedings*, *50*, 2241–2248. https://doi.org/10.1016/j.matpr.2021.09.504

Szychta, E., & Szychta, L. (2020). Comparative Analysis of Effectiveness of Resistance and Induction Turnout Heating. *Energies*, *13*(20), 5262. https://doi.org/10.3390/en13205262

Taleb, L., & Sidoroff, F. (2003). A micromechanical modeling of the Greenwood–Johnson mechanism in transformation induced plasticity. *International Journal of Plasticity*, *19*(10), 1821–1842. https://doi.org/10.1016/S0749-6419(03)00020-2

Tong, D., Gu, J., & Edward Totten, G. (2017). Numerical simulation of induction hardening of a cylindrical part based on multi-physics coupling. *Modelling and Simulation in Materials Science and Engineering*, *25*(3), 035009. https://doi.org/10.1088/1361-651X/aa5f7c

Tong, D., Gu, J., & Totten, G. E. (2018). Numerical investigation of asynchronous dual-frequency induction hardening of spur gear. *International Journal of Mechanical Sciences*, *142–143*, 1–9. https://doi.org/10.1016/j.ijmecsci.2018.04.036

Toparli, M., Sahin, S., Ozkaya, E., & Sasaki, S. (2002). Residual thermal stress analysis in cylindrical steel bars using finite element method and artificial neural networks. *Computers & Structures*, *80*(23), 1763–1770. https://doi.org/10.1016/S0045-7949(02)00215-8

Totik, Y., Sadeler, R., Altun, H., & Gavgali, M. (2003). The effects of induction hardening on wear properties of AISI 4140 steel in dry sliding conditions. *Materials & Design*, *24*(1), 25–30. https://doi.org/10.1016/S0261-3069(02)00099-7

Totten, G. E., Howes, M. A. H., & Inoue, T. (Eds.). (2002). *Handbook of residual stress and deformation of steel*. ASM International.

Trzaska, J., & Jagie, A. (2009). The calculation of CCT diagrams for engineering steels. *Archives of Materials Science and Engineering*, *39*(1).

Tudbury, C. (1974). Electromagnetics in induction heating. *IEEE Transactions on Magnetics*, *10*(3), 694–697. https://doi.org/10.1109/TMAG.1974.1058381

Van Bohemen, S. M. C., & Sietsma, J. (2009). Martensite Formation in Partially and Fully Austenitic Plain Carbon Steels. *Metallurgical and Materials Transactions A*, *40*(5), 1059–1068. https://doi.org/10.1007/s11661-009-9796-2

Vandijk, N., Butt, A., Zhao, L., Sietsma, J., Offerman, S., Wright, J., & Vanderzwaag, S. (2005). Thermal stability of retained austenite in TRIP steels studied by synchrotron X-ray diffraction during cooling. *Acta Materialia*, *53*(20), 5439–5447. https://doi.org/10.1016/j.actamat.2005.08.017

Wang, M., & Huang, M. X. (2020). Abnormal TRIP effect on the work hardening behavior of a quenching and partitioning steel at high strain rate. *Acta Materialia*, *188*, 551–559. https://doi.org/10.1016/j.actamat.2020.02.035

Wang, M.-M., Tasan, C. C., Ponge, D., & Raabe, D. (2016). Spectral TRIP enables ductile 1.1 GPa martensite. *Acta Materialia*, *111*, 262–272. https://doi.org/10.1016/j.actamat.2016.03.070

Wang, X., Meng, Q., Wang, Z., Gan, J., Yang, Y., Qin, X., Gao, K., Zhong, H., Cheng, M., & Gan, X. (2019). Prediction of the surface characteristic of 42CrMo after spot continual induction hardening based on a novel co-simulation method. *Surface and Coatings Technology*, *357*, 252–266. https://doi.org/10.1016/j.surfcoat.2018.09.088

Wetz, D., Landen, D., Satapathy, S., & Surls, D. (2011). Inductive heating of materials for the study of high temperature mechanical properties. *IEEE Transactions on Dielectrics and Electrical Insulation*, *18*(4), 1342–1351. https://doi.org/10.1109/TDEI.2011.5976137

Wolff, M., Böhm, M., Dalgic, M., Löwisch, G., Lysenko, N., & Rath, J. (2006). Parameter identification for a TRIP model with backstress. *Computational Materials Science*, *37*(1–2), 37–41. https://doi.org/10.1016/j.commatsci.2005.12.007

Wolff, M., Böhm, M., Dalgic, M., Löwisch, G., & Rath, J. (2007). Validation of a TP model with backstress for the pearlitic transformation of the steel 100Cr6 under step-wise loads. *Computational Materials Science*, *39*(1), 49–54. https://doi.org/10.1016/j.commatsci.2006.01.025

Wölfle, C. H., Krempaszky, C., & Werner, E. (2022). An implicit integration scheme with consistent tangent modulus for Leblond's model of transformation-induced plasticity in

steels. *Continuum Mechanics and Thermodynamics*, *34*(1), 321–340. https://doi.org/10.1007/s00161-021-01058-4

Zervos, A., Papanicolopulos, S.-A., & Vardoulakis, I. (2009). Two Finite-Element Discretizations for Gradient Elasticity. *Journal of Engineering Mechanics*, *135*(3), 203–213. https://doi.org/10.1061/(ASCE)0733-9399(2009)135:3(203)

Zhang, M.-X., & Kelly, P. M. (2009). The morphology and formation mechanism of pearlite in steels. *Materials Characterization*, *60*(6), 545–554. https://doi.org/10.1016/j.matchar.2009.01.001

Zhang, S., Liu, C., & Wang, X. (2019). Optimisation research on inductor shape parameters for thermal forming behaviour of ship hull plate by moving induction heating. *Ships and Offshore Structures*, *14*(8), 853–866. https://doi.org/10.1080/17445302.2019.1570740

Zhang, W., Yang, J., Xu, Y., & Gao, T. (2014). Topology optimization of thermoelastic structures: Mean compliance minimization or elastic strain energy minimization. *Structural and Multidisciplinary Optimization*, *49*(3), 417–429. https://doi.org/10.1007/s00158-013-0991-9

Zhe, X., & Sanqiang, P. (2013). Temperature optimal control of the casting billet induction heating process based on the BP prediction model. *2013 IEEE Symposium on Computational Intelligence in Control and Automation (CICA)*, 163–167. https://doi.org/10.1109/CICA.2013.6611678

Zhong, H., Wang, Z., Gan, J., Wang, X., Yang, Y., He, J., Wei, T., & Qin, X. (2020). Numerical simulation of martensitic transformation plasticity of 42CrMo steel based on spot continual induction hardening model. *Surface and Coatings Technology*, *385*, 125428. https://doi.org/10.1016/j.surfcoat.2020.125428

Zhu, H. L., Li, S. Y., & Wang, C. R. (2013). Numerical Simulation of Temperature Field of Gears in Quenching Process. *Applied Mechanics and Materials*, *457–458*, 566–570. https://doi.org/10.4028/www.scientific.net/AMM.457-458.566

Ziegler, H. (1959). A modification of Prager's hardening rule. *Quarterly of Applied Mathematics*, *17*(1), 55–65. https://doi.org/10.1090/qam/104405

List of publications

Publication in journals

1. **D. Desisa**, A. Smalcerz, V. Kotlan, J. Barglik, A. Smagor, and I. Dolezel, "Mathematical modelling of thermal stresses of induction surface hardening in axi-symmetric formulation," Surface and Coatings Technology, vol. 479, p. 130516, Mar. 2024, doi: 10.1016/j.surfcoat.2024.130516
2. A. Smalcerz, L. Blacha, B. Węcki, **D. G. Desisa**, J. Łabaj, and M. Jodkowski, "Elimination of Zinc from Aluminum During Remelting in a Vacuum Induction Furnace" 2022, doi: 10.24425/AFE.2022.140231.
3. J. Smoleń, K. Tomaszewska, **D. G. Desisa**, "Thermal Characterization of Cross-Linking Process in Unsaturated Polyester Resin Based Polymer Concrete" Research Journal of the Polish Society of Composite, COMPOSITE THEORY AND PRACTICE, p. 166-171, Oct. (2022). https://www.researchgate.net/publication/364225391_THERMAL
4. L. Blacha, A. Smalcerz, B. Wecki, J. Labaj, **D. G. Desisa**, and M. Jodkowski, "Comparative Analysis of Lead Removal from Liquid Copper by ICF and CCF Refining Technologies," Materials, vol. 15, no. 19, p. 7024, Oct. 2022, doi: 10.3390/ma15197024.
5. J. Barglik, A. Smagór, A. Smalcerz, and **D. G. Desisa**, "Induction Heating of Gear Wheels in Consecutive Contour Hardening Process," Energies, vol. 14, no. 13, p. 3885, Jun. 2021, doi: 10.3390/en14133885.
6. **Desisa D.G,** Shekata G.D, (2020) Performance Analysis of Flat-Plate and V-groove Solar Air Heater Through CFD Simulation. International Journal of Renewable Energy Development, 9(3), 369-381, https://doi.org/ 10.14710/ ijred.2020.30091.
7. **D. Desisa**, A. Smalcerz, V. Kotlan, I. Dolezel "FE Analysis of the Thermoelastic-Plastic Properties of AISI 4140 Steel" (in the process)

Publication in an international conference

1. J. Barglik, V. Kotlan, A. Smalcerz, A. Smagór, **D. Desisa**, and I. Doležzel, "An improved model of hardening gear wheels and determining the electrical efficiency of the process," 24th International Conference on Computational Problems of Electrical Engineering (CPEE), Grybów, Poland: IEEE, Sep. 2023, p. 1–4.

doi:10.1109/CPEE59623.2023.10285320

2. **D. Desisa,** "Numerical Modeling of Induction Heating Process Control," in 2022 22nd International Scientific Conference on Electric Power Engineering (EPE), Kouty nad Desnou, Czech Republic, Jun. 2022, p. 1–6. doi: 10.1109/EPE54603.2022.9814122.
3. J. Barglik, V. Kotlan, A. Smalcerz, I. Dolezel, **D. G. Desisa**, "Calibration of Model for Hardening Gear Wheels," 27th IFHTSE Congress & European Conference on Heat Treatment, Wyndham Grand Salzburg, Austria, September 5–8, 2022. https://www.scopus.com/record/display.uri?eid=2-s2.0-85170820591&origin=resultslist&sort
4. **Debela Desisa** and Vaclov Kotlan "Optima control of an induction heating processes: an approach using numerical analysis". Electrical engineering and informatics 2022.XIII, annual publication of doctor's works, Nov. 2022, Nectny Castle, Czeck Republic. P.9-12.
5. **D. Desisa,** J. Barglik, V. Kotlan, A. Smalcerz, A. Smagor and I. Dolezel," MODEL OF RESIDUAL STRESSES IN INDUCTIVELY HARDENED SURFACES," an international conference on heating by electromagnetic source (HES-23), Padua, Italy, May 9 – 12, 2023. Oral presentation.
6. A. D. Tura, H. B. Mamo, and **D. G. Desisa**, "Multi-objective optimization and analysis for laser beam cutting of stainless steel (SS304) using hybrid statistical tools GA-RSM," IOP Conference Series Material Science & Eng., vol. 1201, Nov. 2021, doi: 10.1088/1757 899X/1201/1/012030.

Appendix A

I) Shaft model

From heat transfer field the following equation was solved by the operator in COMSOL multiphysics

$$\rho C_p \frac{dT}{dt} + \rho C_p u \cdot \nabla T + \nabla \cdot q = Q + Q_{ted}$$

$$q = -k\nabla T$$

$-n \cdot q = 0$ at the symmetry axysis

On the surface of the workpiece,

$$-n \cdot q = q_0$$

$$q_0 = h(T_{ext} - T)$$

$$h = \frac{k}{D}\left(0.3 + \frac{0.62ReD^{1/2}Pr^{1/3}}{\left(1 + \left(\frac{0.4}{Pr}\right)^{2/3}\right)^{1/4}}\left(1 + \left(\frac{ReD}{282000}\right)^{5/8}\right)^{4/5}\right)$$

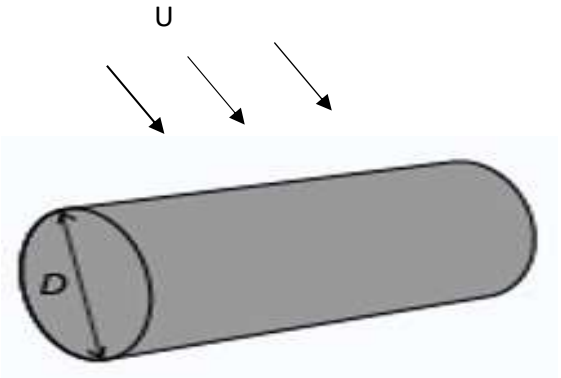

Figure A.1: 3D shaft under quench

Phase transformations:

$\dot{\xi}^i = \sum_i A_{i\to j}, i \neq j, i =$ Phase transformation

Averaging of phase properties:

$\rho = \sum_j \xi^j \rho^j, \rho = \{k, E, \nu, \sigma_h, \mu_r, \sigma, \epsilon_r\}, j =$ phase

$C_p = \frac{1}{\rho} \sum_i \xi^j \rho^j C_p^j$, $j =$ phase

$\sigma_{ys0} = \sum_j g_i(\xi^j)\sigma_{ys}^j$, $j =$ phase

Phase transformation latent heat:

$Q_0 = \sum_i Q_0^j$, $i =$ phase transformation

Phase transformation strain:

$\epsilon_{inel} = \sum_i \epsilon_{tp}^i + \sum_j \epsilon_{th}^j$, $i =$ phase transformation, $j =$ phase

$\epsilon_{th}^j = \xi^j \alpha^j \left(T - T_{ref}^j\right)$,

and linear isotropic hardening has computed

$\sigma_{ys} = \sigma_{ys} + E_{iso}\epsilon_{pe}$, $\frac{1}{E_{iso}} = \frac{1}{E_{Tiso}} - \frac{1}{E}$

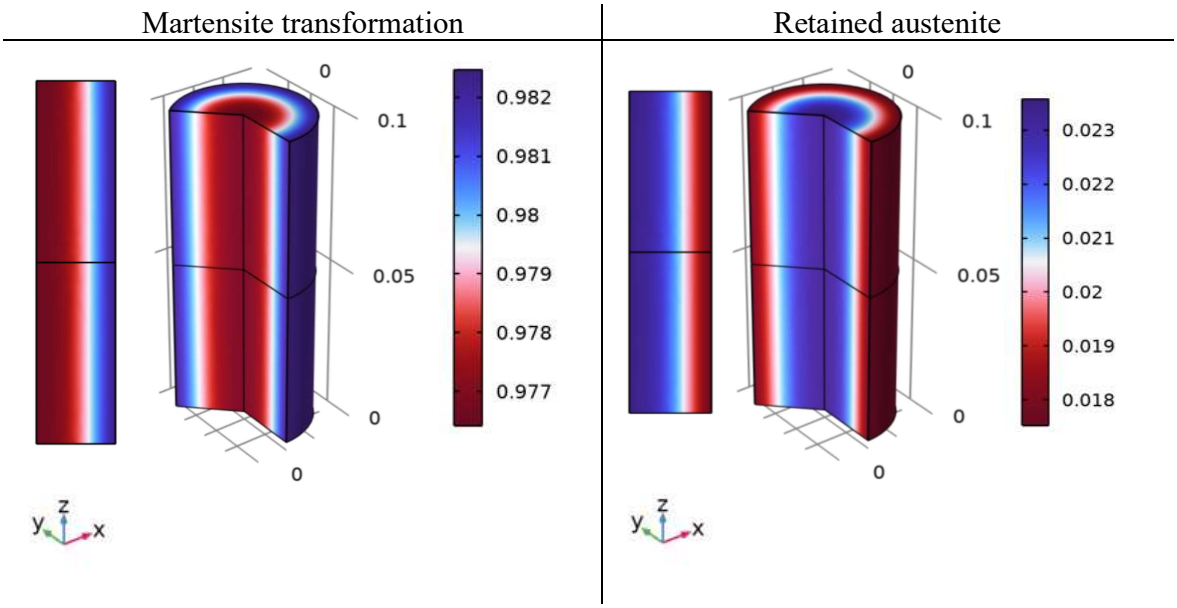

Figure A.2: present of martensite and retained austenite phase in 3D model contour

Effective thermal properties and mechanical properties were selected to be computed for the entire process. Under solid mechanics model command input, transformation induced plasticity, thermal stains and phase plasticity are enabled to be computed.

User controlled time dependent study was performed and under linear elasticity modeling the operator computes the following equations simultaneously where symmetry is in consideration.

$0 = \nabla \cdot S + F_V$

$u(R, \Phi, Z) \rightarrow (u, 0, w)^T$

$S = S_{inel} + S_{el}, \epsilon_{el} = \epsilon - \epsilon_{inel}$

$\epsilon_{inel} = \epsilon_0 + \epsilon_{ext} + \epsilon_{th} + \epsilon_{hs} + \epsilon_{pl} + \epsilon_{cr} + \epsilon_{vp} + \epsilon_{ve}$

$S_{el} = C : \epsilon_{el}$

$S_{inel} = S_0 + S_{ext} + S_q$

$\epsilon = \frac{1}{2}[(\nabla u)^T + \nabla u]$

$C = C(E, \nu)$

von Mises stress, Gauss point evaluation (N/m^2). For visibility, scale factor set to 10

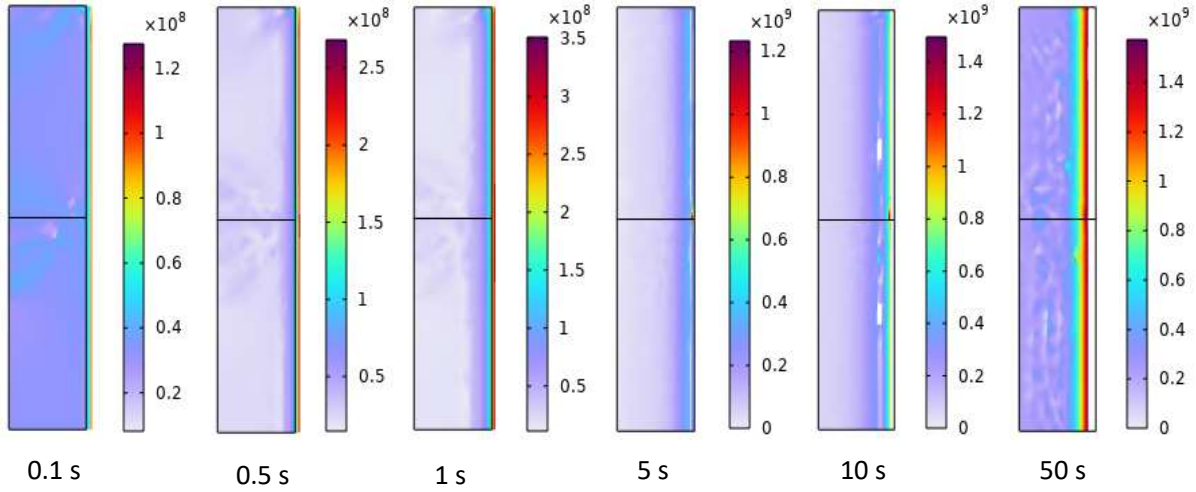

Figure A.3: Deformation due to thermal stress

II) Spur gear model

In the gear model, attention was given to temperature control methods. Among these methods, one involves defining the objective function, and introducing parameters, constraints, and objective function equations. Before conducting optimization, it is recommended to try it at a low computational cost using sweep analysis.

Step 1: Parameters were defined under global definition, geometry and materials also clearly defined at under component

Step 2: study setting includes parameters value list, units and name all involved in the study.

$$I \in \langle 200, 1000 \rangle \text{A}, f \in \langle 10, 50 \rangle \text{kHz}, \alpha \in \langle 4, 20 \rangle \text{W}/m^2\text{K},$$

Step 3: objective functions are defined

$$1/(at(1[s], comp1.ppb1) - at(1[s], comp1.ppb2))\text{^}2$$

$$at(1[s], comp1.ppb2) - 1073$$

The following lectromagnetic equetions were solved by operator in COMSOL Multiphysics

$$\nabla \times \boldsymbol{H} = \boldsymbol{J}$$

$$\boldsymbol{B} = \nabla \times \boldsymbol{A}$$

$$\boldsymbol{J} = \sigma \boldsymbol{E} + \boldsymbol{J}_e$$

Resulted in heat transfer phenomena.

$$\rho C_p u \cdot \nabla T + \nabla \cdot q = Q + Q_{ted}$$

$$q = -k\nabla T$$

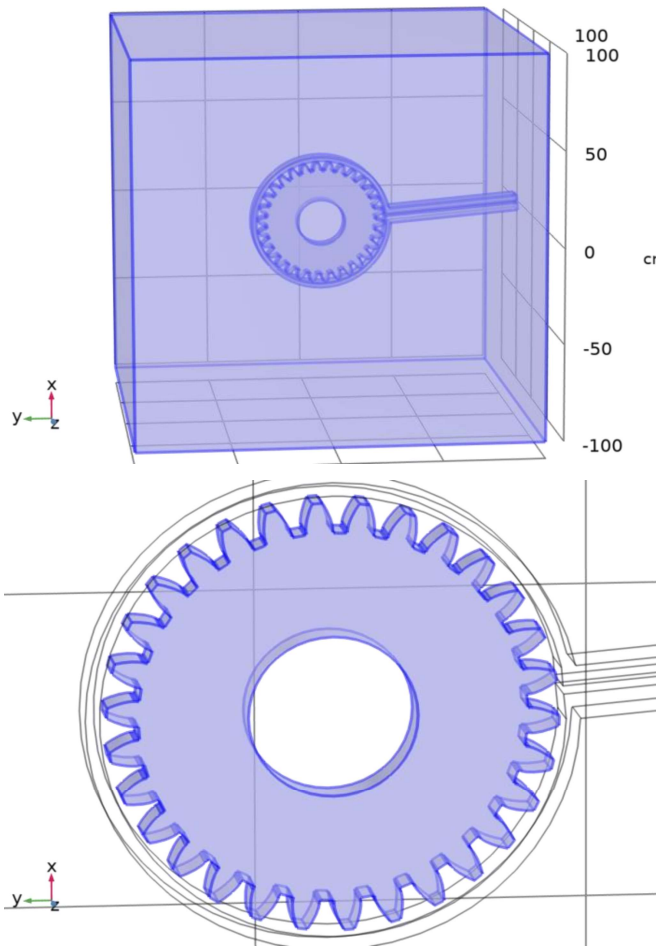

Figure A.4: 3D model setup with air domain

Appendix B

For each analysis and discussion in the document, the data was collected from post-processing using 'derived values' through point or line evaluation, as well as some parameters from global evaluation. A Similar approach was implemented for analysis other data.

Table B.1: Sample data; cooling temperature gradient and strain hardening function

Cooling (Quenching)				Strain-hardening function			
				surface		core	
Time (s)	Temperature (℃), core	Temperature (℃), surface	Temperature difference (℃),	with TRIP	without TRIP	with TRIP	without TRIP
0	900	893.73686	6.2631366	373823	342656	282024	282012
0.1	900.00003	714.4485	185.55152	809126	8182554	282249	2835520
0.2	899.99995	651.8454	248.15454	1.30E+08	1.29E+08	285203	2838954
0.3	899.99933	608.91085	291.08847	1.67E+08	1.67E+08	285175	2835002
0.4	900.00032	575.27384	324.72647	1.94E+08	1.90E+08	285164	2834370
0.5	900.00151	547.99287	352.00863	2.11E+08	2.07E+08	2851641	2834370
0.6	900.001	524.78267	375.21833	2.20E+08	2.22E+08	2851641	2834370
0.7	899.99889	504.34935	395.64954	2.31E+08	2.35E+08	2851825	2834370
0.8	899.99781	485.99215	414.00566	2.43E+08	2.47E+08	2852003	2837983
0.9	899.998	469.56548	430.43252	2.55E+08	2.57E+08	2851971	2841913
1	899.99962	454.78581	445.21381	2.64E+08	2.66E+08	2851703	2843497
1.1	900.00133	441.39206	458.60927	2.73E+08	2.75E+08	2851641	2842523
1.2	900.00253	429.25362	470.7489	2.80E+08	2.83E+08	2851641	2840524
1.3	900.00074	418.07626	481.92423	2.86E+08	2.91E+08	2851641	2837536
1.4	899.9962	407.84071	492.15549	2.92E+08	2.97E+08	2852270	2835104
1.5	899.98817	398.38484	501.60332	2.97E+08	3.04E+08	2853599	2834370
1.6	899.98114	389.50817	510.47296	3.03E+08	3.09E+08	2854764	2834370
1.7	899.97511	381.20975	518.76536	3.08E+08	3.15E+08	2855761	2834370
1.8	899.96973	373.51258	526.45715	3.13E+08	3.20E+08	2856653	2834370
1.9	899.96567	366.3954	533.57026	3.18E+08	3.24E+08	2857325	2834370
2	899.96553	359.77067	540.19486	3.20E+08	3.29E+08	2857348	2834370
2.1	899.97401	353.51034	546.46367	3.26E+08	3.33E+08	2855943	2834370
2.2	899.9936	347.6269	552.36672	4.69E+08	3.25E+08	2852685	2834370
2.3	900.02558	342.22148	557.80409	4.48E+08	3.02E+08	2851641	2834370
2.4	900.06948	337.23215	562.83732	4.22E+08	2.84E+08	2851641	2834370
2.5	900.12404	332.56849	567.55555	3.99E+08	2.69E+08	2851641	2834370
2.6	900.18688	328.18702	571.99985	3.79E+08	2.55E+08	2851641	2834370
2.7	900.25482	324.05917	576.19564	3.61E+08	2.43E+08	2851641	2834370
2.8	900.32402	320.1659	580.15812	3.44E+08	2.32E+08	2851641	2834370

2.9	900.39022	316.46111	583.9291	3.30E+08	2.22E+08	2851641	2834370
3	900.44885	312.92795	587.52089	3.16E+08	2.13E+08	2851641	2834370
3.1	900.49518	309.54715	590.94802	3.04E+08	2.05E+08	2851641	2834370
3.2	900.52447	306.30754	594.21692	2.92E+08	1.97E+08	2851641	2834370
3.3	900.53203	303.19293	597.3391	2.82E+08	1.90E+08	2851641	2834370
3.4	900.51328	300.19782	600.31545	2.72E+08	1.83E+08	2851641	2834370
3.5	900.46388	297.30378	603.1601	2.60E+08	1.75E+08	2851641	2834370
3.6	900.37971	294.50969	605.87002	2.48E+08	1.67E+08	2851641	2834370
3.7	900.25691	291.80615	608.45076	2.37E+08	1.60E+08	2851641	2834370
3.8	900.09195	289.18681	610.90513	2.28E+08	1.53E+08	2851641	2834370
3.9	899.88157	286.65207	613.22949	2.18E+08	1.47E+08	2871250	2834370
4	899.62286	284.18677	615.43609	2.10E+08	1.41E+08	2914090	2834370
4.1	899.31325	281.7907	617.52255	2.02E+08	1.36E+08	2965368	2864071
4.2	898.95046	279.46642	619.48403	1.94E+08	1.30E+08	3025466	2913881
4.3	898.5325	277.20356	621.32894	1.87E+08	1.26E+08	3094716	2972575
4.4	898.05769	274.99664	623.06104	1.80E+08	1.21E+08	3173405	3040490
4.5	897.52472	272.84972	624.675	1.74E+08	1.17E+08	3261758	3117920
4.6	896.93239	270.75602	626.17637	1.68E+08	1.13E+08	3359981	3205110
4.7	896.27994	268.70842	627.57152	1.63E+08	1.09E+08	3468211	3302253
4.8	895.56669	266.706	628.86069	1.57E+08	1.06E+08	3586571	3409495
4.9	894.79225	264.75518	630.03707	1.53E+08	1.02E+08	3715137	3526945
5	893.95642	262.85222	631.1042	1.48E+08	99118615	3853956	3654683
5.1	893.0592	260.98649	632.07271	1.43E+08	96087099	4003164	3792755
5.2	892.10073	259.12357	632.97715	1.39E+08	93145474	4163169	3941381
5.3	891.08129	257.30134	633.77995	1.35E+08	90356133	4334664	4101562
5.4	890.0013	255.52429	634.47706	1.31E+08	87709129	4517897	4273468
5.5	888.86146	253.78095	635.08051	1.27E+08	85188619	4711654	4456990
5.6	887.66229	252.06797	635.59431	1.24E+08	82786910	4912655	4650678
5.7	886.4046	250.3854	636.01919	1.20E+08	80493447	5105968	4848773
5.8	885.08923	248.7353	636.35392	1.17E+08	78302066	5315304	5055594
5.9	883.71702	247.12321	636.59381	1.14E+08	76208778	5572850	5266556
6	882.28908	245.54398	636.74509	1.11E+08	74202716	5859545	5477748
6.1	880.80622	243.98947	636.81674	1.08E+08	72279475	6138094	5697095
6.2	879.26997	242.45884	636.81113	1.05E+08	70441745	6418501	5952557
6.3	877.68124	240.95343	636.7278	1.03E+08	68682766	6703507	6240319
6.4	876.04119	239.47455	636.56663	1.00E+08	66992037	6996651	6542185
6.5	874.35086	238.02643	636.32442	97977428	65368696	7286161	6854787
6.6	872.61164	236.60798	636.00365	95687858	63812053	7600536	7179885
6.7	870.82463	235.21228	635.61234	93485722	62316534	7921717	7517055
6.8	868.99103	233.83603	635.155	91362433	60878398	8256646	7866216
6.9	867.11208	232.4794	634.63268	89315233	59497301	8640320	8231158
7	865.189	231.14179	634.0472	87340322	58169331	9038571	8606647
7.1	863.22306	229.82417	633.39888	85436349	56888060	9453121	8999385

7.2	861.21545	228.53086	632.68458	83606648	55650187	9896584	9395327
7.3	859.16736	227.26366	631.9037	81850760	54455013	1034356	9811373
7.4	857.07999	226.0185	631.06149	80160240	53300552	1082397	1023927
7.5	854.95452	224.79107	630.16345	78526923	52184275	1131564	1067092
7.6	852.79213	223.5801	629.21203	76947124	51104843	1180469	1112299
7.7	850.59378	222.38455	628.20923	75417768	50197666	1234755	1159206
7.8	848.36095	221.20308	627.15786	73935302	49859587	1292043	1206863
7.9	846.09471	220.03572	626.05898	72498218	49497172	1350301	1256573
8	843.79609	218.88451	624.91157	71107504	49143192	1407052	1308944
8.1	841.46616	217.752	623.71415	69764607	48822605	1462009	1364346
8.2	839.10599	216.63807	622.46791	68467688	48516260	1520013	1420925
8.3	836.71661	215.53971	621.17689	67211752	48189752	1577417	1478949
8.4	834.29886	214.45447	619.84439	65992829	47937866	1636039	1540533
8.5	831.85408	213.38208	618.472	64809249	47696066	1695784	1601110
8.6	829.38308	212.32334	617.05973	63660877	47418688	1755283	1662331
8.7	826.88666	211.27765	615.60901	62546010	47144357	1817393	1725682
8.8	824.36588	210.24365	614.12222	61462151	46897837	1879219	1788955
8.9	821.8215	209.22147	612.60002	60408556	46658213	1941714	1852015
9	819.25453	208.2124	611.04212	59385578	46393391	2006937	1915485
9.1	816.66579	207.21709	609.4487	58392943	46110006	2068993	1979428
9.2	814.05615	206.2345	607.82164	57428734	45900757	2130886	2045160
9.3	811.42649	205.26318	606.16331	56490692	45730785	2193429	2114864
9.4	808.77756	204.30262	604.47494	55577598	45507041	2259186	2184791
9.5	806.11012	203.35298	602.75714	54688899	45324816	2330144	2257841
9.6	803.42496	202.41411	601.01085	53823769	45132228	2412742	2330458
9.7	800.72281	201.48515	599.23766	52980775	44930696	2491949	2402401
9.8	798.00432	200.5651	597.43921	52158430	44750091	2576652	2477519
9.9	795.27021	199.6533	595.61691	51355600	44578191	2661487	2554464
10	792.52109	198.74999	593.77109	50572016	44489019	2746322	2633461
10.1	789.75757	197.85649	591.90108	49808275	44339242	2833505	2713404
10.2	786.98039	196.97384	590.00654	49064744	44226645	2922479	2792695
10.3	784.19018	196.1018	588.08837	48340674	44091002	3016534	2871270
10.4	781.38765	195.23888	586.14877	47634292	43950404	3111514	2952717
10.5	778.57338	194.38379	584.18958	46944140	43830877	3207112	3036682
10.6	775.74788	193.53612	582.21175	46269482	43748546	3300515	3121990
10.7	772.91156	192.69621	580.21535	45610214	43613873	3398630	3206664
10.8	770.06491	191.86434	578.20056	44966178	43546027	3504051	3294739
10.9	767.20849	191.04013	576.16835	44336711	43453351	3608328	3383448
11	764.34292	190.22287	574.12004	43720926	43299502	3721899	3469747
11.1	761.4687	189.41202	572.05668	43118103	43222524	3829349	3561405
11.2	758.58629	188.60753	569.97875	42527916	43097800	3925904	3653367
11.3	755.69605	187.80989	567.88616	41950427	43043868	4031062	3747210
11.4	752.79842	187.01974	565.77868	41385801	42987364	4136990	3846109

11.5	749.89393	186.23729	563.65664	40833876	42894184	4239132	3948002
11.6	746.98301	185.46223	561.52078	40294141	42784651	4345347	4050749
11.7	744.06604	184.69404	559.372	39765960	42728613	4454333	4156951
11.8	741.1433	183.93244	557.21086	39248875	42652468	4566800	4263226
11.9	738.21532	183.17749	555.03783	38742684	42644729	4681075	4378798
12	735.28268	182.42921	552.85347	38247151	42536840	4791161	4484241
12.1	732.34578	181.68717	550.6586	37761763	42532608	4891921	4598451
12.2	729.40483	180.95057	548.45425	37285780	42447160	4995424	4713246
12.3	726.45984	180.21858	546.24126	36818497	42423243	5099143	4835374
12.4	723.51108	179.49051	544.02056	36359285	42357232	5203509	4944681
12.5	720.55904	178.76615	541.79288	35907859	42340775	5300272	5065439
12.6	717.60413	178.04588	539.55824	35464312	42280485	5397141	5177091
12.7	714.64661	177.33063	537.31597	35029055	42227096	5499839	5295169
12.8	711.68657	176.62138	535.06518	34602505	42216000	5614626	5421259
12.9	708.72405	175.91852	532.80552	34184716	42100088	5743027	5541196
13	705.75932	175.22171	530.53761	33775288	42073689	5874674	5666148
13.1	702.7932	174.5303	528.2629	33373676	42023158	6010529	5793862
13.2	699.82597	173.8437	525.98227	32979384	41976876	6147573	5923969
13.3	696.85778	173.16156	523.69622	32592075	41923921	6285570	6052104
13.4	693.88881	172.48384	521.40497	32211580	41867480	6420372	6183072
13.5	690.91916	171.81055	519.10861	31837784	41808142	6564860	6319508
13.6	687.9489	171.14156	516.80734	31470489	41759969	6702038	6453644
13.7	684.97821	170.47658	514.50162	31109408	41709023	6830229	6586658
13.8	682.0074	169.81524	512.19216	30754232	41689664	6953210	6724821
13.9	679.03683	169.15722	509.87961	30404688	41650706	7083478	6869675
14	676.06689	168.50237	507.56451	30060601	41593548	7224644	7008156
14.1	673.09779	167.85083	505.24696	29721939	41529538	7377207	7145656
14.2	670.12947	167.20291	502.92655	29388776	41482753	7533024	7294501
14.3	667.16174	166.55899	500.60275	29061200	41449626	7686870	7435155
14.4	664.19453	165.91933	498.2752	28739243	41404505	7845617	7581869
14.5	661.22779	165.28406	495.94373	28422863	41332951	7997830	7724789
14.6	658.2618	164.65311	493.60868	28111927	41249026	8137570	7872553
14.7	655.29662	164.02629	491.27033	27806236	41176365	8274689	8005715
14.8	652.33233	163.40335	488.92898	27505578	41098173	8420867	8147231
14.9	649.36913	162.78408	486.58504	27209762	41066042	8568824	8297307
15	646.40735	162.16829	484.23906	26918624	41023640	8724452	8452665
15.1	643.44752	161.55565	481.89187	26631912	40932634	8888822	8602235
15.2	640.48994	160.94586	479.54408	26349419	40869209	9054560	8748050
15.3	637.53463	160.33867	477.19596	26070993	40793648	9214874	8906228
15.4	634.58123	159.73391	474.84732	25796474	40786454	9372365	9060058
15.5	631.62968	159.13143	472.49824	25525692	40716695	9527719	9214709
15.6	628.68018	158.53136	470.14882	25258682	40649525	9690511	9358466
15.7	625.73201	157.9338	467.79814	24995474	40595030	9862571	9515778

15.8	622.78489	157.33922	465.44567	24736087	40517955	1.00E+08	9665217
15.9	619.83943	156.74779	463.09164	24480641	40438763	1.02E+08	9819857
16	616.89553	156.15984	460.73569	24229183	40367642	1.04E+08	9960598
16.1	613.95356	155.5754	458.37815	23981656	40289132	1.06E+08	1.01E+08
16.2	611.0141	154.99438	456.01972	23737952	40228046	1.07E+08	1.03E+08
16.3	608.07739	154.41654	453.66085	23497918	40087666	1.09E+08	1.04E+08
16.4	605.1433	153.84165	451.30167	23261390	40013629	1.10E+08	1.06E+08
16.5	602.21204	153.2695	448.94254	23028243	39928503	1.12E+08	1.07E+08
16.6	599.28346	152.69989	446.58357	22798322	39856405	1.13E+08	1.09E+08
16.7	596.3577	152.13278	444.22492	22571569	39715370	1.13E+08	1.10E+08
16.8	593.43493	151.5681	441.86682	22347914	39651145	1.14E+08	1.10E+08
16.9	590.51536	151.00581	439.50955	22127285	39527811	1.15E+08	1.11E+08
17	587.59889	150.44581	437.15307	21909609	39420888	1.16E+08	1.12E+08
17.1	584.68506	149.88806	434.797	21694816	39341678	1.17E+08	1.13E+08
17.2	581.77344	149.33248	432.44096	21482843	39230423	1.18E+08	1.14E+08
17.3	578.86369	148.77908	430.08461	21273648	39129079	1.19E+08	1.15E+08
17.4	575.95583	148.22794	427.72788	21067219	39002688	1.20E+08	1.16E+08
17.5	573.05019	147.67919	425.37099	20863566	38892559	1.21E+08	1.17E+08
17.6	570.14761	147.13297	423.01463	20662699	38787832	1.22E+08	1.18E+08
17.7	567.24931	146.58938	420.65992	20464612	38690987	1.23E+08	1.19E+08
17.8	564.35613	146.04846	418.30766	20269280	38574799	1.24E+08	1.19E+08
17.9	561.46764	145.51014	415.9575	20076628	38451449	1.25E+08	1.20E+08
18	558.58282	144.9743	413.60851	19886582	38354379	1.25E+08	1.21E+08
18.1	555.70148	144.44081	411.26067	19699050	38222878	1.26E+08	1.22E+08
18.2	552.82435	143.9094	408.91486	19513937	38083026	1.27E+08	1.23E+08
18.3	549.95157	143.3802	406.57137	19331162	37982981	1.29E+08	1.23E+08
18.4	547.08273	142.85286	404.22986	19150663	37830463	1.30E+08	1.24E+08
18.5	544.21783	142.32738	401.89044	18972379	37732235	1.31E+08	1.25E+08
18.6	541.35707	141.80368	399.55338	18796251	37618650	1.32E+08	1.26E+08
18.7	538.50004	141.28167	397.21836	18622220	37456446	1.33E+08	1.27E+08
18.8	535.64656	140.76126	394.88529	18450231	37330324	1.34E+08	1.28E+08
18.9	532.79736	140.24239	392.55496	18280235	37219022	1.35E+08	1.29E+08
19	529.95365	139.72501	390.22864	18112192	37060640	1.36E+08	1.30E+08
19.1	527.116	139.20912	387.90687	17946089	36939853	1.37E+08	1.30E+08
19.2	524.28431	138.69474	385.58957	17781883	36818139	1.38E+08	1.31E+08
19.3	521.4581	138.18192	383.27618	17619577	36701548	1.39E+08	1.32E+08
19.4	518.63657	137.6707	380.96587	17459163	36613505	1.41E+08	1.33E+08
19.5	515.81931	137.16116	378.65814	17300636	36461217	1.42E+08	1.34E+08
19.6	513.00633	136.65336	376.35297	17143989	36344408	1.44E+08	1.35E+08
19.7	510.19736	136.14733	374.05002	16989222	36252453	1.45E+08	1.37E+08
19.8	507.39143	135.64304	371.74839	16836278	36137577	1.46E+08	1.38E+08
19.9	504.58799	135.1405	369.44748	16685145	35983300	1.47E+08	1.39E+08
20	501.78647	134.63968	367.14679	16535791	35916066	1.48E+08	1.40E+08

20.1	498.98598	134.14055	364.84543	16388182	35762845	1.49E+08	1.41E+08
20.2	496.18612	133.64307	362.54304	16242287	35632731	1.49E+08	1.42E+08
20.3	493.38789	133.14724	360.24065	16098081	35509785	1.50E+08	1.43E+08
20.4	490.59276	132.65304	357.93972	15955539	35408976	1.51E+08	1.45E+08
20.5	487.80034	132.16046	355.63988	15814634	35287570	1.52E+08	1.46E+08
20.6	485.00978	131.66945	353.34033	15675335	35095682	1.53E+08	1.47E+08
20.7	482.22271	131.17998	351.04272	15537614	34951288	1.54E+08	1.48E+08
20.8	479.44216	130.69203	348.75013	15401441	34827290	1.55E+08	1.49E+08
20.9	476.66924	130.20555	346.46369	15266781	34704098	1.56E+08	1.49E+08
21	473.9008	129.72056	344.1803	15133623	34508828	1.57E+08	1.50E+08
21.1	471.13258	129.23707	341.89551	15001952	34378840	1.58E+08	1.51E+08
21.2	468.3631	128.75509	339.60801	14871750	34191611	1.59E+08	1.52E+08
21.3	465.59412	128.27461	337.31951	14743000	34055273	1.60E+08	1.53E+08
21.4	462.82689	127.79566	335.03123	14615688	33895760	1.61E+08	1.54E+08
21.5	460.06055	127.31823	332.74231	14489795	33712573	1.62E+08	1.55E+08
21.6	457.29396	126.84231	330.45165	14365300	33544137	1.64E+08	1.55E+08
21.7	454.52583	126.36787	328.15795	14242179	33403975	1.65E+08	1.56E+08
21.8	451.75699	125.89489	325.86209	14120411	33234935	1.67E+08	1.56E+08
21.9	448.99307	125.42335	323.56972	13999972	33085383	1.68E+08	1.57E+08
22	446.23742	124.95322	321.2842	13880839	32916623	1.69E+08	1.58E+08
22.1	443.48713	124.4844	319.00267	13762987	32749105	1.70E+08	1.59E+08
22.2	440.73564	124.01703	316.71861	13646390	32582797	1.72E+08	1.59E+08
22.3	437.97831	123.55088	314.42743	13531021	32417666	1.74E+08	1.60E+08
22.4	435.21119	123.08597	312.12522	13416855	32253680	1.76E+08	1.61E+08
22.5	432.43247	122.62226	309.8102	13303868	32090819	1.76E+08	1.61E+08
22.6	429.64435	122.15973	307.48462	13192047	31929071	1.77E+08	1.62E+08
22.7	426.8502	121.69837	305.15182	13081376	31768430	1.78E+08	1.63E+08
22.8	424.05006	121.23818	302.81187	12971831	31608893	1.78E+08	1.64E+08
22.9	421.24046	120.77916	300.4613	12863403	31450457	1.79E+08	1.65E+08
23	418.41865	120.32131	298.09734	12756082	31293115	1.79E+08	1.66E+08
23.1	415.58679	119.86464	295.72214	12649859	31136855	1.80E+08	1.67E+08
23.2	412.74998	119.40913	293.34084	12544717	30981666	1.80E+08	1.68E+08
23.3	409.91296	118.95476	290.9582	12440634	30827534	1.81E+08	1.70E+08
23.4	407.0766	118.50152	288.57507	12337599	30674446	1.81E+08	1.71E+08
23.5	404.23735	118.0494	286.18795	12235597	30522390	1.82E+08	1.73E+08
23.6	401.38843	117.59838	283.79004	12134614	30371354	1.83E+08	1.74E+08
23.7	398.52176	117.14846	281.3733	12034637	30221323	1.86E+08	1.75E+08
23.8	395.63063	116.69963	278.931	11935654	30072282	1.90E+08	1.77E+08
23.9	392.71559	116.25188	276.46371	11837649	29924214	1.94E+08	1.78E+08
24	389.78525	115.80518	273.98006	11740611	29777106	1.96E+08	1.79E+08
24.1	386.84575	115.35954	271.48621	11644522	29630947	1.98E+08	1.80E+08
24.2	383.89916	114.91493	268.98423	11549372	29485727	1.99E+08	1.82E+08
24.3	380.94213	114.47134	266.47078	11455148	29341440	2.02E+08	1.84E+08

24.4	377.94716	114.02879	263.91836	11361841	29198077	2.04E+08	1.86E+08
24.5	374.8825	113.58727	261.29523	11269440	29055630	2.06E+08	1.89E+08
24.6	371.73976	113.14677	258.59299	11177937	28914089	2.08E+08	1.91E+08
24.7	368.51699	112.7073	255.80968	11087322	28773444	2.11E+08	1.94E+08
24.8	365.21535	112.26885	252.9465	10997583	28633686	2.14E+08	1.96E+08
24.9	361.8504	111.83141	250.01899	10908708	28494802	2.17E+08	1.98E+08
25	358.43822	111.39497	247.04324	10820682	28356785	2.25E+08	2.05E+08
25.1	354.99213	110.95952	244.0326	10733498	28219623	2.29E+08	2.07E+08
25.2	351.52921	110.52506	241.00414	10647148	28083307	2.26E+08	2.05E+08
25.3	348.06782	110.09159	237.97622	10561621	27947848	2.17E+08	1.98E+08
25.4	344.62372	109.65909	234.96462	10476908	27813305	2.09E+08	1.90E+08
25.5	341.20952	109.22754	231.98197	10392989	27679573	2.01E+08	1.83E+08
25.6	337.83411	108.79694	229.03716	10309860	27546554	1.93E+08	1.76E+08
25.7	334.50307	108.36729	226.13578	10227510	27414315	1.86E+08	1.69E+08
25.8	331.21951	107.93856	223.28095	10145929	27282853	1.79E+08	1.63E+08
25.9	327.98575	107.51074	220.475	10065107	27152159	1.73E+08	1.57E+08
26	324.80266	107.08383	217.71883	9985031	27022220	1.66E+08	1.51E+08
26.1	321.67036	106.6578	215.01256	9905692	26893032	1.60E+08	1.45E+08
26.2	318.58926	106.23264	212.35661	9827081	26764579	1.55E+08	1.40E+08
26.3	315.55948	105.80835	209.75112	9749189	26636858	1.50E+08	1.35E+08
26.4	312.58073	105.3849	207.19582	9672004	26509849	1.44E+08	1.31E+08
26.5	309.65213	104.96229	204.68984	9595516	26383554	1.40E+08	1.26E+08
26.6	306.77113	104.54047	202.23065	9519712	26257947	1.35E+08	1.22E+08
26.7	303.93695	104.11945	199.8175	9444584	26133034	1.31E+08	1.18E+08
26.8	301.14938	103.69922	197.45015	9370126	26008788	1.27E+08	1.15E+08
26.9	298.40511	103.27975	195.12535	9296323	25885214	1.22E+08	1.10E+08
27	295.70579	102.86106	192.84473	9223178	25762276	1.17E+08	1.06E+08
27.1	293.04746	102.44312	190.60434	9150674	25639980	1.12E+08	1.01E+08
27.2	290.4274	102.02589	188.4015	9078800	25518323	1.07E+08	97074511
27.3	287.84779	101.60941	186.23838	9007559	25397302	1.03E+08	93112136
27.4	285.30541	101.19363	184.11178	8936929	25276893	99049068	89343447
27.5	282.80133	100.77855	182.02277	8866913	25157097	95186848	85776170
27.6	280.33454	100.36418	179.97036	8797503	25037918	91535628	82414328
27.7	277.90168	99.950483	177.9512	8728682	24919349	88061047	79249968
27.8	275.50458	99.537467	175.96711	8660455	24801355	84774618	76211842
27.9	273.14032	99.125115	174.0152	8592807	24683951	81650263	73336090
28	270.80819	98.713422	172.09476	8525733	24567136	78678980	70618772
28.1	268.50905	98.302395	170.20665	8459232	24450900	75863406	68042457
28.2	266.23905	97.892015	168.34704	8393288	24335225	73172936	65572309
28.3	263.99996	97.482291	166.51767	8327905	24220120	70616964	63228851
28.4	261.78984	97.073231	164.71661	8263073	24105582	68179275	61009113
28.5	259.60573	96.664849	162.94088	8198784	23991602	65837542	58890287
28.6	257.44946	96.257137	161.19232	8135038	23878176	63601738	56861581

28.7	255.32103	95.850095	159.47094	8071831	23765304	61469489	54932774
28.8	253.22045	95.443722	157.77673	8009162	23652984	59438473	53101599
28.9	251.14695	95.038034	156.10891	7947024	23541216	57502366	51342681
29	249.09631	94.633109	154.4632	7885415	23429995	55636944	49661044
29.1	247.07178	94.228887	152.84289	7824332	23319319	53857558	48059011
29.2	245.073	93.825367	151.24798	7763772	23209187	52162322	46533524
29.3	243.10101	93.42255	149.67846	7703732	23099609	50549393	45062287
29.4	241.15199	93.020506	148.13148	7644208	22990575	49003299	43656501
29.5	239.2236	92.619304	146.60433	7585199	22882082	47509708	42314761
29.6	237.31888	92.218867	145.10002	7526700	22774135	46081788	41030785
29.7	235.43774	91.819196	143.61854	7468708	22666744	44718150	39793345
29.8	233.5802	91.420292	142.15991	7411221	22559897	43417434	38609003
29.9	231.74199	91.022307	140.71968	7354240	22453592	42161395	37476653
30	229.92365	90.625222	139.29843	7297762	22347841	40951366	36387975
30.1	228.12668	90.228983	137.8977	7241782	22242648	39792165	35339615
30.2	226.35107	89.83359	136.51748	7186295	22138002	38682753	34334694
30.3	224.59683	89.439044	135.15778	7131300	22033899	37622112	33372327
30.4	222.85871	89.045601	133.81311	7076806	21930360	36591044	32443109
30.5	221.13996	88.653102	132.48685	7022800	21827374	35600162	31549177
30.6	219.44068	88.261542	131.17914	6969281	21724936	34649074	30691106
30.7	217.76088	87.87092	129.88996	6916244	21623046	33736991	29867533
30.8	216.09958	87.481297	128.61828	6863690	21521735	32860148	29070204
30.9	214.45375	87.092857	127.3609	6811624	21420980	32008590	28303218
31	212.8258	86.705453	126.12035	6760036	21320778	31189153	27565988
31.1	211.21573	86.319086	124.89664	6708922	21221138	30401220	26855846
31.2	209.62352	85.933755	123.68977	6658281	21122078	29644184	26168525
31.3	208.04765	85.549573	122.49808	6608110	21023580	28912479	25506508
31.4	206.48733	85.166597	121.32073	6558410	20925640	28203146	24869317
31.5	204.94373	84.78474	120.15899	6509174	20828275	27519521	24253425
31.6	203.41686	84.404004	119.01286	6460400	20731489	26861123	23657644
31.7	201.90673	84.024387	117.88234	6412084	20635268	26227480	23083123
31.8	200.41033	83.646105	116.76422	6364232	20539610	25611966	22529470
31.9	198.92861	83.269091	115.65951	6316839	20444538	25016186	21992606
32	197.46223	82.893297	114.56893	6269900	20350040	24441149	21473585
32.1	196.01121	82.518722	113.49248	6223411	20256110	23886479	20972548
32.2	194.57536	82.145379	112.42998	6177369	20162748	23351506	20488608
32.3	193.15146	81.773513	111.37795	6131780	20069982	22829950	20016363
32.4	191.74168	81.402958	110.33872	6086635	19977790	22325551	19558758
32.5	190.34603	81.033715	109.31231	6041931	19922869	21838008	19115538
32.6	188.96449	80.665784	108.29871	5997664	19861304	21367021	18686452
32.7	187.59627	80.29923	107.29704	5953834	19797255	20910875	18271253
32.8	186.23982	79.934176	106.30565	5910439	19734170	20466666	17869697
32.9	184.89651	79.570513	105.32599	5867474	19672038	20036528	17481546

33	183.56632	79.208241	104.35808	5824937	19602771	19620218	17103639
33.1	182.24927	78.84736	103.40191	5782823	19538566	19217499	16736054
33.2	180.94405	78.487975	102.45607	5741131	19485102	18826001	16380129
33.3	179.65041	78.130104	101.5203	5699857	19423550	18445161	16035662
33.4	178.36908	77.773691	100.59539	5658998	19362477	18075960	15702458
33.5	177.10006	77.418734	99.681328	5618551	19301878	17718205	15380323
33.6	175.84335	77.065235	98.778116	5578513	19241753	17371703	15069067
33.7	174.59595	76.713375	97.882579	5538872	19167814	17032052	14763449
33.8	173.35925	76.36307	96.996184	5499628	19121658	16701087	14466370
33.9	172.13363	76.014297	96.119332	5460781	19062065	16379195	14178244
34	170.91907	75.667056	95.252023	5422328	19002792	16066230	13898922
34.1	169.7156	75.321347	94.394255	5384265	18943837	15762048	13628259
34.2	168.5232	74.977171	93.54603	5346591	18885200	15466508	13366111
34.3	167.34187	74.634526	92.707348	5309301	18831900	15179471	13111786
34.4	166.17162	74.293414	91.878208	5272395	18749121	14900799	12861903
34.5	165.01244	73.953834	91.05861	5235868	18711189	14630357	12619103
34.6	163.86296	73.615851	90.24711	5199710	18653823	14366479	12383272
34.7	162.72206	73.279519	89.44255	5163911	18596773	14107845	12154299
34.8	161.59156	72.944751	88.646815	5128479	18540039	13856356	11932074
34.9	160.47145	72.611547	87.859904	5093413	18483620	13611899	11716489
35	159.36172	72.279908	87.081818	5058709	18426035	13374362	11506260
35.1	158.26239	71.949834	86.312556	5024365	18346518	13143637	11300205
35.2	157.17344	71.621324	85.552119	4990378	18316159	12919617	11099722
35.3	156.09488	71.29438	84.8005	4956746	18260951	12702195	10904725
35.4	155.02671	70.968999	84.057718	4923466	18206049	12491267	10715129
35.5	153.9648	70.645338	83.319469	4890505	18151453	12282654	10530850
35.6	152.91187	70.323295	82.588576	4857881	18097164	12078998	10351805
35.7	151.86834	70.002853	81.86549	4825594	18035786	11880650	10176416
35.8	150.83422	69.684013	81.150211	4793643	17981425	11687528	10004876
35.9	149.80951	69.366774	80.442738	4762025	17935946	11499553	9837766
36	148.7942	69.051136	79.743071	4730737	17882788	11316649	9675022
36.1	147.78831	68.7371	79.051211	4699778	17829923	11138738	9516577
36.2	146.79182	68.424665	78.367158	4669144	17777350	10965744	9362367
36.3	145.80325	68.11386	77.689397	4638821	17725070	10796435	9212327
36.4	144.82109	67.804713	77.016378	4608791	17660412	10629581	9064765
36.5	143.84745	67.497184	76.350273	4579073	17621228	10466796	8920703
36.6	142.88235	67.191272	75.691084	4549664	17569722	10308021	8780201
36.7	141.92578	66.886979	75.03881	4520563	17518490	10153197	8643208
36.8	140.97775	66.584304	74.393451	4491766	17467535	10002269	8509671
36.9	140.03825	66.283246	73.755008	4463272	17416857	9855178	8379541
37	139.10728	65.983807	73.12348	4435079	17369669	9711869	8252539
37.1	138.18485	65.685985	72.49886	4407185	17299061	9572288	8127649
37.2	137.26791	65.389766	71.878143	4379550	17266494	9434384	8005687

37.3	136.35834	65.09516	71.263183	4352197	17216936	9299370	7886611
37.4	135.45656	64.802168	70.654396	4325128	17167658	9167473	7770382
37.5	134.56257	64.51079	70.051782	4298340	17118660	9038649	7656959
37.6	133.67636	64.221027	69.45534	4271833	17069942	8912858	7546301
37.7	132.79794	63.932878	68.865071	4245604	17019464	8790055	7437931
37.8	131.92731	63.646343	68.280974	4219652	16951845	8670199	7331516
37.9	131.06447	63.361422	67.70305	4193973	16925323	8553249	7227495
38	130.20839	63.078085	67.130312	4168553	16877649	8438601	7125835
38.1	129.35782	62.796294	66.561534	4143371	16830245	8325526	7026503
38.2	128.5144	62.516097	65.998302	4118448	16783111	8214906	6929469
38.3	127.67811	62.237495	65.440617	4093784	16736248	8106708	6834701
38.4	126.84896	61.960488	64.888479	4069376	16682927	8000899	6741619
38.5	126.02696	61.685076	64.341888	4045223	16636573	7897448	6650345
38.6	125.2121	61.411259	63.800843	4021323	16597263	7796322	6561049
38.7	124.40438	61.139036	63.265345	3997675	16551477	7697492	6473707
38.8	123.6038	60.868408	62.735394	3974276	16505963	7600925	6388291
38.9	122.80812	60.59925	62.208877	3951088	16460721	7505552	6304776
39	122.01865	60.331635	61.687017	3928132	16415751	7411958	6223138
39.1	121.23575	60.065583	61.170169	3905412	16360062	7320296	6142707
39.2	120.45942	59.801093	60.658331	3882926	16318513	7230540	6063920
39.3	119.68967	59.538167	60.151503	3860672	16282062	7142665	5986774
39.4	118.92649	59.276805	59.649687	3838650	16237992	7056647	5911248
39.5	118.16988	59.017005	59.15288	3816858	16194169	6972463	5837321
39.6	117.41985	58.758768	58.661085	3795294	16150594	6890089	5764973
39.7	116.67578	58.502044	58.173738	3773944	16109293	6809223	5694072
39.8	115.93675	58.246756	57.69	3752787	16049645	6729432	5624250
39.9	115.20388	57.992995	57.210886	3731845	16021204	6651205	5555815
40	114.47716	57.740763	56.736397	3711117	15978534	6574521	5488748
40.1	113.75659	57.490059	56.266532	3690602	15936100	6499362	5423034
40.2	113.04217	57.240883	55.801292	3670298	15893903	6425708	5358654
40.3	112.33391	56.993235	55.340676	3650204	15851944	6353542	5295594
40.4	111.6318	56.747116	54.884685	3630319	15808136	6282845	5233640
40.5	110.93584	56.502524	54.433319	3610641	15751110	6213599	5172687
40.6	110.24413	56.259295	53.984839	3591137	15727459	6145197	5112898
40.7	109.55769	56.017517	53.540178	3571824	15686437	6077946	5054262
40.8	108.87691	55.777224	53.099685	3552706	15645654	6011948	4996762
40.9	108.20177	55.538416	52.663361	3533783	15605108	5947191	4940386
41	107.53229	55.301092	52.231205	3515053	15564802	5883658	4885121
41.1	106.86846	55.065253	51.803216	3496514	15518928	5821337	4830535
41.2	106.21029	54.830898	51.379396	3478167	15464363	5760212	4776767
41.3	105.55777	54.598028	50.959744	3460009	15445008	5700269	4723930
41.4	104.91029	54.366574	50.543718	3442028	15405506	5641332	4672013
41.5	104.26675	54.136412	50.130347	3424204	15366223	5583103	4621004

41.6	103.62842	53.907684	49.720737	3406558	15327159	5525901	4570895
41.7	102.99527	53.680388	49.31489	3389090	15288314	5469715	4521675
41.8	102.36733	53.454526	48.912804	3371797	15249689	5414534	4473333
41.9	101.74457	53.230097	48.514481	3354680	15211285	5360346	4425859
42	101.12702	53.007101	48.119919	3337736	15173102	5307140	4379244
42.1	100.51465	52.785537	47.729119	3320965	15135141	5254906	4333478
42.2	99.907489	52.565407	47.342082	3304367	15097403	5203631	4288551
42.3	99.304078	52.346498	46.957579	3287910	15059887	5152964	4244454
42.4	98.705128	52.128913	46.576215	3271607	15023888	5103066	4201059
42.5	98.110982	51.912704	46.198278	3255467	14973626	5054010	4158113
42.6	97.52164	51.69787	45.82377	3239486	14941392	5005786	4115909
42.7	96.937101	51.484411	45.45269	3223665	14911630	4958386	4074440
42.8	96.357365	51.272327	45.085038	3208002	14875074	4911800	4033698
42.9	95.782433	51.061618	44.720815	3192496	14838729	4866020	3993674
43	95.212305	50.852285	44.360019	3177148	14802596	4821037	3954361
43.1	94.646566	50.644255	44.002311	3161946	14766676	4776754	3915750
43.2	94.084334	50.437373	43.64696	3146870	14730969	4732977	3877835
43.3	93.526565	50.231808	43.294757	3131941	14695475	4689904	3840607
43.4	92.973261	50.027558	42.945702	3117158	14660195	4647526	3804059
43.5	92.424419	49.824625	42.599794	3102520	14625131	4605838	3768184
43.6	91.880042	49.623007	42.257034	3088027	14593150	4564832	3732903
43.7	91.340128	49.422706	41.917422	3073677	14546653	4524502	3697776
43.8	90.804678	49.22372	41.580957	3059469	14508006	4484839	3663220
43.9	90.273691	49.02605	41.247641	3045404	14486652	4445838	3629229
44	89.745242	48.829291	40.91595	3031435	14452519	4407146	3595797
44.1	89.220181	48.633622	40.586558	3017582	14418588	4368915	3562919
44.2	88.69904	48.439155	40.259885	3003856	14384861	4331233	3530588
44.3	88.181819	48.245889	39.93593	2990258	14351337	4294096	3498799
44.4	87.668518	48.053825	39.614693	2976785	14318018	4257499	3467546
44.5	87.159137	47.862962	39.296175	2963438	14284903	4221435	3436825
44.6	86.653676	47.673301	38.980375	2950215	14251994	4185901	3406628
44.7	86.152135	47.484842	38.667293	2937117	14219291	4150892	3376952
44.8	85.654514	47.297584	38.356929	2924142	14190920	4116401	3347790
44.9	85.160813	47.111528	38.049284	2911290	14147934	4082425	3318725
45	84.671032	46.926674	37.744357	2898560	14105260	4048958	3290106
45.1	84.185171	46.743021	37.442149	2885952	14090082	4015996	3261928
45.2	83.703229	46.56057	37.142659	2873465	14058222	3983534	3234187
45.3	83.225208	46.379321	36.845887	2861098	14026552	3951567	3206879
45.4	82.751107	46.199273	36.551834	2848851	13995071	3920090	3179999
45.5	82.280925	46.020426	36.260498	2836723	13963781	3889099	3153543
45.6	81.814664	45.842782	35.971882	2824714	13932680	3858589	3127507
45.7	81.350277	45.665923	35.684354	2812778	13901771	3828263	3101888
45.8	80.888811	45.490063	35.398748	2800938	13871054	3798270	3076680

45.9	80.430954	45.31534	35.115613	2789208	13840529	3768703	3051881
46	79.976703	45.141756	34.834946	2777588	13810196	3739560	3027486
46.1	79.526061	44.969311	34.55675	2766078	13775592	3710837	3003224
46.2	79.079026	44.798003	34.281023	2754676	13736164	3682529	2979278
46.3	78.6356	44.627833	34.007766	2743382	13713312	3654633	2955680
46.4	78.195781	44.458802	33.736978	2732195	13690298	3627146	2932428
46.5	77.759569	44.290909	33.46866	2721116	13660768	3600064	2909519
46.6	77.326966	44.124154	33.202811	2710144	13631417	3573383	2886949
46.7	76.89797	43.958537	32.939433	2699277	13602247	3547100	2864716
46.8	76.472582	43.794058	32.678523	2688516	13573256	3521211	2842816
46.9	76.050801	43.630717	32.420084	2677860	13544447	3495712	2821246
47	75.632629	43.468515	32.164114	2667309	13515819	3470601	2800004
47.1	75.218064	43.307451	31.910613	2656861	13487373	3445874	2779086
47.2	74.807107	43.147524	31.659582	2646517	13459109	3421527	2758490
47.3	74.399758	42.988736	31.411021	2636277	13428300	3397557	2738042
47.4	73.993231	42.830475	31.162756	2626080	13391889	3373619	2717819
47.5	73.588805	42.673021	30.915783	2615954	13369533	3349869	2697876
47.6	73.187545	42.516609	30.670935	2605921	13347397	3326436	2678209
47.7	72.789451	42.361238	30.428212	2595980	13319884	3303319	2658817
47.8	72.394523	42.206908	30.187615	2586131	13292539	3280514	2639698
47.9	72.002762	42.053619	29.949142	2576373	13265363	3258019	2620849
48	71.614167	41.901372	29.712795	2566706	13238357	3235832	2602267
48.1	71.228738	41.750166	29.478572	2557131	13211520	3213949	2583951
48.2	70.846476	41.600001	29.246475	2547645	13184854	3192369	2565898
48.3	70.46738	41.450877	29.016502	2538249	13158359	3171089	2548106
48.4	70.09145	41.302795	28.788655	2528943	13132035	3150107	2530573
48.5	69.718687	41.155754	28.562932	2519726	13104605	3129419	2513190
48.6	69.34909	41.009754	28.339335	2510597	13070997	3109025	2495970
48.7	68.982659	40.864796	28.117863	2501557	13037634	3088921	2478976
48.8	68.619395	40.720879	27.898515	2492605	13028057	3069106	2462206
48.9	68.259296	40.578003	27.681293	2483740	13002452	3049576	2445660
49	67.902365	40.436168	27.466196	2474962	12977006	3030330	2429334
49.1	67.546129	40.29479	27.251338	2466221	12951721	3011118	2413228
49.2	67.191581	40.154103	27.037477	2457536	12926595	2992038	2397339
49.3	66.839792	40.014361	26.82543	2448929	12901631	2973198	2381666
49.4	66.490762	39.875564	26.615198	2440400	12876827	2954595	2366207
49.5	66.144491	39.737711	26.40678	2431949	12852184	2936228	2350960
49.6	65.80098	39.600804	26.200176	2423574	12827704	2918095	2335924
49.7	65.460228	39.464841	25.995386	2415276	12803301	2900195	2321039
49.8	65.122234	39.329824	25.79241	2407055	12772313	2882525	2306282
49.9	64.787	39.195751	25.591249	2398910	12741553	2865084	2291712
50	64.454526	39.062623	25.391902	2390840	12725208	2847870	2277328

Appendix C

First, import the generated data from COMSOL Multiphysics into an Excel file. Then, transfer the data from the Excel file to a MATLAB file to create graphs for analysis, which will be discussed later in the discussion section. The following MATLAB code was written for the data mentioned in Appendix B. A Similar approach was implemented for analysis of other data.

```
%exporting excel data (hardening function)
clear all;%close all
write_fig=0;
T=xlsread('hardening function.xlsx','sheet1','A4:E504');
sur_withTR=T(:,2);
sur_withoutTR=T(:,3);
cor_withTR=T(:,4);
cor_withoutTR=T(:,5)
time=T(:,1);
figure(1);
plot(time,sur_withTR,'r');
hold on
plot(time,sur_withoutTR,'m');
hold on
plot(time,cor_withTR,'b');
hold on
plot(time,cor_withoutTR,'k')
xlabel('time (s)');
ylabel('hardening function,(N/m^2)');
title ('surface with TRIP','surface without TRIP','core with TRIP','core withour TRIP')

hold off
```